University of Naples Federico II

Department of Industrial Engineering

Ph.D. Programme in Industrial Engineering

XXXV Cycle

Ph.D. Thesis

Process modelling, monitoring and control for laser welded copper-to-steel battery tab connectors

Supervisors:
Prof. Stanislao Patalano
Prof. Pasquale Franciosa
Prof. Giovanni Pio Pucillo

Ph.D. Candidate:
Ing. Giovanni Chianese

Thesis submitted in 2023

In the middle of difficulty lies opportunity.

- *Albert Einstein*

Abstract

The transition toward electric mobility is influencing the industrial strategies of many productors in the automotive field that are now planning to increase the share of electric vehicles (EVs) in their offer. Production of a finished battery pack can account for the 40% of the added value of a battery EV, therefore, large scale sustainable manufacturing of battery packs is emerging as a topic of strategic importance, and players in the automotive industry are focussing their efforts on research and development of technologies and methods to achieve Near Zero Defects (NZD) production.

Structure of a battery packs for electric vehicles follows a pack-module-cell layout with up to several thousand of joints within a pack. For this reason, manufacturing connections between cells and modules is a task of critical importance in the entire production process, and repeatability is a strong requirement as, joints with different electrical resistance result in inhomogeneous current loads that can lead to detrimental effects on the performances and durability of the entire system.

As it offers relevant technological advantages, such as high production rate, one side accessibility, narrow heat affected zone (HAZ), and possibility to reprocess defective seams, remote laser welding (RLW) enables good flexibility, automatic manufacturing processing and cost-effective mass production. Therefore, it is establishing itself as a key-enabler technology for sustainable manufacturing of connections within battery packs. Furthermore, connections between battery cells consist of joints between dissimilar metallic thin sheets, and RLW is potentially applicable to any cell type configuration and metals combination.

Uncontrollable variations involved in the process pose significant challenge, as they can affect repeatability with detrimental effects on the quality of the weld joint and of the battery system. Variations from the manufacturing and clamping tolerances can cause geometric variations of the parts and, ultimately, result in lack of connection. Incorrect thermal management during welding can lead to damage to battery cells due to overpenetration with the unwanted risks of piercing and leaks. Additionally, welding of dissimilar metals with laser technology involves significant mixing, resulting in additional challenge in terms of control of cracking mechanisms and brittle Inter-Metallic Compounds (IMC). All these challenges urgently call for innovative solutions and models to control RLW of dissimilar metallic battery tab connectors.

Deployment of control systems can have significant impact toward automatization of the process and achievement of NZD production target. However, its development and implementation consist of intermediate objectives. They are: (i) understanding of complex phenomena involved in the process, (ii) in-process monitoring of targeted nuisance factors, (iii) classification of the actual status of the RLW process, and (iv) development of an architecture for autonomous decision of corrective actions.

This dissertation aimed to contribute to achievement of objectives (i), (ii), and (iii) and focused on variations of part-to-part gap and weld penetration depth during RLW of copper-to-steel thin sheets, by addressing the following research topics:

1. Development of a multi-physics CFD model for the simulation of RWL of copper-to-steel thin sheets with variable part-to-part gap and weld penetration depth,
2. Characterization of a photodiode-based sensor to variations of part-to-part gap and weld penetration depth during RLW of dissimilar metallic battery tab connectors,
3. Implementation of photodiodes and supervised Machine Learning algorithms for automatic isolation and diagnosis of weld defects during welding of copper-to-steel thin-sheets.

Table of contents

List of figures

List of Table

Nomenclature

ARM	Adjustable Ring Mode
Ar	Model parameter to be calibrated (Pa)
CFD	Computational Fluid Dynamics
CLIP	Closed-loop in- process
DWT	Discrete Wavelet Transform
c_p c_v	Specific heat at constant volume and pressure (J/kg·K)
D_T	Distance between primary and secondary beam in LBS#4 (µm)
D_{pen}	Weld penetration depth (µm)
EV	Electric Vehicle
f	Fraction of fluid (-)
IMCs	Inter Metallic Compounds
IR	Infrared
$\vec{I}$, $\vec{R}$	Incoming and reflection vector in the ray-tracing model
k	Thermal conductivity (W/m·K)
l_{diff}	Thermal diffusion length (m)
LBW	Laser Beam Welding
$\hat{n}$	Normal to surface in the ray-tracing model
NIR	Near-Infrared radiation
NN	Neural network
OCT	Optical Coherent Tomography
P_L	Laser power (W)
PPs	Process parameters
P_{recoil}	Recoil pressure (Pa)
P_{sat}	Saturation pressure (Pa)
P_{vap}	Partial pressure exerted by vapour (Pa)
Q_{mass}	Evaporation rate (kg/s)
R	Gas constant (J/mol·K)
R_I , R_{II}	Curvature radius at interface (m)
L_P	Laplace pressure (Pa)
S_M	Marangoni forces (Pa)
S_P, S_T, S_R	Photodiode-based signals
T	Temperature (K)
T_L	Lower material thickness (µm)
T_S	Throat thickness (µm)
T_U	Upper material thickness (µm)
T_v, P_v	Coordinates of a point on the saturation curve (K, Pa)
UV	Ultra-violet radiation
VIS	Visible radiation
VOF	Volume of fluid
W_B	Width of the weld seam at the bottom (µm)
W_E	Effective width (µm)
W_{int}	Width of the weld seam at the interface (µm)
W_{top}	Width of the weld seam at the top (µm)
t_{end}	Simulated welding time (s)
α	Accommodation coefficient (-)
γ	Ratio of specific heats of air (-)

ΔHv	Latent heat of vaporization (J/kg)
∇_t	Gradient along the tangent direction
μ_P, μ_T, μ_R	Mean values of signals S_P, S_T, and S_R
ρ	Mass density (kg/m^3)
σ	Surface tension (N/m)
σ_P, σ_T, σ_R	Scatter levels of signals S_P, S_T, and S_R

Chapter 1

1 Thesis overview

1.1 Context

As part of their actions against air pollution and climate change, many countries have set the target to phase out fossil fuel and to shift to electric mobility by enacting laws that progressively ban or restrict the sale of vehicles with internal combustion engine from 2030 [1].

Transition toward electric mobility is resulting in increasing share of electric vehicles sold. Nearly 10% of global car sales were electric in 2021, four times the market share in 2019 [2] -as shown in Figure 1-, and this is influencing the industrial strategies of many productors in the automotive field that are now focussing their efforts to meet the increasing demand of electric vehicles (EVs). Five times more new EV models were available in 2021 than in 2015, increasing the attractiveness for consumers. Estimates report that the annual 2030 global EV sales are projected to be 21-31 million [3]. In this context, large scale sustainable manufacturing of battery packs is emerging as a target of strategic importance that can be achieved with Near Zero Defects (NZD) production. Estimates report that the battery pack alone is worth about the 40% of the added value of a battery EV [4], and, therefore, players in the automotive industry are focussing their efforts in research and development of technologies and methods for sustainable manufacturing of this key component.

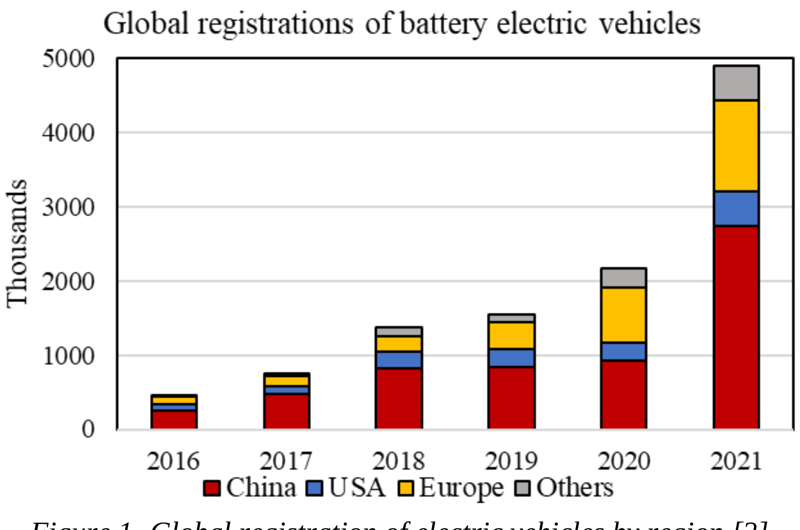

Figure 1- Global registration of electric vehicles by region [2].

Battery packs for electric vehicles have a modular structure [5,6] and lithium-ion is the preferred technology for rechargeable cell units in typical applications for EVs [7]. The structure follows a cell-module-pack layout where the battery pack consists of modules, and cells are connected in series or parallel within a module. The design of the layout depends on the characteristics of the battery cell type that is employed, and on the requirement of the overall battery pack in terms of capacity and power [6]. Up to several thousands of joints are realized within a pack, and defective single connection between cells can influence the functionality and efficiency of the whole battery system. Indeed, joints with different electrical resistance result in inhomogeneous current loads that can lead to detrimental effects on the performances and durability of the entire system [5]. Therefore, manufacturing connections between cells and modules has critical importance in the entire production process and repeatability of the process is a strong requirement.

Connections between battery cells are realised by joining tab connectors which consist of dissimilar metallic thin sheets and repeatability of the process, in terms of electrical resistance and mechanical strength, is a strong requirement.

Remote Laser Welding (RLW) is emerging as a key-enabler technology to manufacture the case of battery pack and connections within it [8,9], as it offers technological advantages, such as high production rate, one side accessibility, narrow heat affected zone (HAZ), and possibility to reprocess defective weld seams. For these reasons, RLW enables highly flexible and efficient production, and shows significant superiority in realizing automatic manufacturing processing [10]. Estimates report that between 60-80% of the overall production cost of a finished battery pack can be addressed by laser material processing [11], and comparative studies showed that the joints realized with RLW have lower electrical contact resistance and higher joint strength than resistance spot welding and ultrasonic welding; additionally, RLW is applicable to any cell type (either cylindrical, prismatic or pouch) with tab connectors consisting of dissimilar metallic thin sheets (i.e., steel, aluminium, copper) [4].

1.2 Challenges

RLW involves several complex physic phenomena, such as laser-metal interaction, phase change with intense evaporation and keyhole formation. Final quality of the weld joint can be affected by several factors, such as thermal conditions during laser–material interaction, variations in material properties due to impurities on the workpiece surface, and changes in the properties of the laser beam, all of which may result in a product that does not meet the requirements [12]. For this reason, stability, repeatability and automatization of the process can be affected by occurrence of disturbance factors that introduce variations [10].

Automatization and repeatability of RLW of dissimilar metallic thin sheets can be affected by several challenges. They include:

(1) Incontrollable variations in the geometry of the thin sheets due to the low bending stiffness, and cumulated manufacturing and clamping tolerances, can result in excessive part-to-part gap which prevents sound welding and affect repeatability of the process.
(2) Temperature management during the joining process to avoid damage to battery cells and to minimize the risk of fire and explosion due to over-heating or over-penetration welds.
(3) Control of cracking mechanisms and brittle Inter-Metallic Compounds (IMC). Welding of dissimilar metals with laser technology involves significant mixing of two materials with different thermal and mechanical properties which can lead to segregation and precipitates, poor compatibility and miscibility, and poor joint strength.

In particular, variations due to Challenge (1) lead to joints with lack of connections that are also indicated as *false friends* in the industrial environment, as they are difficult to detect by visual inspections. Figure 2 shows an example of dissimilar metallic thin sheets with sound weld and lack of connection. Realisation of uneven or defective connections within the battery pack, that lead to anomalous current loads on the battery cells, is not only critical for the performances of the battery system but also affects the environmental impact of the production. Achievement of NZD production would have significant beneficial impact on:

i. scrap rate, as early detection of defects and deviations can shorten processing me and enable online compensation of process deviations for “first time right” [12]. At the present, principal causes that mostly contribute to scrape rate in manufacturing of connections within the battery pack, are lack of connection in the joints (false friends), and cell piercing, due to over-penetrated joints- scrap rate is currently at 15%; and,
ii. likelihood of performance degradation after sale - reports indicate that up to 20% warranty claims in the first 6 months after sale were due to formation of micro-cracks in joints which were not detected until delayed leakages occur.

Implementation of in-process quality control system can significantly contribute toward NZD production by enabling automatization with adaptive adjustment of process parameters, and real-time diagnosis and isolation of defective welds.

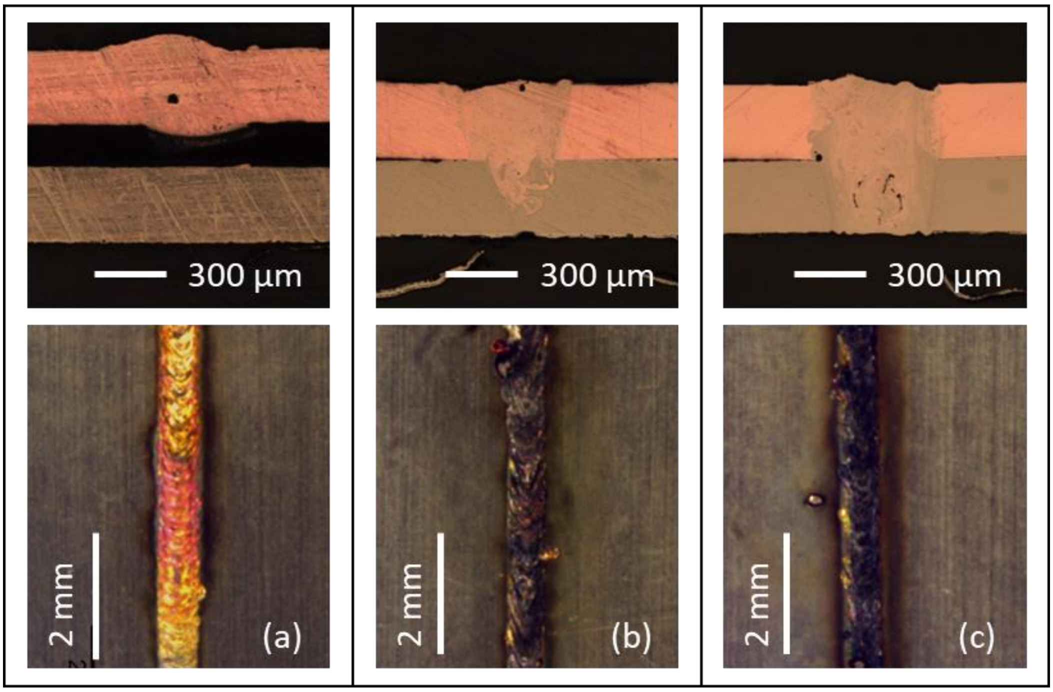

Figure 2 - Top view and cross sections of 300- µm copper-to-steel welds with lack of connection (a), sound weld (b) and over-penetration (c).

1.3 Motivation

Closed loop in-process (CLIP) control systems enable automatization of the process and real-time adaptive adjustment of process parameters. As schematised in Figure 3, generic framework of a CLIP control system hinges two main streams: in-process monitoring of targeted variations with sensors, which is indicated as *feedback process*, and autonomous adjustment of process parameters (PPs - laser power, focal position) to achieve given requirements, which is indicated as *forward process* [13]. Autonomous adjustment of PPs can follow a *data-driven*, a *physics-driven*, or an integrated approach. Data-driven systems adjust PPs purely based on the data used to train the system, whereas physics-driven systems calculate the process status based on directly measured process features that are inputted in physics-based model.

Though necessary for in-process monitoring, performances of data-driven approaches are highly dependent on data used during training and can lack of physical link in defect identification during root causes analysis. Therefore, integration of physics-driven CAE models with data-gathering would enabled physical interpretability of data, whereas in data-driven techniques decision process based on numeric value of model parameters without physical meaning, which are therefore so-called "black-box" [10,14]. Development of a physical model is the first step toward integration of data collected with sensors and reference values that are inferred for simulated scenarios with the digital model. This is a fundamental step toward development of digital twins of the process. Indeed, matching data that are gathered with sensors during the real process with data simulated with digital model, a key-concept of digital twins. For all these reasons, this research topic is becoming the latest trend and focus of intelligent welding field.

The target of integrating physics-driven and data-driven approach for the development of a control system, requires achievement of intermediate objectives, which are:

I. Physics modelling and understanding of complex phenomena involved in the process,
II. Capability to in-process monitor target nuisance variations with sensors,
III. Diagnosis and isolation of weld defects via classification of the actual status of the RLW process with data from sensors,
IV. Development of a model for autonomous adjustment of PPs.

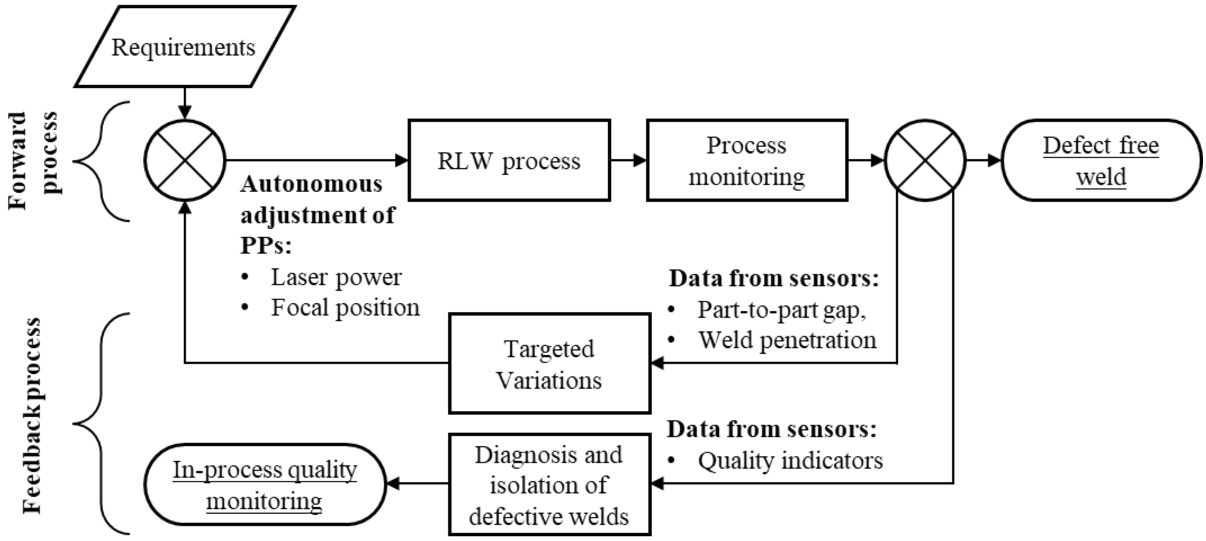

Figure 3- Generic flux-diagram of CLIP quality control system.

1.4 Ph.D. goals, research questions and methodology

This Ph.D. aimed to contribute toward development of a CLIP quality control system and focusses on objectives I, II, and III. Therefore, the following research questions were addressed:

a) How to model RLW of battery tab connectors, so that complex phaenomena involved in the process can be simulated, and then analysed and understood via combined numerical and experimental approach?
b) Is it possible to detect targeted disturbance factors that cannot be controlled by processing data gathered with optical sensors during RLW of battery tab connectors?

c) How to develop a model that leverages optical sensors and ML algorithms for real time diagnosis and isolation of defective welds?

Combination of experimental and numerical approaches was used to address these research questions. The research focussed on variations of the part-to-part gap and weld penetration depth during the welding process, as they are the object of great interest in the industrial environment due to their strategical implications, as explained in the previous section. RLW of battery tab connectors was experimentally studied by welding copper-to-steel thin sheets, with thickness ranging between 200-300 μm.

Objective I was the investigation of the process via physics modelling for the understanding of complex phaenomena involved, and it was achieved by addressing question (a). A multi-physics CFD model of the process was developed to simulate RLW of 300 μm-thick copper-to-steel using a commercial software FLOW-3D and its module FLOW-WELD. Multi-physics CFD analysis enabled access to subsurface features that are difficult to measure with in-situ monitoring. This allowed analysis and understanding of complex phaenomena involved during the process, and ultimately discussion on root actions for weld optimization via laser beam shaping implementation.

Objective II was addressed with characterization of a photodiode-based sensor to variations of weld penetration depth and part-to-part gap. Photodiodes have relatively simple structure and low-cost implementations, and their potential to monitor process variations during laser welding of thick part for structural applications was largely investigated. However, research about applications to monitor part-to-part gap in dissimilar thin sheets welding was scattered. Additionally, as they passively record optical emissions during the process, operativity and effectiveness of photodiodes-sensors do not need them to be recalibrated when operative conditions change, whereas some other sensing techniques do, such as Optical Coherent Tomography OCT [15], that directly observe features of the process. Results of this research activity provide an answer to research question (b).

Once characterisation of photodiodes allowed assessment of their capability to detect variations of weld penetration depth and part-to-part gap, objective III, which consisted of diagnosis and isolation of defective welds, was addressed by using supervised Machine Learning ML for automatic classification of photodiode-signals that were record during the weld. Three classes were introduced to label three welding conditions, *sound weld*, *lack of connection* and *over-penetration*, that are represented in Figure 2. Best in class ML algorithms and a neural network (NN) that was trained with coefficients calculated with discrete wavelet transform (DWT) of the signals were considered. Training of these models and classification of welds provided scientific basis to answer research question (c).

1.5 Contributions of this Ph.D.

Research addressed in this Ph.D. aimed to provide methods and solutions to cope with challenges that welding dissimilar metallic battery tab connectors poses.

Besides being relevant in the implementation of a digital twin of the welding process, the development of a multi-physic model can effectively contribute to right-at-the-first-time implementation of the process in the production environment and its improvement. Indeed, as in-situ in-process observation of subsurface features, such as surface-tension related mechanisms, velocity and temperature fields, still is not viable due to technological challenges, multi-physic modelling enables combined experimental-numerical approaches that can boost fundamental research about complex phaenomena occurring below the surface of the process region. For this reason, modelling enables analysis of root causes and identification of corrective actions for improvement of the process without the need of extensive experimental campaigns that are expensive and time-consuming.

In-process monitoring, diagnosis and isolation of weld defects are relevant for improvement of efficiency and quality of the production. Estimates report that average rate of defective cells and modules produced in Gigafactory is approximately 6% due to faults in the joining processes [16]. One of the challenges is the detection of *false friends* (welds with no connection) by visual inspection of the top view of the seam. Additionally, it has been estimated that up to 20% warranty claims in the first 6 months after sale were undetected defective welds. In this context, in-time diagnosis and isolation of faulty welds has beneficial effects on the efficiency and the quality of the overall production, as it prevents that semifinished workpieces with undetected flaws undergo to further processing with waste of time and resources, or that battery packs with defective connections are placed on the market with performance degradation after sale.

For all these reasons, modelling, monitoring and controlling the process of laser welding battery tab connectors has a strategical impact on industrial applications and represents a hot spot in the process chain and should be considered.

1.6 Thesis structure

This dissertation follows the following structure:

- Chapter 2 provides background, concepts, and common terms involved in manufacturing of battery packs for electric vehicles with RLW, and in in-process monitoring and control.
- Chapter 3 reports development of a multi-physics CFD model with the details of assumptions and modelling approaches, results of simulations with RWL of copper-to-steel thin sheets with variable part-to-part gap and weld penetration depth, and discussion on opportunities for process improvement.
- Chapter 4 addresses characterization of a photodiode-based sensor for the detection of variations in part-to-part gap and weld penetration depth during RLW of dissimilar metallic thin sheets.
- Chapter 5 addresses diagnosis and isolation of defective welds via implementation of photodiodes and supervised ML for automatic isolation and diagnosis of weld defects during welding of copper-to-steel thin sheets.
- Chapter 6 lays down final remarks and discusses next steps for further developments.

Chapters 3 of this dissertation extensively deals with research which is reported in a manuscript that is currently under review process, and in the following conference article:

- Chianese, G, Jabar, S, Franciosa, P, Ceglarek, D, Patalano, S. “A multi-physics CFD study on the part-to-part gap during remote laser welding of copper-to-steel battery tab connectors with beam wobbling.” (DOI: 10.1016/j.procir.2022.08.075).

Chapters 4 and 5 of this dissertation extensively treats contents of the following journal articles:

- Chianese, G., Franciosa, P., Nolte, J., Ceglarek, D., and Patalano, S.. "Characterization of Photodiodes for Detection of Variations in Part-to-Part Gap and Weld Penetration Depth During Remote Laser Welding of Copper-to-Steel Battery Tab Connectors." ASME. *J. Manuf. Sci. Eng.* July 2022; 144(7): 071004. (DOI: 10.1115/1.4052725), and
- Giovanni Chianese, Pasquale Franciosa, Tianzhu Sun, Dariusz Ceglarek, and Stanislao Patalano, "Using photodiodes and supervised machine learning for automatic classification of weld defects in laser welding of thin foils copper-to-steel battery tabs", *Journal of Laser Applications* 34, 042040 (2022) (DOI: 10.2351/7.0000800).

Chapter 2

2 Background

2.1 Structure of a battery pack for EVs and requirements of the connections

Battery packs for EVs consists of up to thousands of individual rechargeable battery cells that are structurally held and electrically connected [17]. Lithium-ions is the preferred technology in electromobility as it allows high energy-to-weight ratios, high open-circuit voltage, low self-discharge rate, low memory effect, and a slow loss of charge when not in use [7]. Battery cells are made up of a cathode, an anode, a separator that is soaked in an electrolyte, and a robust housing [7]. They are manufactured in different types and are classified based on their geometry in three different categories: small solid cylindrical cells, larger solid prismatic cells and larger soft pouch cells, which are represented in Figure 4 [17]. Although the dimensions of the three cell types can vary between different manufacturers, standards ISO/PAS 16,898:2012 and DIN 91,252:2016–11 define the dimensions [6]. Typically, size of battery cells is smaller for the cylindrical than for prismatic and pouch types. This results in lower individual capacity of the cylindrical battery cells compared to the prismatic and the pouch ones.

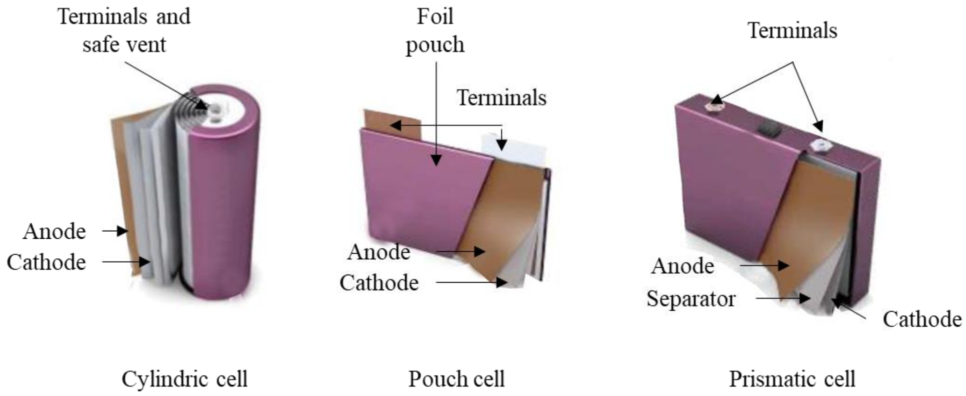

Figure 4- Cylindric, pouch and prismatic battery cells [17].

Structure of a battery pack follows cells-module-pack layout. Cells are clustered within a module with series or parallel connections, and modules are connected in series, as shown in

Figure 5. The design of the layout depends on the characteristics of the battery cell type that is employed, and on the requirement of the overall battery pack in terms of capacity and power. Indeed, two approaches can be followed: (i) connection in series of a lower number of large battery cells with a high individual cell capacity, or alternatively (ii), larger number of small battery cells with low individual cell capacity can be connected in parallel and subsequently connected to modules with high capacity [6].

Requirements of battery pack manufacturing are highly interdisciplinary [5,6,17], and can be summarized as follow:

- Electro-thermal requirements – Low electrical resistance is required, as joints between cells high resistance results in lower efficiency of the entire system; additionally, higher electrical resistance result in higher heat generated that contribute to thermos-mechanical stresses of the joint.
- Thermo-mechanical requirements – To manufacture the joints with low thermal input because high temperatures and heat transmission can have detrimental effect on adjacent components, and result in residual stresses mechanical stresses in the joint.
- Mechanical requirements – As battery pack and modules are subjected to cyclic loads and random vibrations, adequate fatigue resistance is required to stand operational loads.

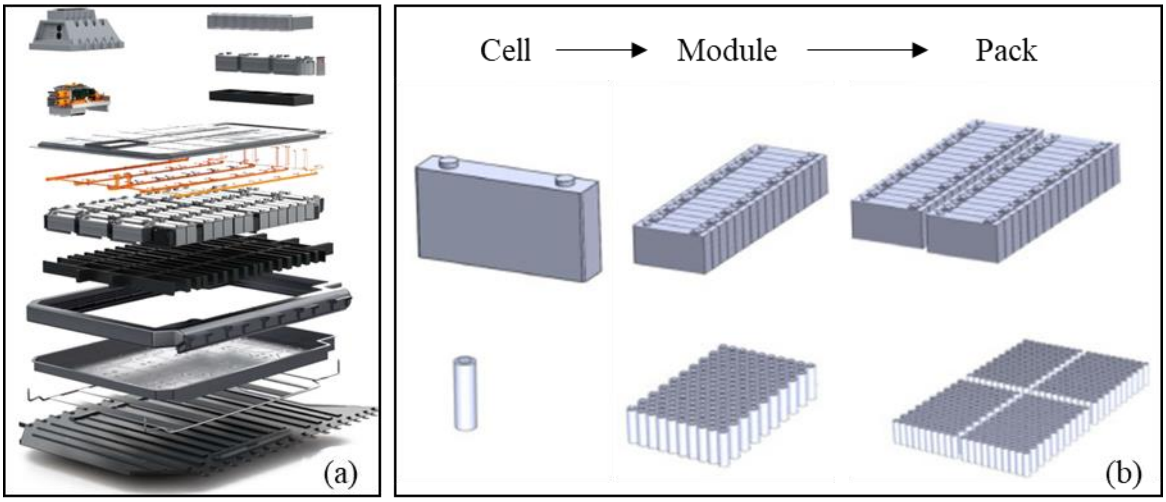

Figure 5 – Structure (a) and modular layout of a battery pack with individual cells, modules and pack level (b) [6].

2.2 Remote Laser Welding for automotive applications

Laser beam welding is a joining technology widely employed in several industrial fields, such as automotive, aerospace, ship-buildings, and electronics, due to its technological advantages and good flexibility [10,18]. Indeed, reduced, controlled, and very localised heat input leads to narrow heat affected zone (HAZ), high precision and low distortion of parts. Contactless nature of laser light and one-side accessibility ensure good flexibility of the weld process. Reduced processing time, with the possibility of making a single weld in fractions of a second, and significant superiority in realizing automatic manufacturing processing enable high throughput necessary for high production volume.

Connection between workpieces can be established during laser welding in two different operational modes: (i) conduction mode, and (ii) keyhole mode. During laser welding in conduction mode, the melt pool is created as the laser heats the metal up to its fusion temperature with no significant evaporation, during keyhole welding, higher power density determines intense and localised evaporation that results in the formation of a deep and narrow capillary in the melt pool, which is called keyhole. Multiple reflections of the laser in the keyhole increase efficiency of the process as almost all the laser power is absorbed.

Another classification of laser welding is based on the distance between the optics and the workpiece. Laser welding with conventional fixed optics involves distances between optics and workpiece to about 250 mm [19], as they enable short focal length, and, therefore, it is known as tactile laser welding. RLW involves medium to long focal length instead, which are enabled by the use of optic fibre, and allow longer distances between the optics and the workpiece (0.8 – 1.1 m), and the use of 6 axis robot for delivering the lases power [20]. These features of RLW enable minimization of the repositioning time between different welds, with beneficial effects on the efficiency due to significantly shorter overall cycle time and increase of the throughput [13].

2.2.1 Applications in the automotive field

First implementation of laser welding in the automotive field was carried-out by *Optical Engineering* in 1997 in California [20].

Nowadays, RLW is emerging as a key-enabler technology to enable Industry 4.0, due to its technological advantages and opportunity for process automation. Indeed, use of medium to long focal length enables customized weld patterns with different shapes, orientation, and distribution, and this results in furtherly improved flexibility of the process [4].

In the context of automotive applications, and in particular of manufacturing of EVs, the need for innovative cost efficient solutions that can enable smart manufacturing and mass production are driving technological advances achieved by laser manufacturers and system integrating companies [4,9,21]. RLW, with its technological advantages, meets this need for cost efficient mass production of electric vehicles and enables manufacturing of battery packs enclosure [8], of connections within battery pack [22,23], welding of hairpins in electric power train [24] and contacting in power control unit assemblies, beside manufacturing of connections between structural part of the body in white [4,25,26]. Figure 6 provide a graphical overview of production processes that can be addressed by RLW.

Figure 6- Tasks that can be addressed by RLW in electric vehicles manufacturing [21].

2.3 Sensing techniques and real-time monitoring of the RLW process

As the weld quality can be affected by factors coming from the manufacturing environment or from variations in the workpiece (in the geometry or in the local material properties), real-time solutions for quality monitoring can provide information to detect faults and to control the process [27]. During monitoring of RLW, information can be collected from observation of the keyhole, molten pool, plasma and spatter, by gathering acoustic, optical and thermal signals with different sensing technologies. Charged-coupled devices (CCD), complementary metal oxide semiconductors (CMOS), and high-speed cameras enable vision of the monitored region by gathering frames and images, which provide spatially resolved information.

Three different types of approaches for real-time monitoring can be distinguished based on the position of the region of interest with respect to process zone, as shown in Figure 7 [27].

Pre-process scanning involves seam tracking and valuation of the part-to-part gap mainly; in-process monitoring consists of direct or indirect measurement of features in the process zone, such as optical and acoustic emissions, surface temperature fields, geometry of the molten pool at the surface, spatter and plasma plume; post-process diagnosis concerns direct detection of weld defects such as pores, cracks, humping and underfill, which are indicators of poor weld quality [10,27,28].

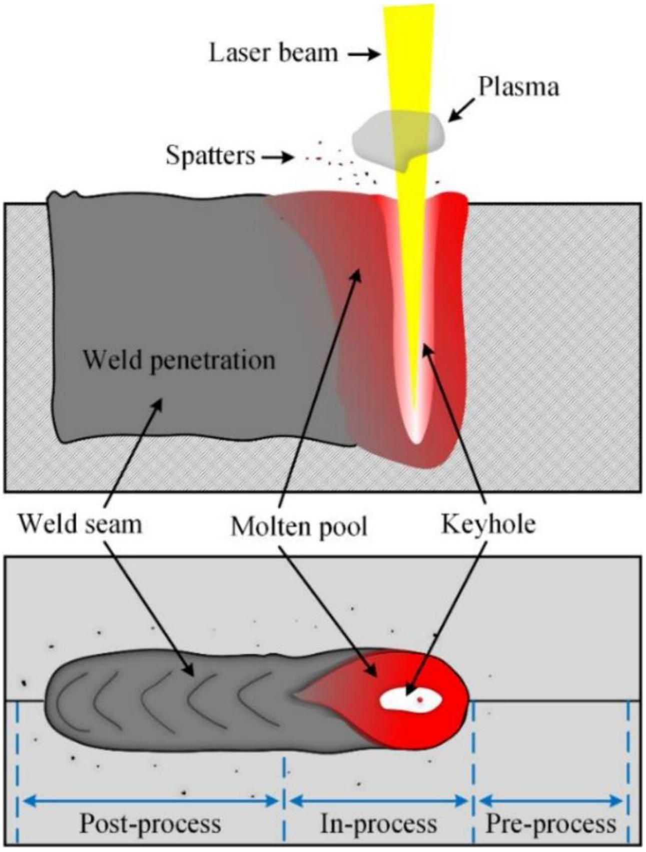

Figure 7 - Schematic representation of pre-process, in-process and post-process monitoring [27].

Traditional monitoring can be classified with respect to the sensing techniques in acoustic, optical and thermal sensors. Acoustical sensors can record pressure fluctuations that are caused by ejection events in the keyhole or phase changes in the material [27,28]. Optical sensors can be classified in spatially resolved (vision system [24], e.g., CCD [29] and CMOS cameras), and spatially integrated (photodiodes [30]), or spectrally resolved (spectrometers [31]) techniques [28]. Pyrometers and IR cameras respectively provide spatially integrated and resolved measurements of temperature in transient and steady state [32].

Novel monitoring methods proved to directly measure features of great interest which are strong indicators of the weld quality. They include, X-ray videography which can provide spatially and time resolved observation of subsurface features such as the keyhole geometry or pore formation [33], OCT that directly measures the keyhole depth in real-time [15] and, therefore, can enable closed loop control of the process.

As single sensors are not able to completely describe the complexity of phaenomena involved in laser welding, sensor fusion has been investigated for more comprehensive understanding and more detailed monitoring of the process. Indeed, fusion of different sensing techniques enables gathering of signals that carry different and non-correlated information [34].

As data are gathered, real-time monitoring involves features extraction from data, which consists of signal processing and imaging processing of spatially integrated and spatially resolved data, respectively. Traditional optical imaging processing consists of geometrical features extraction via image filtering, thresholding and edge detection [35]. Signal processing can involve analysis in the time domain with calculation of statistical descriptors [36], analysis of the signal in the frequency domain with Fast Fourier Transform, or analysis in the time-frequency domain with Discrete Wavelet Transform [37] and Short-Time Fourier Transform [10].

Once features are extracted, they can be used to establish a relation between the gathered data and quality of the weld seam. Artificial Intelligence (AI) and supervised ML algorithms can be trained with signal features for the detection and classification of weld defects, process parameters optimization and welding process control [38]. Traditional ML algorithms include support sector machine (SVM), Naïve-Bayes, k-nearest neighbour, decision tree, discriminant analysis, and Artificial Neural Networks (ANN). ANN is the basis for more sophisticated algorithms, such as Convolutional Neural Networks (CNN) that are classified as Deep Learning algorithms and enable direct processing of signals and data, without the need to extract the features [10]. These algorithms automatically learn relevant features during training and, therefore, they are particularly suitable in image processing and features recognition [39].

Chapter 3

3 Multi-physics CFD modelling of RLW of dissimilar metallic sheets

3.1 Introduction

This chapter addressed Objective I, which is the development of a multi-physics CFD model of the process as described in §1.4.

RLW of battery tab connectors is a critical task in the production of battery pack, and repeatability of the process is a strong requirement in manufacturing of connections between cells and modules. As the occurrence of variations in part-to-part gap and weld penetration depth has a great impact on electric and mechanical properties of the joint and on metal mixing, it is critical to understand and model physical phenomena during melting, formation of the keyhole and solidification, that are involved in RLW of dissimilar metallic thin sheets (thickness below 500 μm). Indeed, ex-situ analyses and tests cannot provide comprehensive understanding of the governing phaenomena involved in the process and underlying features, such as subsurface velocity, temperature and mixing fields [40]. Multi-physics CFD models enable simulations of the process that mimic mechanisms which are difficult to observe with in-situ investigations due to technical challenges that still exist, instead. Therefore, simulations, that are now enabled by high computational capability of workstations, are a useful tool that support critical comprehension of phenomena involved, and many researchers are contributing to this field.

This chapter investigated the underlying physics of the welding process to understand the influence of the laser beam wobbling, part-to-part gap and weld penetration depth on temperature fields and metal mixing. A CFD multi-physics model was implemented and then calibrated with experimental data. Scenarios with variable weld penetration depth and part-to-part gap were considered during lap welding of 300 μm copper to 300 μm nickel-plated steel, with circular beam wobbling. After the validation, the model was employed for numerical investigation of corrective actions that improve the process via laser beam shaping.

3.2 State of the art

Due to continuous improvement of computational capability, multi-physics numerical simulations emerged as viable approach to investigate complex phaenomena, and they have gained particular interest in applications where in-situ observation are still technically challenging to perform. In the context of laser welding, extensive efforts have been made to develop multi-physics models for combined experimental-numeric approach to access subsurface features of the process, such as temperature and velocity fields, and to understand complex phaenomena, such as mixing mechanisms and keyhole dynamics.

Artinov et al. developed a 3D transient multi-physics model to study the formation and evolution of the bulging effect during laser welding of two unalloyed steels with thickness of 8 mm and 12 mm [41]. *Meng et al.* implemented three different ray-tracing algorithms based on different free surface reconstruction strategies in a 3D CFD model to evaluate their impact on spatial laser energy distribution and the corresponding molten pool dynamics during laser welding of 10 mm-thick austenitic steels [42]. *Daligault et al.* developed combined ray-tracing algorithm, VOF method and an Eulerian interface tracking method for the liquid-gas interface in an in an axisymmetric FEM model in COMSOL MULTIPHYSICS ® to reproduce the well-known beam trapping in keyhole laser welding of 1 mm – thick copper [43]. *Deng et al.* employed commercial software FLOW-3D ® and FLOW-WELD to simulate RLW of zinc-coated steels with thickness of 0.65 mm and 1.2 mm, respectively on top and at the bottom. They analysed the dynamic behaviour of the keyhole and instantaneous zinc vapour pressure to study the spatter occurrence, and compared the results with high speed filming [44]. Also *Lin et al.* implemented a model in the FLOW-3D suite to simulate RLW of AA 5182 aluminium sheets to study the keyhole dynamics and formation of porosity with variable inclination of the laser beam, laser power and weld speed [45].

Ozkat et al. developed a decoupled multi-physics model for prediction of the weld penetration and interface width during laser lap welding of zinc coated steel sheets considering part-to-part gap [46].*Drobniak et al.* [47] and *Buttazzoni et al.* [48], implemented Computational Fluid Dynamics (CFD) multi-physics simulations of 1 mm-thick stainless-steel plates with adaptive mesh refinement to predict the shape of the weld seam in presence of part-to-part gap. They validated the model and employed it to optimize the weld quality via iterative set of simulations by predicting the effect of secondary laser beams with different shapes to optimize the weld quality.

With respect to dissimilar thin-sheets welding, *Huang et al.* that developed a CFD model in FLOW WELD® to study the metal mixing rate during RLW of 200 μm aluminium to 500 μm copper sheets and all the phaenomena involved [40]; only welding in ideal condition was considered without accounting any disturbance factor. *Chianese et al.* [49] used the same software to investigate the effect of part-to-part gap in RLW of copper-to-steel thin sheets with beam wobbling implemented. They showed that the presence of part-to-part gap and mixing mechanism between parent metals are linked in part because, beside limiting weld penetration, occurrence of part to part-to-gap influences the temperature and velocity fields in the molten pool resulting in different mixing of metals. Then, they outlined opportunities for improvement of the process by implementation of different welding strategies to be investigated in the future with multi-physics modelling.

3.3 Materials and methods

3.3.1 Materials and experimental procedure

3.3.1.1 Materials and equipment

Materials that were employed in the experimental part of this work are Copper SE-Cu58 2.0070 and Nickel-plated Steel (commercial name: Hilumin). Weld trials consisted of 30 mm long welds in lap joints configuration with 300 μm-thick copper on top and 300 μm-thick nickel-plated steel at the bottom. Dimensions of the specimens were: 65mm x 30mm.

The equipment consisted of nLight Compact Fiber Laser 3 kW (n-Light Inc., USA), and the Scout-200 system (Laser and Control K-lab, South Korea) that was used to deliver the laser power to the specimens via 2D F-theta scanner with telecentric lenses. Specifications of the equipments are reported in Table 1 and Table 2. Welding experiments were in continuous mode with no power modulation.

Table 1 - Compact Fiber Laser 3kW, nLight.

Max. output power	3 kW
Wavelength range	1070 ± 10 nm
Beam quality	4 mm·rad
Fibre diameter	50 μm

Table 2 - Scout-200, Laser & Control K-lab.

Working field	70 x 70 mm^2
Collimating length	160 mm
Focal length	254 mm
Max. allowed laser power	2 kW
Spot diameter on focus	80 µm
Rayleigh length	0.8 mm

3.3.1.2 Experimental procedure

Laser beam wobbling was implemented to obtain a wider interface between parent materials and to cope with high reflectivity of copper. The laser trajectory was the result of a linear motion with speed of 120 mm/s and circular oscillations (wobbling frequency of 500 Hz and 0.2 mm radius).

Welding experiments were performed using three different power levels, i.e. 615, 690 and 765 W. All the experiments were performed without shielding gas nor filler wire. Each weld seam was cut and prepared to obtain three cross sections for each experiment. They were mounted in resins disks and prepared by grinding and polishing for the analysis at the optical microscope Nikon Eclipse LV150N. In each cross section, width of the weld seam at the top W_{top}, the width at the interface between parent metals W_{int}, and the weld penetration depth in the thin sheet D_{pen}, were measured to calibrate and validate the numerical model with experimental results. These geometrical features are schematically represented in Figure 8. To evaluate and characterise metal mixing with parent metals, elemental mappings of cross-sections were carried out with an FEI Versa 3D dual beam scanning electron microscope using Energy Dispersive X-ray Spectroscopy (EDS mapping).

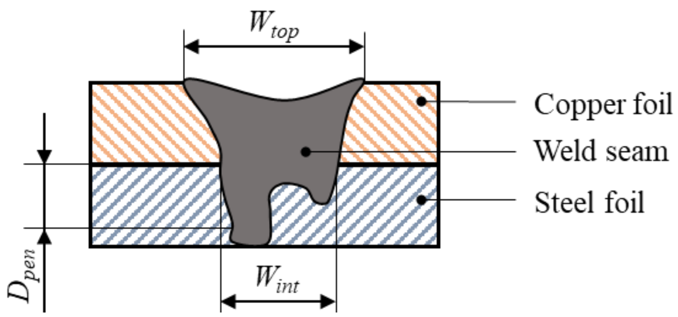

Figure 8-Schematical representation of top width of the weld seam W_{top}, the width at the interface between parent metals W_{int}, and weld penetration depth D_{pen} in the lower thin-sheet.

3.3.2 Model development

A multi-physics model was developed using the commercial CFD code FLOW-3D ® and its module FLOW-WELD. To reduce the computational cost of the simulations, the computational domain was divided in two zones, a process zone which was interested by phase change, and a thermal diffusion zone that models heat transmission in the thin sheets. A finer mesh size was used for cells in the process zone, and a mesh size 5 times greater than in the process zone was used for cells in the thermal diffusion zone.

Dimensions of the process zone were 2 mm x 0.8 mm x 0.725 mm. Length of the process zone was chosen to enable simulation of 1.9 mm weld length; the width value was selected to ensure that the full wobbling pattern and phase change events were restricted in it. Extension of the thermal diffusion zone was calculated according to the following formula:

$$l_{diff} = 2\sqrt{2\frac{k(T=T_{amb})}{c_P(T=T_{amb})\cdot\rho(T=T_{amb})}\cdot t_{end}} \tag{1}$$

Four different values of the mesh size in the process zone were considered during sensitivity analysis, namely 40 μm, 20 μm, 15 μm, and 10 μm, that resulted in mesh independent solution for mesh size equal to or below 15 μm, which therefore is the selected size. This led to total number of cells approximatively equal to 479 thousand. Thin sheets were oriented in the computational domain so that in-plane dimensions were parallel to X and Y axis, as shown in Figure 9; welding direction was parallel to X axis.

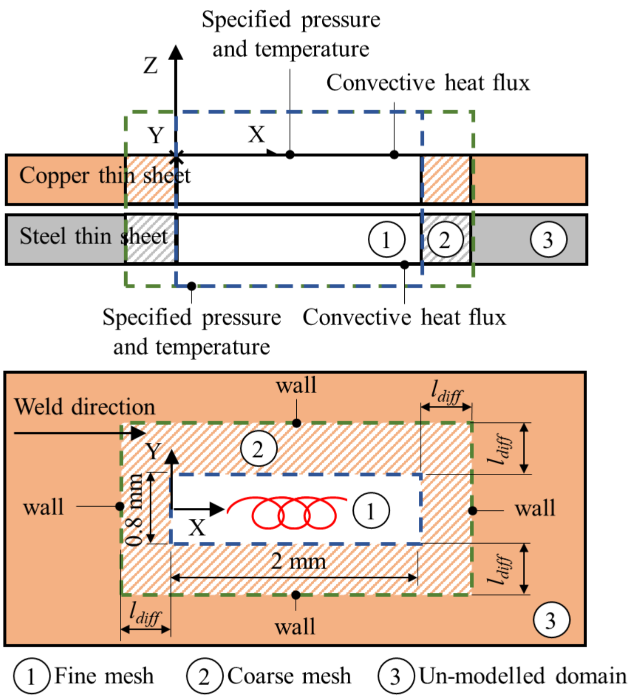

Figure 9 - Schematic representation of the computational domain and modelling approach with nested meshes.

3.3.2.1 Assumptions and boundary conditions

The following model assumptions were made: (i) the liquid flow was considered Newtonian and incompressible; (ii) volumetric thermal expansion of the liquid metal due to temperature dependent mass density was accounted; (iii) the air and vaporized metal were modelled as “void” type, with room temperature and pressure assigned to model the heat exchange with the metal as a natural convective flux (irradiance is neglected); (iv) the laser beam waste was assumed cylindrical as the stacked thickness of the processed foils including eventual gap between the parts, was within one Rayleigh length.

The following boundary condition were assigned: wall in the X and Y direction (with constant ambient temperature); assigned pressure and temperature at the boundaries of the computational domain in the Z directions, with natural convective heat flux between the metallic sheets and the air.

3.3.2.2 Governing equations

The following physics were accounted to model the welding process: continuity, fluid flow via Navier-Stokes equations, energy conservation, metal melting and evaporation, keyhole formation and evolution, solidification, species conservation and tracking, surface tension with Marangoni and Laplace forces, and multiple reflections.

Incremental fusion in the cells occurred as latent heat was absorbed by the metal once the fusion temperature was reached. Information about whether fusion occurred or not in a cell was provided by the output variable *melt region*, whose value ranges between 0 and 1 to indicate the cases in which melting did not involve or involved all the metal of the cell, respectively.

Equation 2 governs evaporation phenomena which were modelled as mass transfer between the liquid phase and the void type and as proportional to the difference between the saturation pressure P_{sat} and the partial pressure P_{vap}. In this equation, α is the accommodation coefficient, R is the gas constant, and T is the temperature. The saturation pressure was calculated as a function of the temperature according to the Clapeyron equation (equation 3), in which the couple of values (P_v , T_v) represents a point on the saturation curve; γ, c_v, and ΔH_v, are the specific heats ratio, the specific heat at constant volume, the latent heat of vaporization.

During remote laser welding, intense vaporization results in the recoil pressure that drives the formation of a capillary, the keyhole, and keeps it open by acting on its surface. The recoil pressure was modelled as proportional to the saturation pressure according to equation 4, where a (and therefore Ar) is a constant to be calibrated.

$$Q_{mass} = \frac{\alpha}{\sqrt{2\pi RT}} \cdot \left(P_{sat} - P_{vap}\right) \tag{2}$$

$$P_{sat} = P_v \cdot \exp\left(\frac{\Delta H_v}{(\gamma-1)\cdot c_v T_v} \cdot \left(1 - \frac{T_v}{T}\right)\right) \tag{3}$$

$$P_{recoil} = a \cdot P_{sat} = a \cdot P_v \cdot \exp\left(\frac{\Delta H_v}{(\gamma-1)\cdot c_v T_v} \cdot \left(1 - \frac{T_v}{T}\right)\right) = Ar \cdot \exp\left(B \cdot \left(1 - \frac{T_v}{T}\right)\right) \tag{4}$$

The surface of the keyhole was tracked by the VOF method, which enabled calculation of the interface between the liquid metal and the void type, according to equation 5. The interface between of the cell was tracked using a scalar value f that indicates the fraction of fluid. A value of $f = 1$ indicates that the cell has only void, conversely, $f = 0$ corresponds to the case of a cell full of liquid, whereas the case of $0 < f < 1$ indicates that the cell has both the liquid and the void type, and therefore the interface between the two is falls in it.

Similarly, metals involved in the welding process with fluid flow and mixing were tracked in each cell by means of a scalar value f_2, which indicates the fraction of second material within the cells. Values of the generic material property $\overline{\varphi}$ in each cell was evaluated as weighted sum of the properties φ_1 and φ_2 of parent metals based on their mixing, according to the equation 6.

$$\frac{\partial f}{\partial t} + \nabla\left(\vec{V} f\right) = 0 \tag{5}$$

$$\overline{\varphi} = (1 - f_2) \cdot \varphi_1 + f_2 \cdot \varphi_2 \tag{6}$$

Tracking of multiple reflections was implemented using a discrete grid cell system ray tracing technique. The laser beam was divided into a finite number of rays, which moved in the laser beam irradiation direction. When the ray encountered the surface of the material, it was reflected according to vector equation 7, in which $\vec{R}$ is the direction of the reflected vector, $\vec{I}$ the direction of the incoming ray, and $\hat{n}$ the normal direction of the material surface.

$$\vec{R} = \vec{I} - 2\left(\vec{I} \cdot \hat{n}\right)\hat{n} \tag{7}$$

Due to its high reflectivity especially at room temperature, the laser absorption of copper was evaluated as temperature dependent.

Beside recoil pressure, that drives the formation of the capillary and contributes to the velocity field in the fluid, surface tension related phenomena, such as the Laplace pressure L_P and the Marangoni force S_M, also have great influence on the process. They were modelled according to equations 8 and 9, in which, σ is the surface tension, R_I and R_{II} are the principal curvature radii, and operator ∇_t indicates the gradient along the tangent direction at the interface. Equation 9 explicitly indicates the dependence of the Marangoni effect on the gradient of the surface tension, which in this work is entirely associated to temperature dependence of the surface tension.

$$L_P = \sigma \cdot \left(\frac{1}{R_I} + \frac{1}{R_{II}}\right) \tag{8}$$

$$S_M = \nabla_t \sigma \tag{9}$$

3.3.2.3 Material properties

Material properties were assumed temperature-dependent and were in part imported from the JMATPRO® material database, in part integrated with research in literature. They were then calibrated to fit the experimental cross sections of all simulated scenarios (part-to-part gap equal to 0 and 100 µm, P_L= (615W, 690 W, 765 W). Although copper and steel are different metals, they were treated with the same evaporation model in the CFD code, therefore, calibrated value of A in equation (4) was unique.

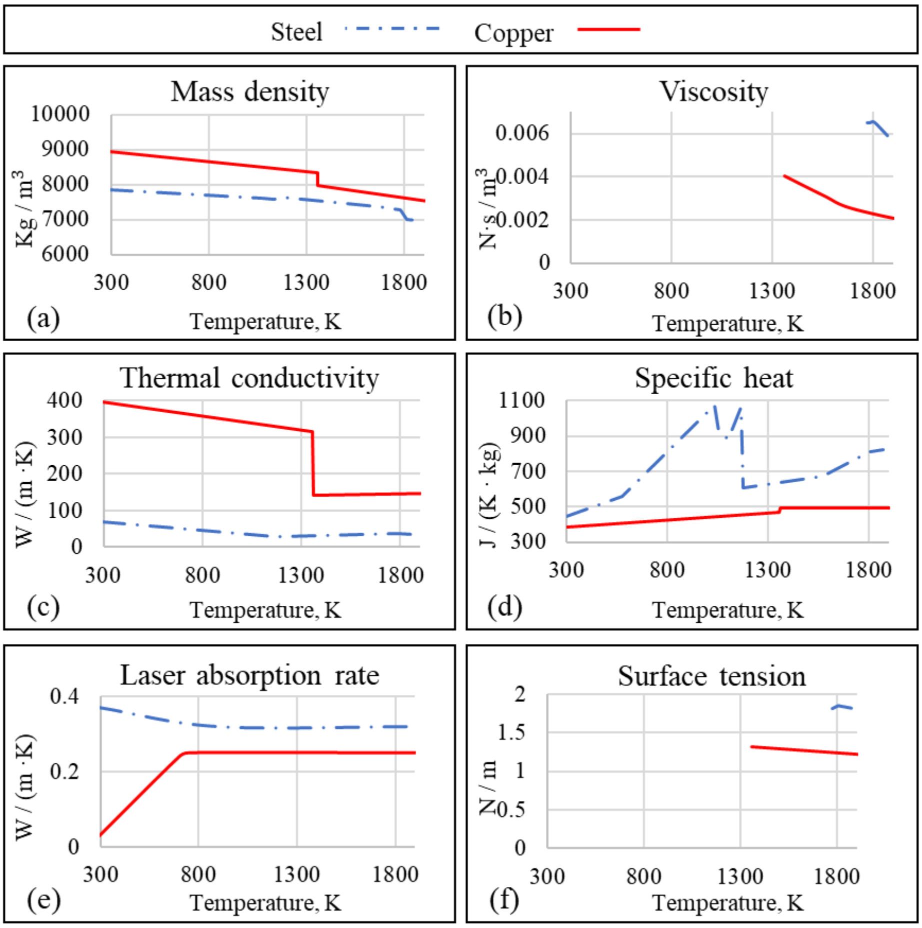

Figure 10 - Temperature-dependent material properties of copper (red solid line) and steel (blue dashed line).

Table 3 - Material properties of copper and steel.

Property	Copper	Steel
Solidus temperature (K)	1357	1770
Liquidus temperature (K)	1358	1813
Latent heat of fusion (kJ/kg)	206.3	290
Vaporization temperature (K)	2835	3134
Latent heat of vaporization (MJ/kg)	4.727	6.080
Vapor specific heat (J/kg·K)	384.6	449

3.3.3 Plan of the simulations

Two sets of simulations were performed: Set #1, to simulate weld experiments to perform combined experimental-numerical analysis of the process, and Set #2, to investigate corrective actions for improvement of the process.

Set #1 consisted of four simulations. Three of them simulated welding with different weld penetration depth and one to investigate the effect of part-to-part gap on the welding process. They were indicated as S1, S2, S3 and S4 and reproduced welding experiments with values of laser power P_L and part-to-part gap that are specified in Table 4, with welding speed of 120 mm/s and circular beam wobbling implemented (wobbling frequency f= 500 Hz, and radius r= 0.2 mm). To validate the model, their results were matched with values of W_{top}, W_{int} and D_{pen} that were measured in the cross sections prepared after experiments. Thermal field, velocity field and mixing mechanisms predicted with simulations were then correlated with experimental observations and analysed for more comprehensive understanding of the process.

Set #2 consisted of simulations that investigate opportunities of process improvement via laser beam shaping. Two welding strategies were investigated by employing secondary laser beam. First, the effects of ring-shaped secondary laser beam were investigated considering three configurations: (i) with only primary laser beam (circular spot), (ii) with combined ring-shaped secondary beam and inner primary beam, and (iii) with combined wider ring-shaped secondary beam and inner primary beam; simulations of welding with these configurations were indicated as LBS#1, LBS#2, and LBS#3, respectively. The reason of this choice is that LBS#1 is the baseline with single beam; LBS#2 and LBS#3 enabled evaluation of the effects of a secondary ring-shaped beam and of its size via comparison with other simulations. Second, the effects of pre-heating laser beam by means of a wider circular spot were investigated with simulations indicated as LBS#4. The reason why this welding strategy was investigated stems in challenges that are posed by high reflectivity at room temperature of metals that are widely employed in these applications, such as copper and aluminium. Indeed, laser power absorption of these metals significantly increases when the temperature reaches the fusion point. Schematic representation of the considered welding configurations and corresponding power density distribution are reported in Figure 11.

Simulations LBS1, LBS2, LBS3, and LBS4, dealed with welding without laser beam wobbling implemented, and the velocity was set equal to 350 mm/s, which is a value in line with experimental works available in literature [50]. Details of process parameters and beam arrangement in these simulations is reported in Table 5. For each weld configurations, values of the laser power P_L for the primary and secondary laser beams were optimised via iterative process to ensure weld penetration depth equal or greater than 90 µm, which corresponds to 30% of the thickness of the lower thin sheet. As selection of optimal values of P_L was carried out with iterative process, a number of simulations was performed, whose details are reported in Table 5.

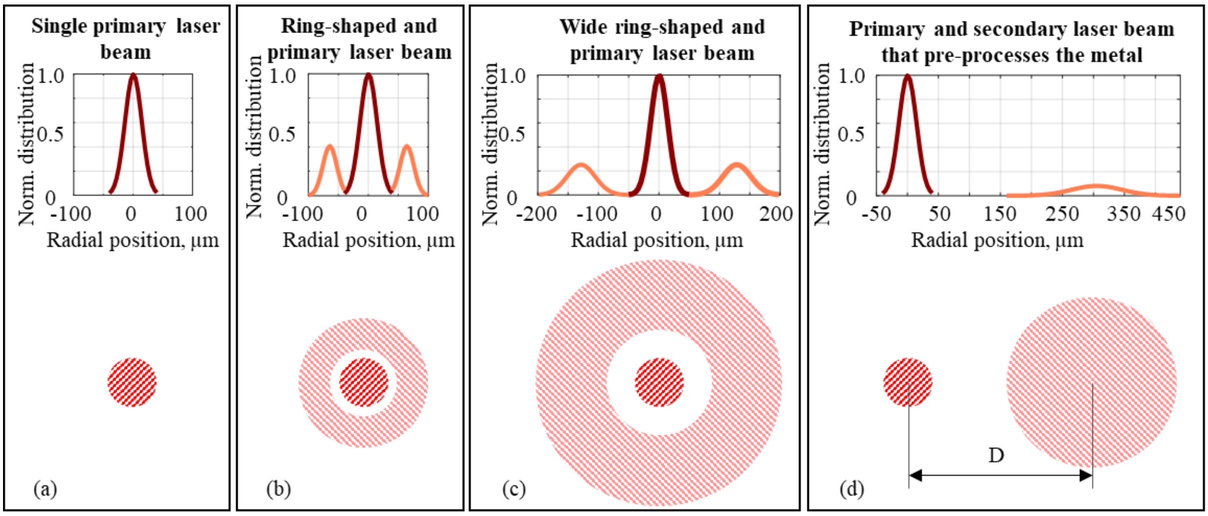

Figure 11- Schematic representation of welding configurations and power density distributions in: LBS1 (a), LBS2 (b), LBS3 (c), and LBS4 (d).

Table 4 - Values of laser power P_L and part-to-part gap for Set #1.

Simulation	Part-to-part gap , µm	Laser power, W
S1	0	615
S2	0	690
S3	0	765
S4	100	690
Constant for all 3 cases		
Speed, mm/s		120
Focal offset		Laser on focus on the upper surface of Cu
Wobbling radius, mm / frequency, Hz		0.2 / 500
Laser beam shape		Circular spot , 40 µm radius

Table 5 - Process parameters set in simulations of Set #2.

Simulation	Laser beam shape: Primary beam Radius	Primary beam Shape	Secondary beam Radius	Secondary beam Shape	Process parameters: Iteration ID	Laser power, W: Primary	Laser power, W: Secondary
LBS1	40 µm	Circular	-	-	1	350	-
					2	700	
					3	500	
					4	600	
					5	650	
LBS2	40 µm	Circular	Inner: 40 µm Outer: 100 µm	Ring	1	300	350
					2	450	450
					3	375	375
					4	300	600
					5	300	450
					6	250	500
					7	350	900
					8	350	700
LBS3	40 µm	Circular	Inner: 100 µm Outer: 200 µm	Ring	1	400	1200
					2	500	1500
					3	400	1500
					4	350	1700
					5	400	1350
					6	350	1500
					Iteration ID	**Tandem distance, mm**	
LBS4	40 µm	Circular	140 µm	Circular	1	0.3	
					2	0.45	
					3	0.6	

Constant for all 4 cases	
Speed, mm/s	120
Focal offset	Laser focus on the upper surface of Cu
Wobbling radius, mm / frequency, Hz	0.2 / 500
Laser beam shape	Circular spot , 40 µm radius

3.4 Results

In this paragraph, experiments and numerical results of Set #1 and Set #2, were analysed and discussed. Profile of welds in the cross sections and geometry of simulated weld of Set #1 were matched after calibration of the model, and quantitative metrics were used to support validation of the model in section 3.4.1.1. Then, in section 3.4.1.2, temperature fields, velocity fields and metal mixing were analysed to understand complex mechanisms involved in the process and their contribution on the metal mixing and quality of the weld seam. The effects of part-to-part gap on the temperature and velocity field were analysed and discussed in section 3.4.1.3 to understand their contribution on phaenomena involved. Once the model was calibrated, in section 3.4.2, prediction of simulations of Set #2 were analysed to discuss opportunities for process improvement via beam shaping.

3.4.1 Simulations of weld experiments

3.4.1.1 Model calibration and validation

Calibration of the model was performed via optimization of the coefficient Ar in equation 4, to simulate the welding process so that cross sections reproduce those observed at the optical microscope. In the evaporation model, the recoil pressure was assumed proportional to the saturation pressure by the constant Ar. The evaporation model is unique with just one entry for Ar, whereas welding involves two metals with different material properties. The value resulting from the optimisation process is Ar = 60780 Pa.

Analysis at the optical microscope revealed that profiles of the cross sections can be distinguished in two types, which are indicated as V-shaped and M-shaped profiles in this work and are shown in Figure 12. This variability seemed to reflect the wobbling pattern of the laser spot (which is schematised in Figure 13). It was explained considering the position of the cross-sections along the weld seam with respect to the path of the laser spot. As the laser moved forward, due to the circular oscillations, the laser spot first processed new material (from position A to position C in Figure 14) and then came back to it (from position C to position A’). Periodic succession of V and M-shaped profiles of the weld seam, that explained variability in the profiles observed with the optical microscope, was well reproduced in the simulations as shown in Figure 12.

Circular oscillation of the laser beam led also to periodic trend of the velocity of the laser spot. Indeed, forward and oscillating components of the motion had periodically equal (position A in Figure 13) and opposite directions (position C) respectively, resulting in minimum and maximum laser-material interaction time. Figure 12 (b, d, f) shows cross sections with M-shaped profiles, which are characterized by two weld roots, that were indicated as “right and left dent” in this work. In both experimental and simulated cross sections shown in Figure 12 (b, d, f), weld penetration of the left dent was deeper of those in the right one as the laser-material interaction times were maximum and minimum, respectively. Figure 12 (a, c, e) shows cross sections with V-shaped profile, which have just one dent in the centreline of the weld as the connection between the thin-sheets was established when the laser processed them in two consecutive wobbling periods as shown in Figure 13 (a).

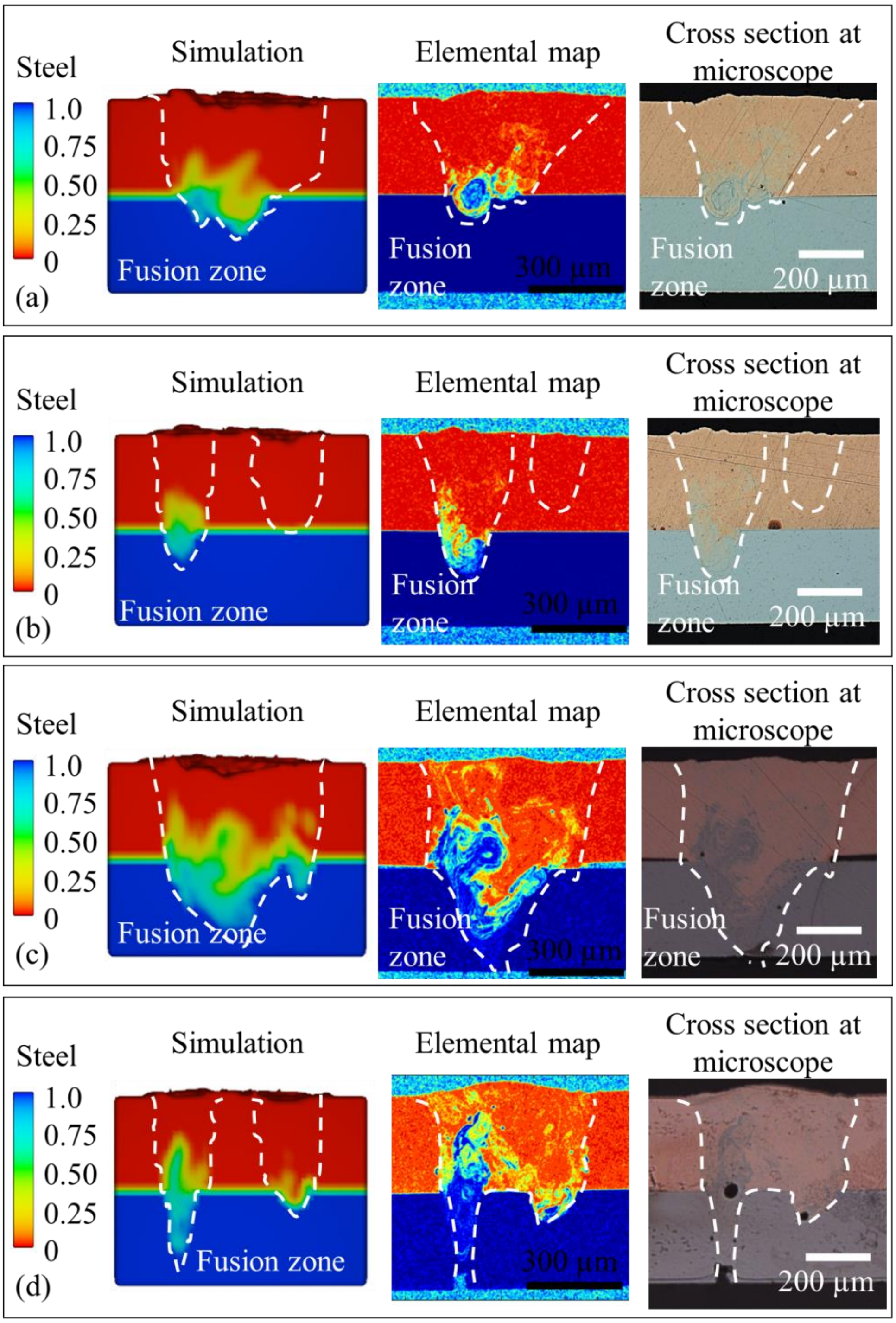

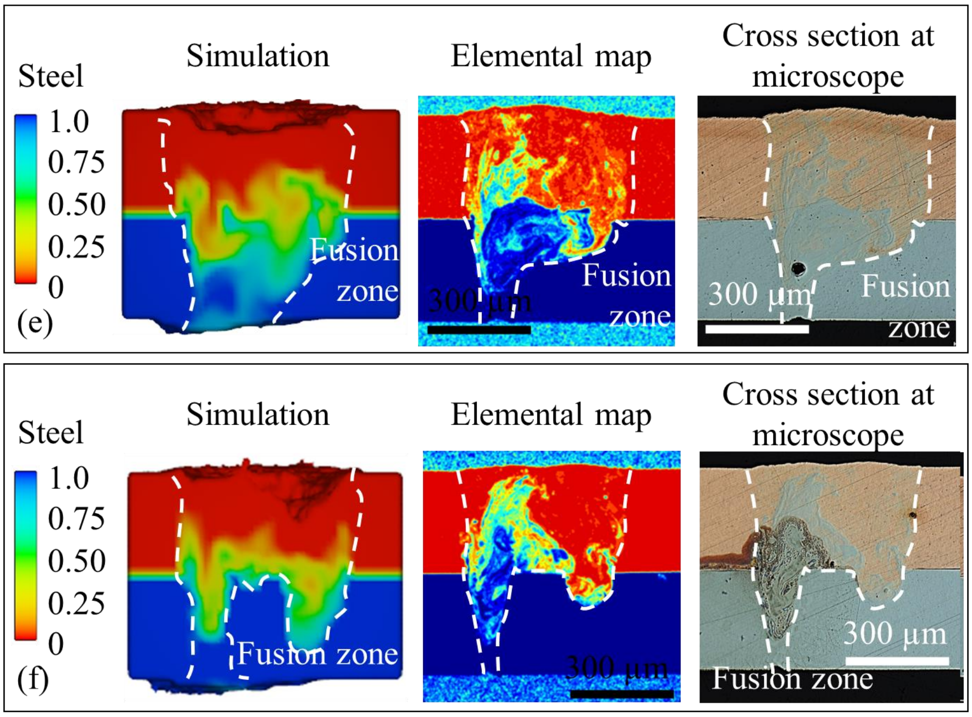

Figure 12 - Comparison of metal mixing and weld profile in experimental and simulated cross sections with part-to-part gap= 0 µm, and P_L= 615 W (a) and (b), P_L= 690 W (c) and (d), and P_L= 765 W (e) and (f).

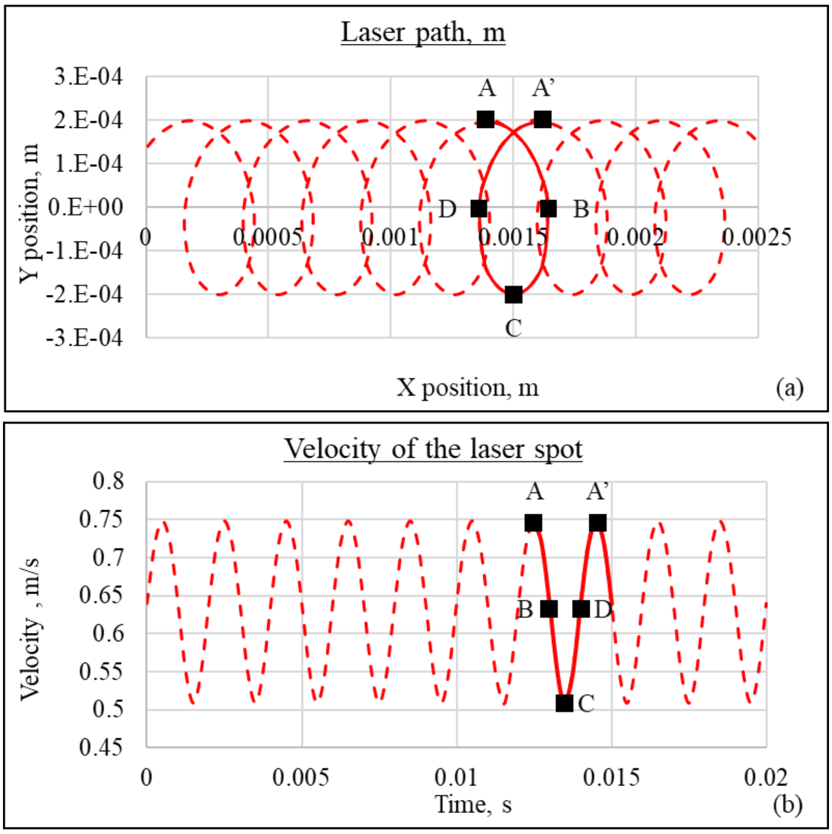

Figure 13 - Definition of positions A, B, C and D with respect to the pattern of the laser spot (a); velocity of the laser spot (b).

Periodic trend in the laser-metal interaction time, was reflected also in the mixing mechanisms. Indeed, when the interaction time was longer, more intense evaporation led to greater recoil pressure which enhanced mixing, as shown in Figure 12 (b, d, f), in which the left dent was deeper with steel being pushed upward in the copper side; additionally, the higher the laser-metal interaction time, the greater the amount of metal that was melted and involved in the mixing. Also, the mass density of copper is greater than the density of steel and this seemed to enhance the mixing with buoyancy forces contributing to the convective flows, in both the simulations and the experiments. Figure 12 (b, d, f) show copper sinking in the steel side and steel flowing to the top of the molten pool.

In Figure 12 (a, c, e), more chaotic patterns in the mixing with parent metal seemed to be the result of two factors: (i) melting occurs twice, and (ii) in the same region. Indeed, in these cross-sections, mixing between parent metals occurred in one fusion zone, whereas in cross sections with M-shaped profile, it occurred in two distinguished and smaller melt regions, involving less metal melting. Additionally, two melting events at different times and in the same region result in enhanced mixing with more complex patterns.

Validation of the model was based on the comparison between geometrical features measured during metallographic analysis and the results of the simulated weld seam. To account variability, 95% confidence intervals were calculated for each of the geometric features considered for all the experimental configurations and are reported in Table 6.

Geometric features of the cross sections were predicted with an error lower than 17% with the only exception of width at interface between parent metals W_{int} when P_L= 615 , 690 W. This was explained looking at the cross-sections of the experiments. Indeed, analysis of cross-sections seemed to indicate that due to uncontrollable experimental variations, such as residual surface contamination or local curvature in the thin sheets, during part of the wobbling period, only part of the laser power was absorbed due to decoupling and reflection of the laser beam, and this occurred when the velocity of the laser spot was maximum (laser spot in position A). This interpretation is in good agreement with very low spread in values of W_{int} when P_L=765 W, as the thermal input was greater enough to ensure that the connection is soundly established throughout the entire wobbling period, regardless of the abovementioned local nuisance factors.

Table 6 - Comparison of measured geometric features in experimental and simulated weld profiles.

			W_{top} , µm	W_{int} , µm	D_{pen} , µm
Part-to-part-gap = 0 µm	P_L= 615 W	Experimental	[525 , 567]	[113 , 171]	[68 . 115]
		Simulations	[469 , 486]	[150 , 210]	[72 , 84]
		Error, %	-13	+26.7	-14.9
	P_L= 690 W	Experimental	[535 , 563]	[232 , 378]	[147 , 235]
		Simulations	[475 , 490]	[373 , 407]	[190, 204]
		Error, %	- 12.4	+ 27.6	- 9.0
	P_L= 765 W	Experimental	[536 , 562]	[362 , 426]	300
		Simulations	[478 , 493]	[432 , 437]	[293 , 300]
		Error, %	- 11.7	+ 10.3	- 1.67
Part-to-part-gap = 100 µm	P_L= 690 W	Experimental	[530 , 552]	[154 , 263]	[92 , 180]
		Simulations	[529 , 534]	[216 , 270]	[107 , 119]
		Error, %	-1.7	16.3	- 16.8

3.4.1.2 Simulations of weld experiments with variable weld penetration depth and without part-to-part gap

After calibration and validation of the model, subsurface features of the process that are difficult to directly measure, such as temperature and velocity fields, and mixing mechanisms, were analysed and correlated with results of ex-post analysis of the cross-sections to better understand phenomena involved in the welding process.

Laser power P_L= 615 W, resulted in poor weld penetration depth, whereas P_L=765 W led to over-penetration of the thin sheets with the risk of piercing adjacent components in industrial applications. Simulations reproduced this trend in weld penetration depth with good approximation as shown in Figure 12 and Figure 14, and as reported in Table 6. Simulations with laser power P_L= 690 W led to sound weld without over-penetration. Therefore, detailed analysis of thermal and velocity fields predicted with simulation focused on S2.

In Figure 15, temperature and mixing between parent metals were plotted for four timeframes within a wobbling cycle, which correspond to positions A, B, C and D of the laser spot that are defined in Figure 13. In these timeframes the laser spot had respectively maximum, average, minimum and average velocity. Therefore, the effects of the wobbling on the process were explicitly captured in the plots, which show longitudinal sections of the process zones with the section-planes being tangent to the laser trajectory. In Figure 15 (b) projected in-plane components of the velocity field in the molten pool were reported with black arrows along with the mixing between parent metal, to highlight mixing mechanisms.

From Figure 15 (a) it is clear that the regions where the laser interacts with the metal on the keyhole walls, had the highest temperatures. Power absorption occurred due to direct exposition and due to multiple reflections, as shown in time-frame t= 0.009 s, leading to the formation of the bulge in the back-walls (timeframe t= 0.0095 s) of the keyhole that can eventually collapse (timeframe t=0.010 s).

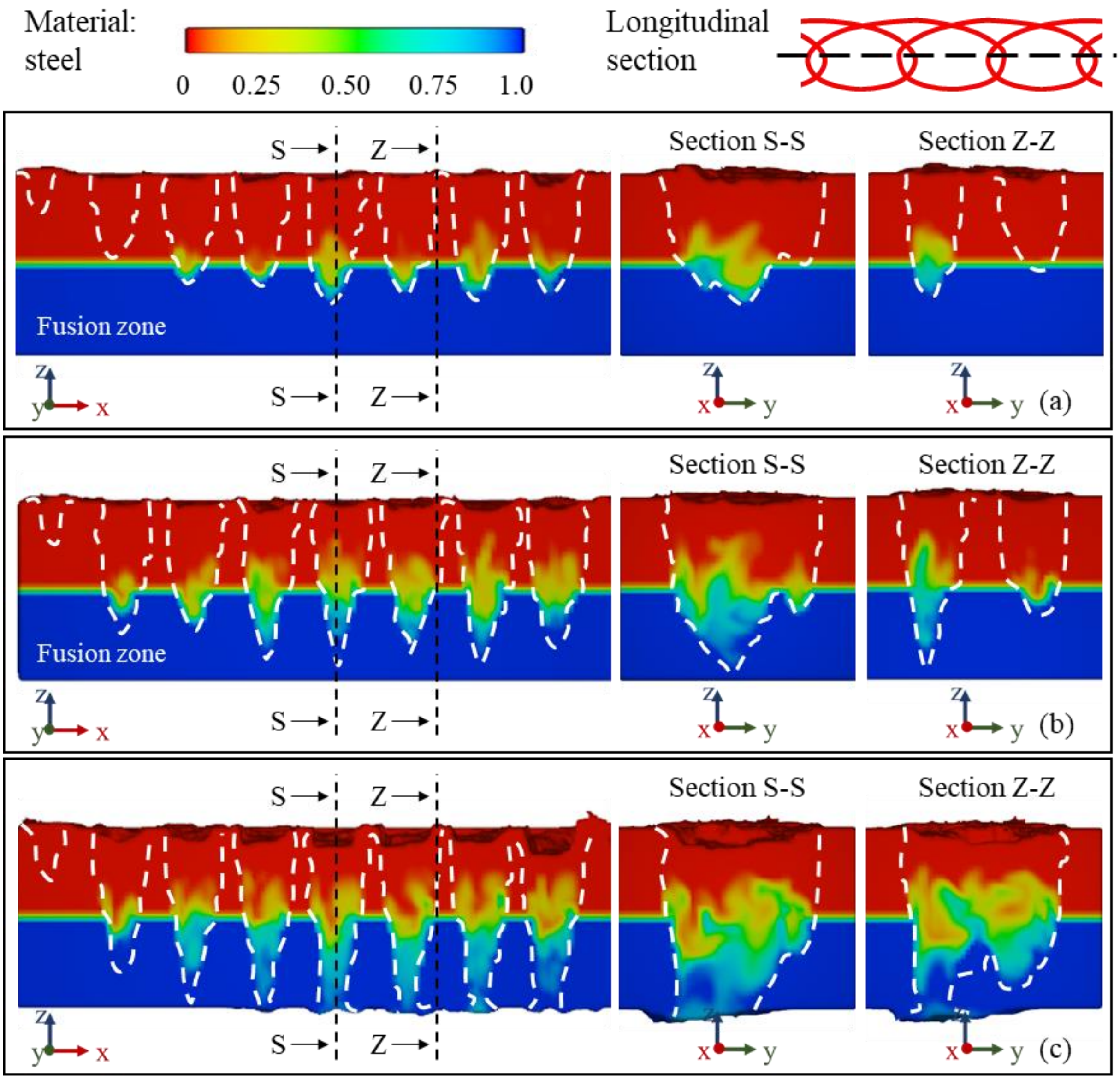

Figure 14 - Longitudinal and cross sections of simulations of the experiments with P_L= {615 . 690, 765} W, in (a), (b), and (c) respectively.

As exposition time to the laser of the process zone varied during the wobbling period, different weld penetration depth was achieved. Indeed, when the laser was in positions A and C, the exposition times were respectively minimum and maximum, with respectively lower and greater thermal power absorbed and resulting in different weld penetration depth. However, another effect of the periodic trend in the thermal fields of the process zone was determined by the circular wobbling and should be taken in account in this analysis. During a wobbling period, the laser spot first melted new metal warming-up the material around when it was in position B, then came back to metal that was melted in the previous wobbling cycle, and finally processed it again when it was in position D. In this position, weld penetration depth of the keyhole is maximum and fusion zone had the greatest extension with maximum material mixing. All these periodic variabilities in the thermal input of the welding resulted in periodic trend in the size of the keyhole and of the fusion zone, with consequences on the size of the melt pool and on the mixing. Longer laser-metal interaction times and local re-melting led ton longer time in which metals stayed in liquid phase with extended mixing-time.

Metal mixing was driven by velocity fields in the molten pool, with several factors contributing, such as the recoil pressure, the Marangoni effect and the laser pattern [40]. Longer black arrows in the vicinity of the highest temperature spots where the laser power was absorbed by the metals, showed that the fluid had higher velocities due to the action of the recoil pressure, which was enhanced due to more intense evaporation. A general trend can be distinguished in fluid flow and was explained accounting the action of the recoil pressure. Indeed, it pushed the molten metal at the bottom of the keyhole which flowed upward toward the free surface where it was deflected by the solid metal that hold the melt pool (grey dashed arrow), and from the keyhole walls toward the outer region of the melt pool. Deflection of upward flow led to vortices (timeframes t= 0.0090 s and t= 0.0095 s) which enhanced mixing between parent metals. Collapse event in the keyhole enhance mixing between parent metals and results in flow moving toward the centre and the bottom of the keyhole with less defined patterns in the velocity field, as shown in timeframe with t=0.010 s.

Marangoni forces, in this model were generated by gradients in the surface tensions due to thermal gradients only. Metal on the surface of the molten pool is driven from the high-temperature to the low-temperature areas. However, in this welding configuration with circular wobbling, liquid metal flow due to the Marangoni forces were not clearly distinguishable as effects of the recoil pressure seemed to prevail.

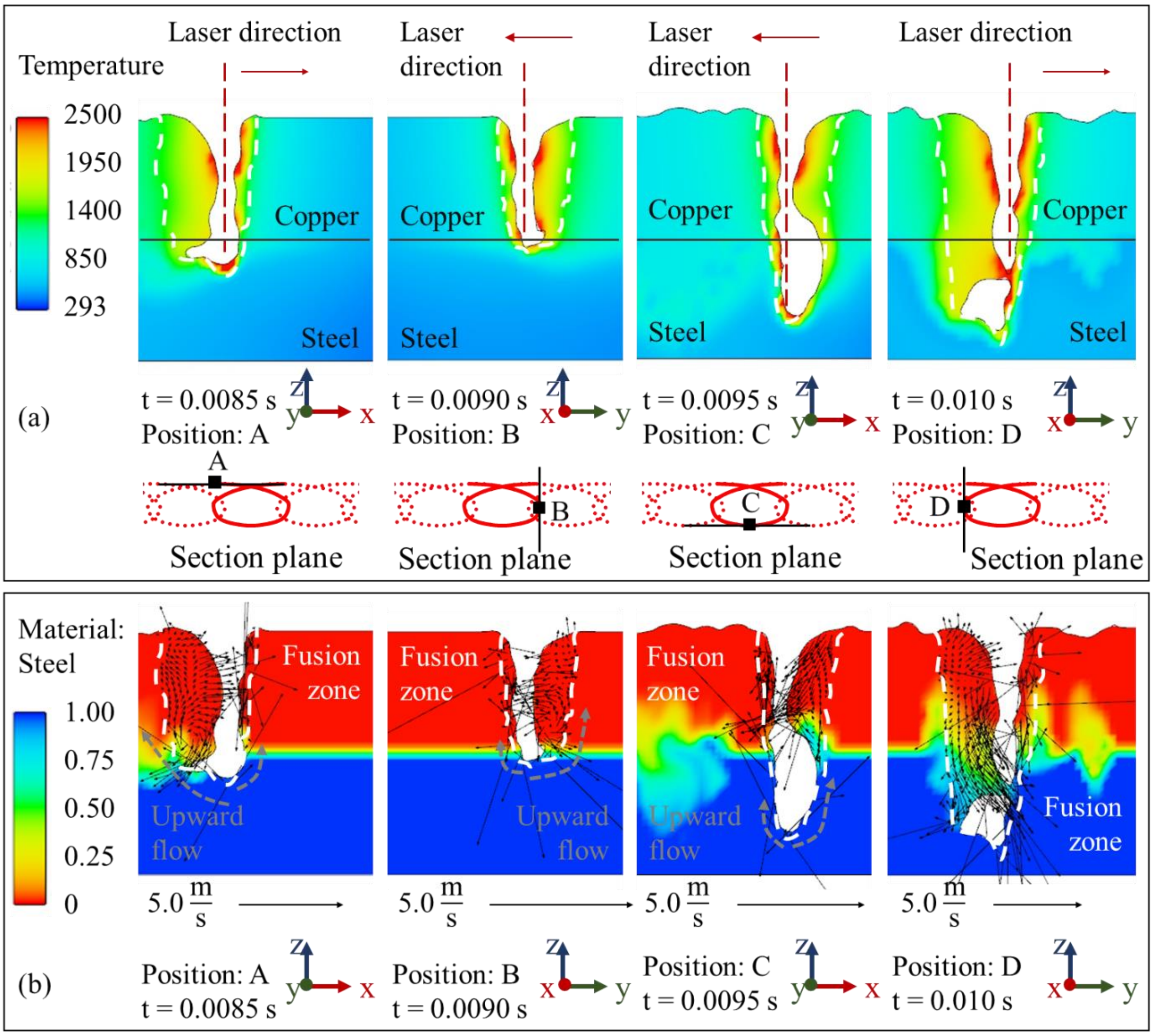

Figure 15 - Plot of the temperature (a) and of the material mixing with projected velocity field in the section plane (b). Part-to-part gap = 0 µm and P_L= 690 W.

3.4.1.3 Simulation of weld experiment with part-to-part gap

Calibrated coefficient Ar in equation (4) was sensitive to the occurrence of part-to-part gap. Indeed, when there is no gap, the keyhole extends throughout the metallic thin sheets and the melt pool is entirely enclosed in the solid metal substrate, whereas, when it extends throughout the part-to-part, it is not. Pressure, acting on the internal walls of the keyhole pushes the metal with different equilibrium scheme that is different in the cases of welds with and without part-to-part gap. In the cases of welds with part-to-part gap, pressure acting on the keyhole walls ultimately results in a “curtain effect” that was observed also in other researches [48]. Calibration of Ar for scenario S4 led to a value of 15195 Pa.

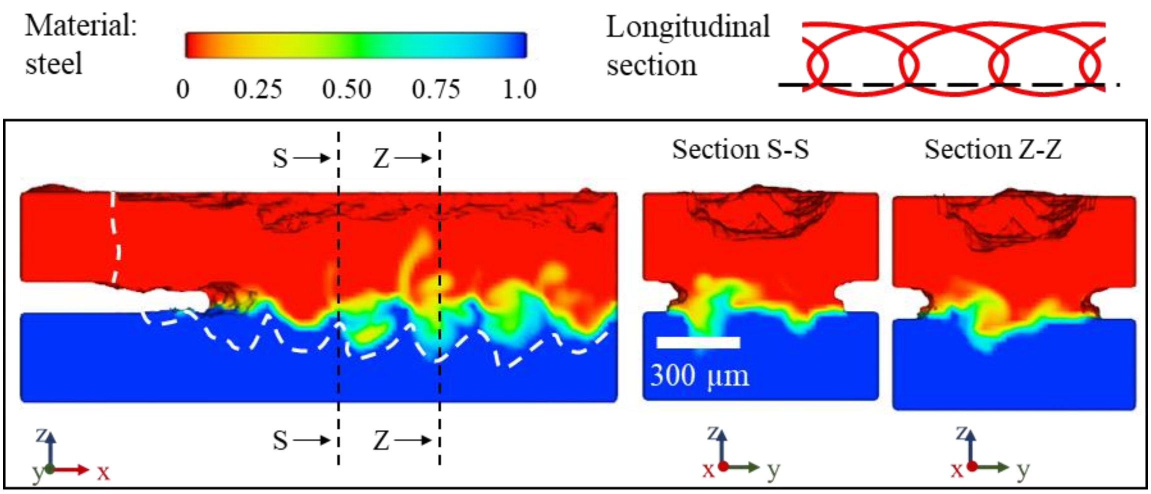

Figure 16 - Longitudinal (-0.2mm offset from centreline) and cross sections of simulations of weld experiment with P_L= 690 W and part-to-part gap = 100 µm.

Comparison between the results in Figure 14 (b) and Figure 16 shows that the part-to-part gap delayed the bonding between the sheets and influenced the dynamics involved in the process. When the laser process started, in simulations with zero gap (Figure 14 (b)), the copper sheet melted and transmitted part of the heat to the adjacent steel sheet, which behaved as heat sink; conversely, in case of part-to-part gap, the heat transfer from copper to steel was delayed due the presence of the gap, which acted as thermal barrier. Additionally, as the laser moves forward, the molten region on the copper side increased in size and was subject to three actions: (i) the gravity force that caused motion of the molten copper towards the bottom determining contact with the steel foil; (ii) the internal friction due to viscosity forces that contrasted any motion and relative slips; and (iii) the surface tension with cohesive forces applied to the surface layer of the molten region. Only when the amount of molten copper increased, gravity prevailed on viscous stresses and surface tension, and connection of the thin sheets occurred, thus enabling gap bridging. Once the connection was established, the weld profile developed, and it was characterized by a double dent/M-shaped.

The effects of part-to-part gap are discussed below with respect to joining mechanism, temperature field and mixing mechanisms.

3.4.1.3.1 Connection between parts

Figure 14 (b) and Figure 16, show that the weld penetration depth was significantly lower in case of part-to-part gap. In simulations with zero gap (Figure 15), the keyhole was established and extended to both the upper and lower sheets, and, therefore, a sound connection was created. In case of part-to-part gap (Figure 17), the results showed that each cycle of the wobbling pattern was divided in two phases: first, the laser warmed up and melts unprocessed metal, which eventually flowed on the lower sheet, and then, while the laser processed again the metal a connection between the two sheets was soundly established. Periodical connection between sheets in the case of part-to-part gap matched well experimental results, as cross-sections with both sound weld and lack of connection were observed within the same seam.

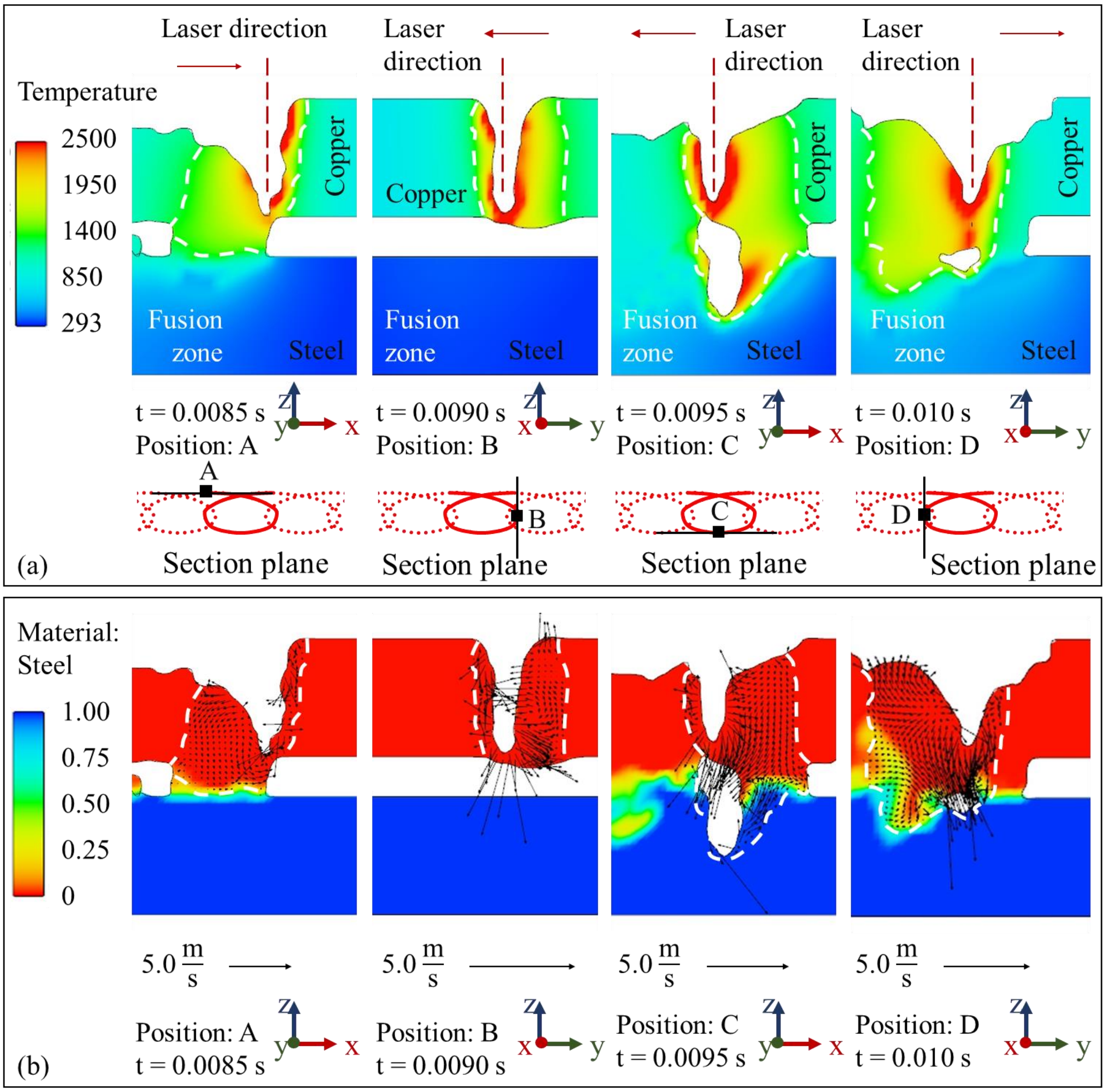

Figure 17 - Plot of the temperature (a) and of the material mixing with projected velocity field in the section plane (b). Part-to-part gap = 100 µm and P_L= 690 W.

3.4.1.3.2 Temperature field

Figure 15 (a) and Figure 17 (a) show that the presence of part-to-part gap resulted in different thermal fields. The highest temperature was achieved on the keyhole walls, due to interaction with laser and multiple reflections, and the heat was transmitted to the surrounding metal. However, in simulation with no gap, direct contact between the two sheets enhanced heat transfer (Figure 15 (a)). In case of part-to-part gap, there was no direct contact between the two sheets and the heat transfer was only ensured by the weld seam that bridged the gap; this resulted in lower temperatures in the steel foil (Figure 17 (a)).

3.4.1.3.3 Metal mixing

Figure 15 (b) and Figure 17 (b) show that different thermal fields resulted in different metal mixing mechanisms. Projected velocity fields were represented with black arrows and both recoil pressure and temperature distribution seemed to drive fluid flow. Arrows in the vicinity of the keyhole walls indicated that the recoil pressure drove the fluid from the bottom of the keyhole to the top and towards the outer region of the melt pool. The thermal gradient due to the rotation of the keyhole (consequence of the circular wobbling) determined a flow that was represented with the projected velocity field. Figure 15 (b) (no gap) showed that the metal flow involved both copper and steel and enhanced mixing throughout all the wobbling cycle in case of no gap. Figure 17 (b) (gap=100 μm) shows that the metal flow involved steel in a limited part of the wobbling cycle. This resulted in uncontrolled metal mixing and periodical discontinuity in the properties of the weld seam.

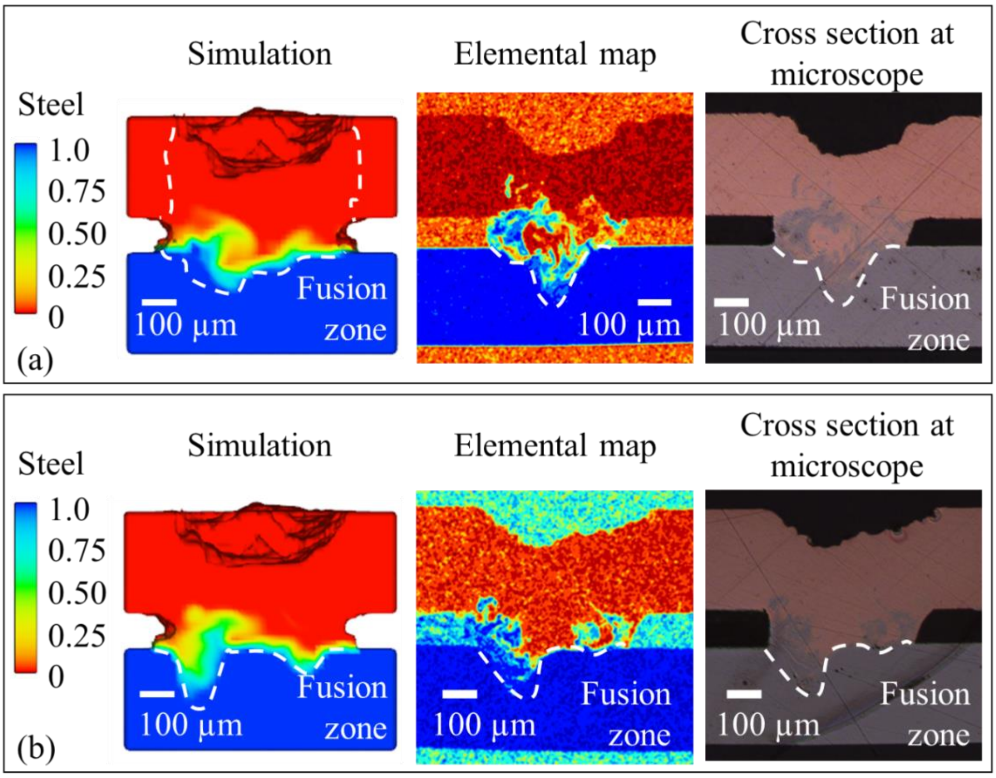

Figure 18 - Comparison of metal mixing and weld profile in experimental and simulated cross sections with PL= 690 W and part-to-part gap =100 μm.

3.4.1.4 Summary of key findings on simulation of weld experiments

In this sub-sections, main findings of experimental-numerical study on Set #1, are summarised in bullet form to ease a more comprehensive and structured view of the results:

- Circular oscillation of the laser beam wobbling resulted in periodical variability in the weld seam with V and M-shaped profiles.
- Periodically variable velocity of the laser spot during the wobbling period caused variable laser-material interaction time and thermal input in the process zone, which led to variable weld penetration depth and size of the melt pool.
- Experimental and numerical results confirmed that the higher the laser power the more intense the evaporation, leading to greater recoil pressure that resulted in enhanced mixing due to higher velocity of flows in the melt pool.
- Upward flow and buoyancy forces were the main mechanisms that cause migration of the steel in the copper side of the melt pool.
- Part-to-part gap delayed the first connection between thin sheets which is governed by surface tension, viscosity stress, and gravity force.
- Part-to-part gap limited heat transfer from the copper to the steel sheets, resulting in lower temperatures in the steel and heat localization in the copper.
- When gap is zero, connection between sheets was established throughout the whole wobbling cycle; whereas, in case of part-to-part gap, the connection was established periodically, since the laser penetrates only the upper sheet during part of the wobbling cycle. This led to uncontrolled metal mixing.
- The wobbling pattern and the sub-consequent periodic variation of laser beam velocity determined inhomogeneity in the metal mixing due to variation in the penetration depth, temperature fields and amount of molten metal.

3.4.2 Simulations of welding with selected laser beam shapes

List of the simulations in Table 5, reports the iterative process for selection of the values of laser power P_L for each of the considered welding configurations. The following discussion focused on the results of those configurations which achieved the requirement of $D_{pen} \geq 90$ μm, which are: LBS1-ID5, LBS2-ID8, LBS3-ID6, and LBS4-ID1. They were analysed separately in dedicated subsections, with key findings summarised in conclusive subsection.

3.4.2.1 Discussion on combined ring-shaped secondary beam and primary beam

Longitudinal and cross sections of LBS1-ID5, LBS2-ID8, and LBS3-ID6 reported in Figure 19 (a, b, c) show the following trend: use of a ring-shaped secondary laser beam resulted in wider interface between parent metals and lower weld penetration depth; this trend was exalted when the size of the ring-shaped spot of the secondary laser beam increased.

Figure 19 (a) showed fluctuations in the weld penetration depth and the presence of pores in the weld simulated with LBS1-ID5. These features indicated that the dynamics of the keyhole was affected by collapse events with gas entrapments that led to the formation of pores.

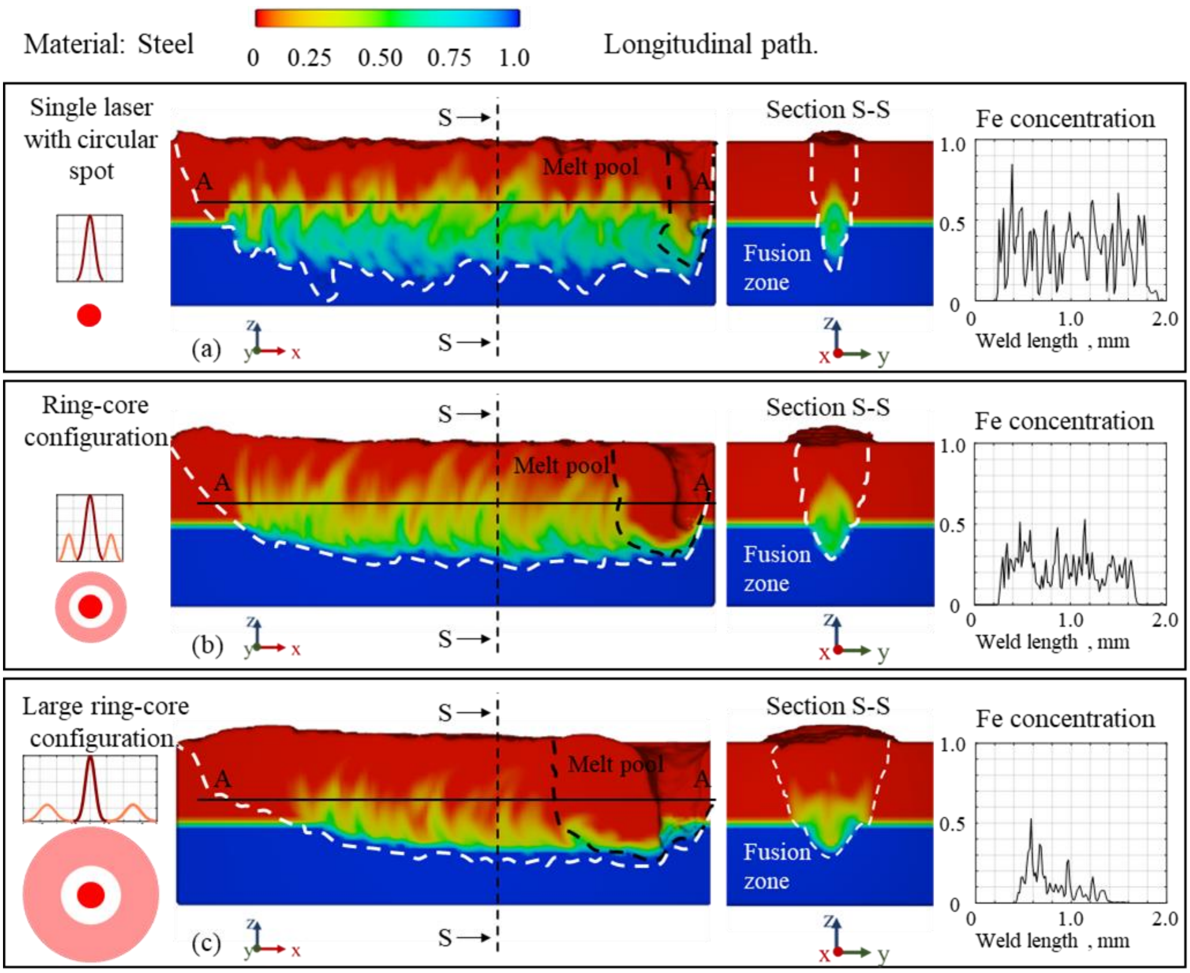

Figure 19 – Longitudinal, cross sections of simulations, and plot of the concentration of Fe (steel) in the Cu-rich side of the molten pool along line A-A for LBS1-ID5 (a), LBS2-ID8 (b), and LBS3-ID6 (c).

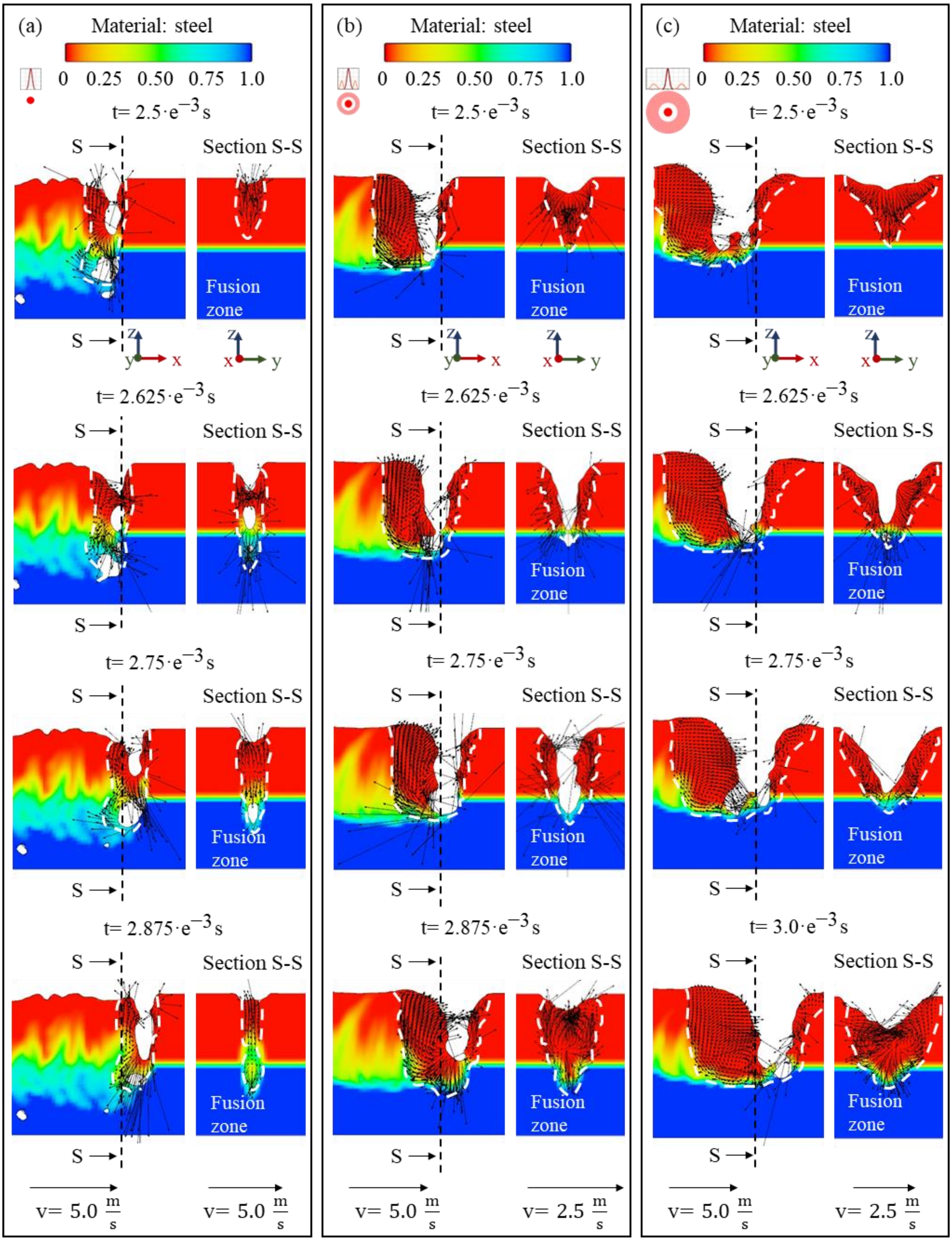

Figure 20 - Metal mixing, fusion zone and velocity fields in consecutive timeframes of LBS1-ID5 (a), LBS2-ID8 (b), and LBS3-ID6 (c). Black arrows represent the projected velocity fields in the section plane.

Figure 20 (a) shows 4 consecutive timeframes of LBS1-ID5, with projected velocity fields represented with black arrows and contour plot of concentration of parent metals. It reports the mechanism of entrapment of gases in the keyhole. Intense recoil pressure pushed molten metal from the bottom of the keyhole, which was deflected by the solid metal substrate, resulting in upward flow which eventually collapsed toward the centre of the keyhole (timeframes t= 2.625e-3 , 2.75 e-3). Furthermore, due to these collapse events, the irradiated surface on the keyhole walls changed with different exposure to the laser power and multiple reflections. Ultimately, these changes resulted in different thermal field and evaporations that caused fluctuations in the weld penetration depth that are shown in Figure 19 (a).

Use of a ring-shaped secondary beam combined with the primary one allows to spread the thermal input on a wider surface, which led to larger melt pool, and ultimately width at interface between parent metals, as mentioned above and shown in Figure 19 (b).

Less localised thermal input in LBS2-ID8 resulted in wider shape of the of the melt pool and also in less intense evaporation, which were both reflected in lower deflection of the upward flows, that ultimately resulted in lower occurrence of collapse events of the keyhole which, therefore, had a more stable dynamics with reduced oscillations, as shown in Figure 20 (b). Predicted stabilisation of the keyhole dynamics resulted in no entrapment of gases and pores formation. In particular, projected velocities in time frames in Figure 20 (b), show that liquid metal involved in upward flow migrated toward the tail of the melt pool, and then was deflected toward the centre, leading to forward flow. Forward and upward flows, collaboratively generated vortices that contributed to metal mixing, as upward flow carried liquid steel in the upper side of the melt pool. However, comparison showed that upward flow in LBS1-ID5 led to formation of Fe-rich clusters in the Cu-rich side of the weld seam, which were not predicted in LBS2-ID8, indicating less sever mixing with potential formation of IMCs.

Use of a wider ring-shaped secondary laser beam led to even less localised thermal input with significant impact on the process as visible by comparing Figure 19 (c) to Figure 19 (b). Larger melt pool resulted in larger width of the weld seam at interface between parent metals (approximatively equal to 250 μm) and smaller weld penetration depth in the lower sheets. This was explained considering that the distance between the regions of the keyhole walls that are irradiated by the primary and the secondary laser are such that the evaporation and the keyhole were not localised anymore.

Larger size of the molten pool also impacted the mixing mechanisms, as the metal stayed in the liquid phase for longer, with more time available for mixing. Beside vortices collaboratively created by upward and forward flows, cross section in Figure 19 (c) and in time frames of Figure 20 (c) shows that recoil pressure pushed the liquid metal at the bottom of the keyhole also toward the side of the melt pool, leading to vortices in the y-z plane that contributed to mixing.

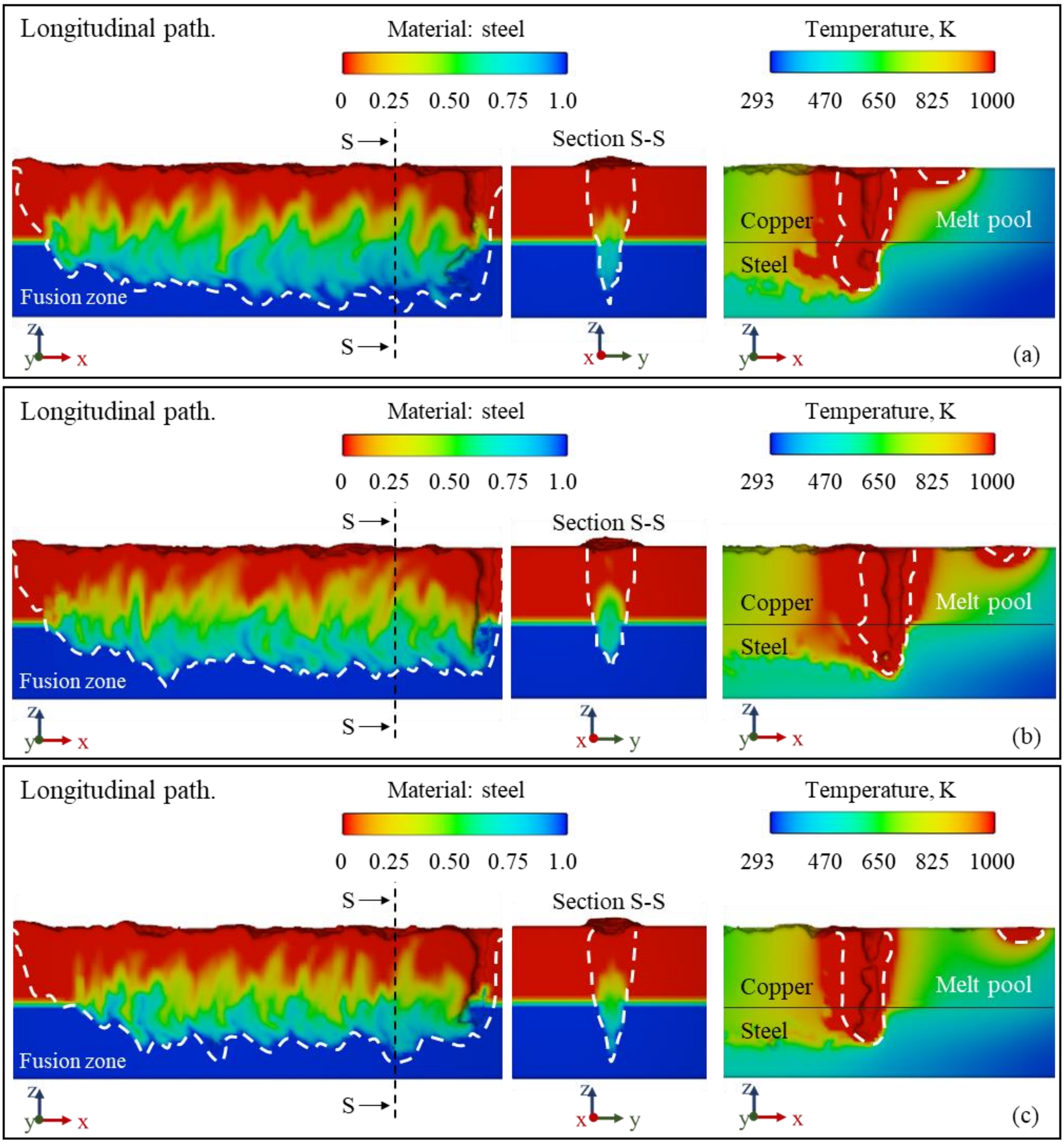

Figure 21 - Metal mixing, fusion zone and temperature fields from simulations for LBS4-ID1 at D_T= 0.3 (a), LBS4-ID2 at D_T= 0.45 (b) and LBS4-ID3 at D_T= 0.6 mm (c).

3.4.2.2 Discussion on dual laser beam in tandem configuration

LBS4 simulated a tandem beam arrangement with the primary laser establishing connection between the parts by processing a region after that the secondary beam pre-heats it. Three different values were considered for the distance between the two laser beam, with significantly different thermal fields between the two lasers: (a) T ≥ 1000 K for D_T = 0.3 mm, (b) T ≥ 850 K for D_T = 0.45 mm, and (c) T ≥ 650 K for D_T = 0.6 mm, as shown in Figure 21.

These variations resulted in marginal differences in the weld profile simulated in the three cases. Additionally, results of LBS4-1,2, and 3 were not significantly different from LBS1-5 indicating that this weld strategy did not contribute much to process improvement.

3.4.2.3 Summary of key findings on simulations with shaped laser beams

Figure 22 reports and compare quantitative data that were discussed in previous subsection and were used to support main findings. These data are: (a) weld penetration in the bottom thin sheet, (b) width of the seam at interface, (c) average concentration of Fe in the copper side of the weld at the centreline (f), and in the entire copper side of the fusion zone, average cooling rate (d), and average temperature of the molten pool. Main findings are discussed as follow:

- Simulations LBS1-ID5 and LBS4-ID1 resulted in weld seams that have very similar geometric features and properties. LBS4-ID1 predicted weld penetration depth equal to 196 μm, width at interface equal to 100 μm, and concentration of Fe in the copper side of the weld at the centreline equal to 17.20%, which are values very close to those predicted with LBS1-ID5.
- Different welding strategies seemed to not impact the average temperature in the melt pool much, however, the use of secondary laser beam seemed to significantly reduce the cooling rate, as they resulted in melt pool with greater size.
- In welds with combined ring-shaped secondary and primary laser beams, concentration of Fe at the centreline in the Cu side was significantly lower (approximatively 10.5% and 4.1% in LBS#2-ID8 and LBS#3-ID6, respectively). However, to account different extensions of the fusion zones, also average concentration of Fe in the Cu side of the entire fusion zone was estimated (Figure 22 (f)). In LBS#1-ID4 and in LBS#4-ID1, the concentration of Fe at the side of the weld seam were respectively equal to 7.7% and 7.9%; whereas, LBS#2-ID8 and LBS#3-ID6 achieved 7.2% and 6.3%, respectively. This confirmed that use of secondary ring-shaped beam tends to reduce the mixing effect, but also indicated that in the case of welding with single beam (LBS#1) and tandem configuration (LBS#4), metal mixing occurs with Fe-rich clusters and structures, all located at the centreline of the weld seam. Notably, the concentration of Fe obtained with a ring-shaped beam was comparable to the one achieved with an inner-only beam in conjunction with beam wobbling (E1-E3).

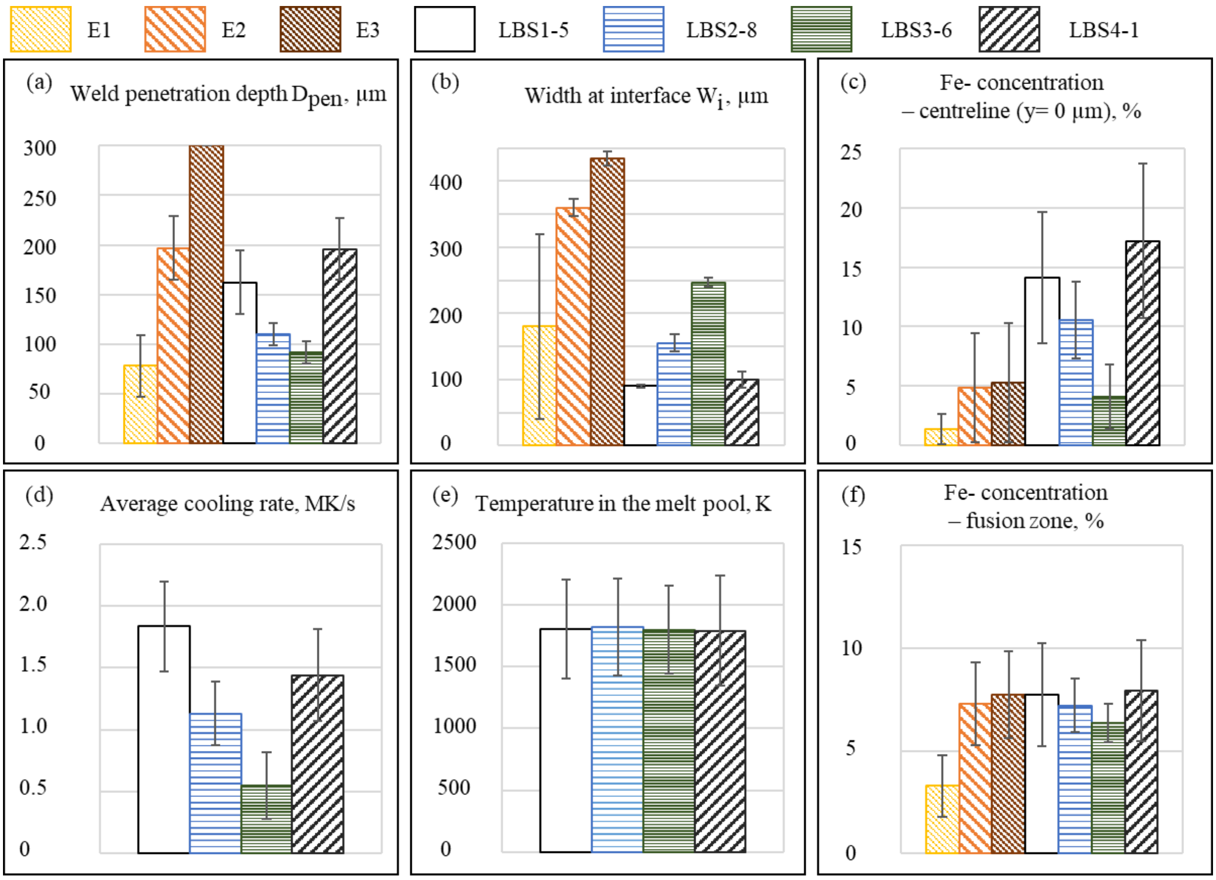

Figure 22 - Key features of simulated welds.

3.5 Conclusions and opportunities for future research

This chapter addressed the development of a multi-physics CFD model of RLW of 300 µm copper to 300 µm nickel-plated steel to investigate the complex phaenomena involved during the process by analysing simulated subsurface features, such as temperature fields, velocity fields and mixing between parent metals, which are all difficult to directly measure via in-situ observations due to technological difficulties.

Two sets of simulations were carried out to evaluate the impact of uncontrollable variations of the part-to-part gap and opportunities for process improvement by implementation of different welding strategies.

Experimental-numerical approach allowed to validate the model with geometric features of the weld profiles and EDS elemental maps, that were prepared from experiments of Set #1, which included four scenarios with variable weld penetration depth and part-to-part gap. Comparison of simulations with variable laser power, with and without part to-part gap (0 and 100 µm) was presented to investigate its impact and the impact of laser beam wobbling on temperature and velocity fields, melt pool dynamics, mixing and connection mechanisms. Then, the validated model was employed to investigate opportunities for improvement of the process via laser beam shaping by simulating linear welds with combined primary and secondary laser beams in ring/core and tandem configurations. Key concepts are summarised as follow:

- Circular oscillations of the laser beam wobbling resulted in periodical variability in the geometrical shape of the weld seam, due to the pattern of the laser beam and to the periodically variable velocity of the laser spot.
- Mixing between parent metals was enhanced by flows that were driven by recoil pressure, which changes with variable laser-material interaction time, and buoyancy forces.
- Part-to-part gap delayed the first connection, limited heat transfer from the copper to the steel sheet and caused periodically discontinuous penetration of the laser in the lower thin sheet, which also resulted in uncontrolled metal mixing.
- Simulations of a ring-shaped secondary laser beam predicted more distributed thermal input which led to larger melt pool, stabilisation of the dynamics of the keyhole, and reduction of the cooling rate, if compared to the case of welds with only primary beam used. Also, different velocity fields resulted in reduced mixing between parent metals.
- Simulations of welds with tandem configuration were implemented which led to predicted results very similar, in terms of geometry of the weld seam and metal mixing, to the case of welds with primary beam only. For this reason, use of a secondary laser beam that pre-heats the metal before the primary one establishes connection did not seem to contribute much to process improvement.

Next step of this research stream is the development of models and methods that enable fusion of data inferred from simulations and data gathered from sensors for full development of a digital twin of the process. This would contribute much to the full developments of a control system with significant impact on manufacturing applications.

Further development of this research is planned and includes a dedicated experimental-numerical study on the mechanical behaviour of these weld joints. This study aims to investigate the effects of incontrollable variations of part-to-part gap on the static and the fatigue strength. It could contribute also to the research field of the digital certification of mechanical properties to meet requirements by integrating FEM models and geometry of the weld seam that was predicted with the present approach.

Chapter 4

4 Characterization of photodiodes to variations of part-to-part gap and weld penetration depth

4.1 Introduction

This chapter addressed characterisation of a photodiode-based sensor to assess its capability to detect variations of weld penetration depth and part-to-part gap so that in-process monitoring system for RLW of battery tab connectors can be implemented. Interest in monitoring these incontrollable variations, that can affect the process during laser welding of dissimilar metallic thin sheets, stems in the following challenges:

1. To limit mixing mechanisms and prevent formation of Intermetallic Compounds (IMC). Mixing of parent metals occurs during laser welding with dissimilar metals which can have different physical properties resulting in segregation and precipitates, poor compatibility and miscibility, and poor joint strength.
2. Clamping and manufacturing tolerances can lead to a cumulated part-to-part gap, such that it is greater than the thickness of the sheets, and therefore, can result in lack of connection between the parts.
3. Management of the thermal input during the weld process to prevent over-heating or over-penetration, that, ultimately, can cause damage to adjacent components with the risk of explosion and fire.

Challenge 1 was addressed in the previous chapter, that contributed toward investigation of mixing between parent metals and formation of IMCs, and therefore it was not discussed in detail this chapter. Challenges 2 and 3 are interrelated with each other because variations in weld penetration depth and part-to-part gap can affect the weld joint from both a mechanical and electrical point of view, as schematised in Figure 23, with detrimental effects on the safety of the process. Lack of connection and excessive seam concavity can be caused by variations of the part-to-part gap, which may be determined by the combined effect of geometrical variations and small thickness of the sheets. The urgent need to detect variations in the weld penetration depth stems in two reasons: first, excessive weld penetration depth (Figure 23 (c)) brings the risk of piercing adjacent components (electrodes, etc.), with subsequent leakages of harmful gases and fire; second, lack of penetration (Figure 23 (b)) is associated to drop in electrical connection with subsequent reduction in electrical conductivity. The variation in weld penetration depth is the cumulative effect of variations in laser power, focal point shift, material reflection, etc. [51].

Photodiodes have relatively simple structure, low cost and they are suitable for applications in industrial environment. Indeed, they have been largely employed to monitor RLW of metallic sheets with thickness greater than 1 mm [52].

In this chapter, characterisation of a photodiode-based sensor to variations of part-to-part gap and weld penetration depth was reported to demonstrate capability of the sensor to isolate and diagnose weld defects. The investigation focussed on RLW of copper-to-steel thin sheets lap joint (copper 300 μm to Ni-plated steel 300 μm), as those materials are widely used for manufacturing of battery cells and tab connectors.

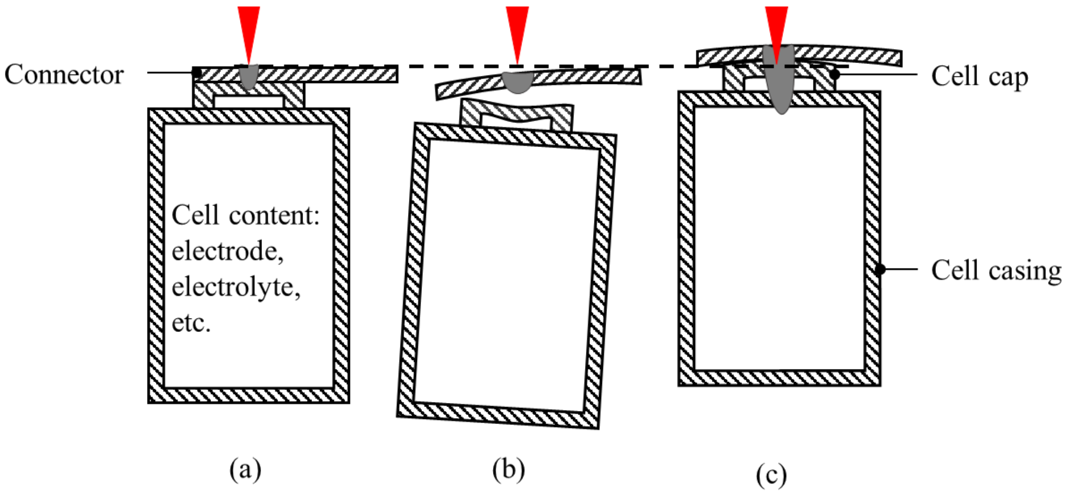

Figure 23 - Typical design of a cylindrical cell and tab connector. (a) ideal welding condition, actual welding condition with lack of connection due to part-to-part gap (b), and over-penetration (c).

4.2 State of the art

Although RLW, has significant superiority in automatization, an important challenge to overcome is the limited or insufficient capability for in-process quality monitoring and control [27]. The quality of RLW weldments is generally assessed by measuring multiple features classified as: (1) surface features (surface spatter, blowout, melt pool width, upper and bottom concavity, seam discontinuity); and, (2) sub-surface features (weld penetration depth, weld connection, porosity, crack) [53]. State-of-the-art approaches for in-process monitoring involve the fusion of multiple sensors to detect multiple weld features [54]. For instance, CMOS/CCD camera-based or laser-based sensors are employed for direct measurement of surface features, and thus, they contribute to in-process monitoring by direct observation of the surface features, which is a well-established area [27]. Direct measurement of the sub-surface features still remains outside the reach of sensing techniques, instead. In this context, *Sokolov et al.* [15] employed Adjustable Ring Mode laser beam to weld 450 µm thick aluminium to 300 µm thick copper and Optical Coherence Tomography (OCT) for direct measurement of weld penetration depth. Authors reported that the OCT sensor can enable direct measurement of weld penetration depth with accuracy of 100 µm, when compared to off-line/off-process metallographic analysis. However, evidence indicated that the accuracy of the OCT measurement was highly sensitive to the selection of the welding process parameters. For this reason, the sensor needed to be re-calibrated every time changes in the process parameters were introduced. Additionally, welding in conduction mode with no keyhole would is a scenario in which the OCT sensor would be completely unsuitable for measuring the weld penetration depth.

To cope with sensitivity to process parameters, sensor that passively observe process emissions could be used. They gather indirect signals, via photodiodes, acoustic detectors and/or spectrometers. Signals are then correlated to the weld features via tailored extraction of features from gathered data and statistical and machine learning techniques. *Tomcic et al.* used Gaussian process regressions on acoustic signals to determine the weld depth during bead-on-plate weld on oxygen free copper plates with a thickness of 1mm [55]. With respect to applications with dissimilar metals, *Simonds et al.* demonstrated increased sensitivity of laser induced fluorescence (LIF) over previous spectroscopy-based in-situ monitoring. They implemented LIF the during laser spot welding of aluminium to copper thin sheets (200 µm-thick) to gather data with information on IMCs formation based on detected copper atoms [31].

Photodiodes can detect the radiation from the metal vapor and plasma plume ($\mathbf{S_P}$ signal), the thermal condition of the processed zone ($\mathbf{S_T}$ signal) and the reflected laser light ($\mathbf{S_R}$ signal) [56]. Typical structure of a photodiode-based sensor is schematically reported in Figure 24. The three sensors record the radiation in three distinguished bandwidths. For example, for applications where the laser source emits in the NIR, the typical bandwidths are: $\mathbf{S_P}$ sensor – 300-700 nm; $\mathbf{S_R}$ sensor – 1020-1090 nm; $\mathbf{S_T}$ sensor – 1200-2000 nm. It is worth noting that the $\mathbf{S_T}$ sensor observes the temperature of both molten pool and plasma plume [56].

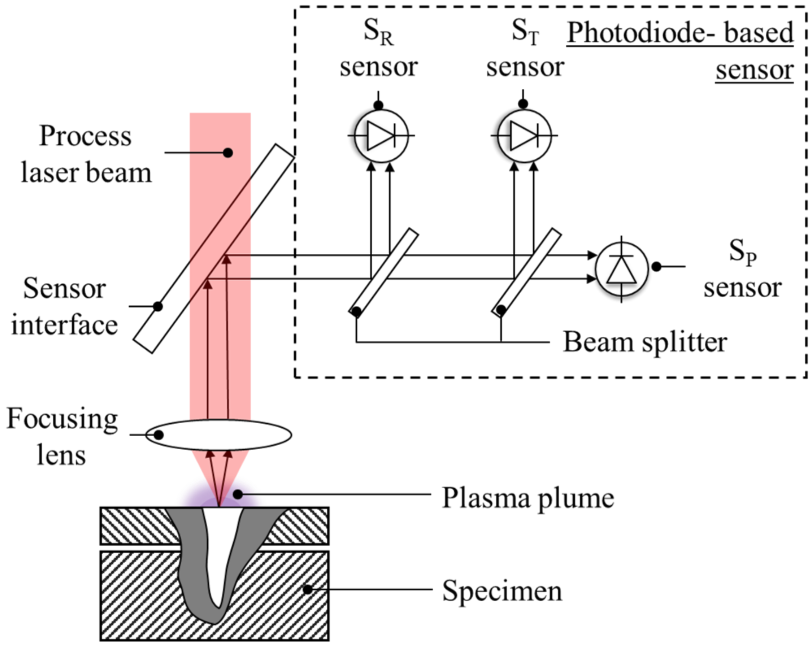

Figure 24 - Standard concept of photodiode-based setup for in-process monitoring of RLW process.

Sanders et al. showed that changes in the weld penetration depth could be monitored with a photodiode that is sensitive to IR emissions [57]. *Eriksson et al.* demonstrated that information carried by signals S_P and S_T can be interdependent as metallic vapour and the plasma plume emit in both the VIS-UV and NIR, and therefore, their emissions are recorded in both the signals. For this reason, they proposed to subtract the two signals S_P to S_T instead of using the raw signal S_T, in order to access the fluctuations in infrared radiation from the melt pool [56]. *Park et al.* used two UV sensors and one IR sensor in order to detect plasma and spatter generated during the laser welding of steel specimens with different thicknesses [58]. Then, they developed a system to perform real time evaluations of the weld quality using a data-driven model based on fuzzy multi-feature pattern recognition. *Rodil et al.* used IR and UV/visible photodiodes to gather data during laser welding of galvanised steels (1 mm thick), and employed them to develop two different approaches for real time process monitoring [26]. *Sibillano et al.* recorded optical emission (300-1,000 nm) during CO2 laser welding of 2 mm - thick steel in butt-joint configuration and performed analysis of the signals in time-frequency domain via DWT to investigate if changes in the frequency oscillations of the signals reflected changes in the weld condition [37]. *De Bono et al.* assessed capability of photodiodes (monitoring wavelength between 600 - 800 nm) to detect variations in the gap, in the surface contaminations and laser power during laser welding of 2 mm thick -nickel in butt configuration [52].

Analysis of literature revealed that photodiode-based monitoring has been mostly implemented for structural welds (i.e., door closures, seat frames and side frames in automotive body construction) with thick parts generally above 1 mm [59]. However, contributions on the application of photodiode-based monitoring in the RLW of dissimilar metallic thin sheets for battery cell manufacturing remain scattered and fragmentated, and characterisation of photodiodes to variation of part-to-part gap and weld penetration depth during RLW of dissimilar metallic thin sheets remains an unexplored area of research [27,28] and will be addressed in this chapter.

4.3 Materials and methods

The experimental campaign consisted of RLW of 300 µm-thick metal sheets (oxygen free C103 copper R240; steel plate cold deep, draw extra, nickel-plated) with a weld length of 40 mm and lap joint configuration. The laser beam pattern was the result of simultaneous linear motion, with a speed of 120 mm/s, and circular wobbling with frequency of 500 Hz and a radius of 0.2 mm. The laser power (P_L) was delivered in CW mode (no power modulation). The laser beam was perpendicular to the specimen (70 mm long and 30 mm wide). No filler wire and shielding gas were employed during the entire experimental campaign. Before the welding trials. samples were wiped with acetone to remove any surface contamination.

The employed laser unit was an nLight Compact Fiber Laser 3kW (nLight Inc., USA) and the laser beam was delivered by a 2D scanner (Scout-200, Laser & Control K-lab, South Korea).

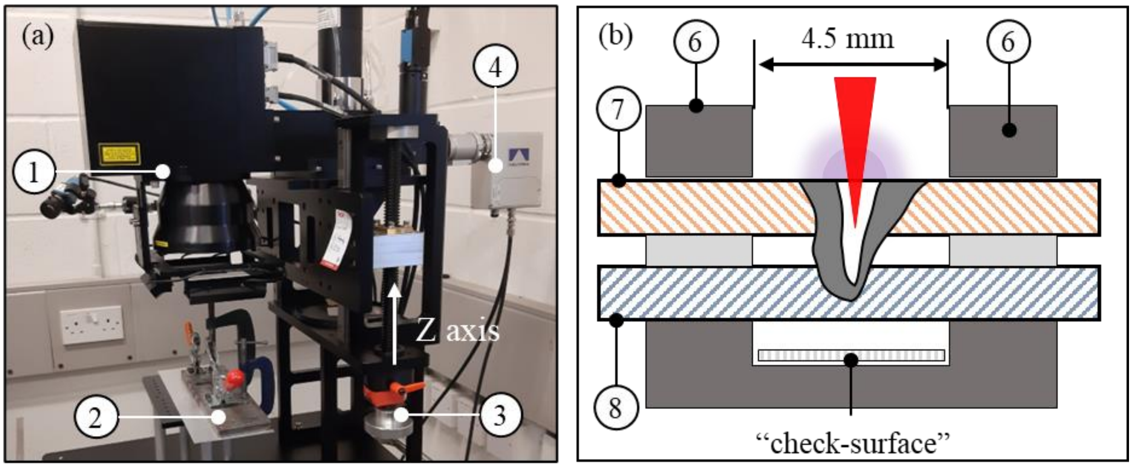

1	Scout-200	2	Fixture setup	3	Z adjustment	4	LWM sensor
5	Shim pack	6	Clamp unit	7	Copper	8	Ni-plated steel

Figure 25- (a) Experimental setup for collecting photodiode-based signals and (b) schematic view of the fixture setup.

The photodiode-based sensor used was the LWM 4.0 (Laser Welding Monitoring, Precitec GmbH, Germany) and it was installed just below the collimator of the scanner, close to the camera port (see Figure 25 (a)). Three signals were collected, namely $\mathbf{S_P}$, $\mathbf{S_R}$ and $\mathbf{S_T}$, with a maximum sampling rate of 50 kHz. The sensor was set so that the region of interest for measurement of optical emissions was the centre of the molten pool/keyhole. Full specifications of the equipment employed during weld experiments are reported in Table 1 and Table 2.

Table 7 - Specifications used for sample preparation with head speed of 60 rpm and applied force of 22 N.

Operation	Grit size [--]	Base speed [rpm]	Time [sec]
Grinding	P400	220	till plane
Grinding	P1200	220	60
Grinding	P2500	220	40
Grinding	P2500	220	40
Polishing	9µm	150	350
Polishing	3µm	150	180
Polishing	1µm	150	120
Polishing	0.6µm	150	90

The focal position of the was controlled by manually adjusting the vertical position of the entire Scout-200 scanner with respect to the mounting frame. In this way, the setting was adjusted to place the focal point at 600 µm above the bottom surface of the steel sheet (see Figure 25 (b)).

A stereo microscope Nikon SMZ18 was used to take pictures of the front and back views for all the weld seams. Then, they were cut to obtain four cross-sections each, that were prepared for metallographic analysis via grinding and polishing (no etching was carried out) - details of the sample preparation are reported in Table 7. Pictures of the cross-sections were taken with Nikon Eclipse LV150N.

Tensile shear tests were carried out using Instron 5985 and following ISO 6892-1:2016 tensile test standard, to assess the mechanical requirements. Tensile load was applied at a constant extension rate of 1 mm/min and the maximum load was then extracted from the load-extension curve.

4.3.1 Requirements and design of experiments

The experimental campaign was articulated in three phases: *phase (1)* – definition of weld requirements and selection of welding parameters; *phase (2)* – characterization of the photodiode-based signals to variations of weld penetration depth; and, *phase (3)* – characterization of the photodiode-based signals to variations of part-to-part gap. To avoid bias effects, weld experiments were carried out with random order.

To define welding parameters that allow to meet the requirements, metallographic analysis was performed. For each cross-section, two descriptors of the profile of the weld seam (see Figure 26) were measured: (1) effective weld width (W_E) measured as the shortest distance from the root to the face of the weld; and, (2) bottom weld width (W_B) measured as the width of the weld at the back. Geometric feature W_B was selected to avoid false positive/negative scenarios as reference to the weld penetration only would have been inadequate. Indeed, Figure 26 (a-b) shows two cases of fully penetrated weld (fusion zone fully extended throughout the 2 foils). However, weld represented in Figure 26 (b) has a blind keyhole, with no propagation of the laser beam throughout the lower thin sheet. Therefore, the laser radiation (represented with red arrows in Figure 26 (a-b)) eventually is absorbed by the keyhole walls only (or back-reflected towards the top), and without piercing through the lower surface of the steel sheet. For this reason, cases (a) and (b) schematise two scenarios with different levels of risk of damage to the adjacent components (electrodes, etc.), and this risk in case (b) is neglectable.

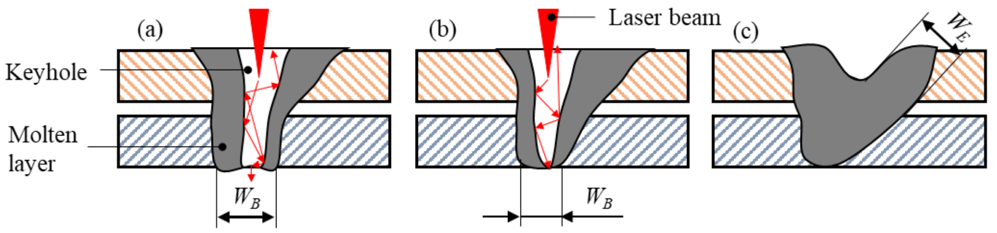

Figure 26 - Definition of the weld features. (a) Keyhole fully open throughout the bottom foil; (b) blind keyhole.

Three classes of welds were introduced to account mechanical integrity, electrical resistance and safety requirement:

Class (1) - Sound weld: $W_E \geq 220$ µm; $W_B \leq 0.6 \cdot W_E$

Class (2) - Lack of connection: $W_E \leq 220$ µm

Class (3) - Over-penetration: $W_B \geq 0.6 \cdot W_E$

Tensile shear test results conducted during phase (1) confirmed that W_E above 220 µm was sufficient to give 70 N/mm joint strength, and minimum electrical resistance below 8 µΩ

[50]. Occurrence of over-penetration is indicated by W_B. We made the assumption that the case of weld where the laser beam propagates throughout the bottom sheet (Figure 26 (a)) was the most critical for safety of the process, as it involve full opening of the keyhole. For each experiment, we checked whether a mark was left over by the laser on a surface, thus indicating the occurrence of piercing, as shown in Figure 25 (b). Results of pre-screening tests during phase (1) confirmed that in the cases when the laser beam imprinted the "check-surface" measured values of W_B were greater than 60% of W_E. For this reason, welds with $W_B \geq 0.6 \cdot W_E$ were labelled as over-penetration.

Phase (2) consisted of 54 experiments with part-to-part gap equal to zero, in which different levels of weld penetration depth were achieved by using different values of P_L in the range [600, 1500] W to reproduce weld conditions spanning from lack of connection to over-penetration. For each power level, 6 replications were performed. In phase (3), for precise control of the part-to-part gap, shim packs (Meusburger, Germany) of 12.5 mm width were used to perform a set of 16 experiments with the following values of gap: 0.0, 100, 200, 300 μm; each scenario was replicated 4 times.

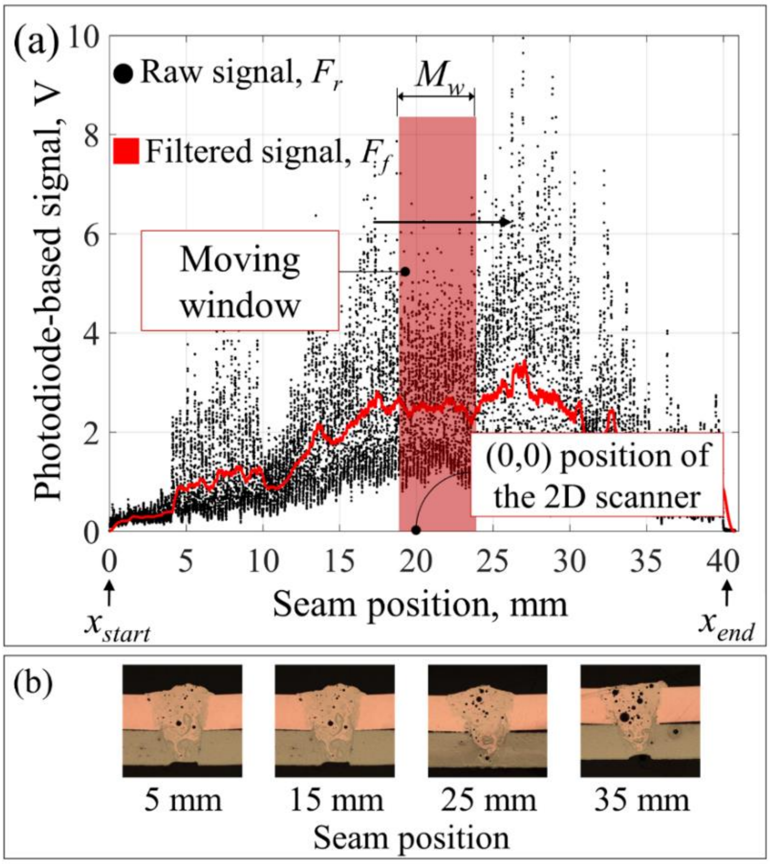

Figure 27 - Example of photodiode-based signal. (a) Raw data and low-pass filtered data, and (b) cross sections of the corresponding seam.

4.3.2 Signal processing

A typical photodiode-based signal that was recorded by the LWM sensor is reported in Figure 27. It was recorded in Volt and both software and hardware gains were adjusted to keep the signals in the range [0, 10] V.

It is worth noting that the signal follows a behaviour akin to a parabola (Figure 27 (a)). This is explained considering that the motion of the laser spot from the start to the end of the weld seam was the result of the rotation of the galvo-mirror. For this reason, the incidence angle varied with the position of the laser spot, and it seemed that this results in variation of the amount of process emission collected by the LWM sensor. This behaviour only affected the signals with negligible effect on the weld quality, as shown by the cross sections in Figure 27 (b).

A filtered signal, F_f, was derived by application of a low-pass filter to remove high-frequency disturbances (above 100 Hz).

For each signal, two descriptors were calculated:

1. *Mean value, μ,* of the filtered signal (see Figure 27 (a)) from the seam start, x_{start}, to the seam end, x_{end}.

   $$\mu = mean\left(F_f(x)\right) \tag{10}$$

2. *Scatter level, σ,* which is the result of variations that cannot be controlled and cumulate randomly, such as accidental laser material decoupling, deviations from nominal geometry of the thin sheets, and complex phaenomena involved in molten pool dynamics. The source of noise related to signal-conditioning electronics is neglected as we assumed that it is invariant to the welding process itself. The scatter level was calculated as the averaged value of the local signal scatters, which are evaluated as the standard deviations, σ_i, (see Eq. (11)) of raw data points within a moving window. Local scatters in different sections of the signals are calculated by shifting the moving window. Optimization of the width (M_w) and the number of scans (N_s) via sensitivity and convergence study with data from preliminary trials of phase (1), led to selection of the following values: M_w=5 mm and N_s=8.

$$\sigma = \frac{\sum_{i=1}^{N_S} \sigma_i}{N_S} \tag{11}$$

Calculation of signals descriptors enabled representation of the sensor signals $\mathbf{S_P}$, $\mathbf{S_T}$ and $\mathbf{S_R}$ are with the six-tuple {μ_P, μ_T, μ_R, σ_P, σ_T, σ_R}, for each welding experiment.

The correlation between signals and values of P_L and part-to-part gap was quantified by calculation of the Pearson's correlation coefficient, which varies between −100% to 100%, where 0 indicates no correlation.

Experiments were grouped in three classes, based on the label assigned to the weld with respect to the measured values of W_B and W_E, as articulated in Section 4.3.1. This allowed to perform Wilcoxon rank sum tests in paired analysis to verify the null hypotheses that the values of signal features from different classes are sampled from distributions with equal medians at significance level of 5%. The non-parametric Wilcoxon rank sum test was selected to account data non-normality and heteroscedasticity between classes.

4.4 Results and discussion

4.4.1 Variations of weld penetration depth

Different levels of weld penetration depth were obtained by varying P_L in the range [600, 1500] W to achieve weld conditions spanning from lack of connection to over-penetration.

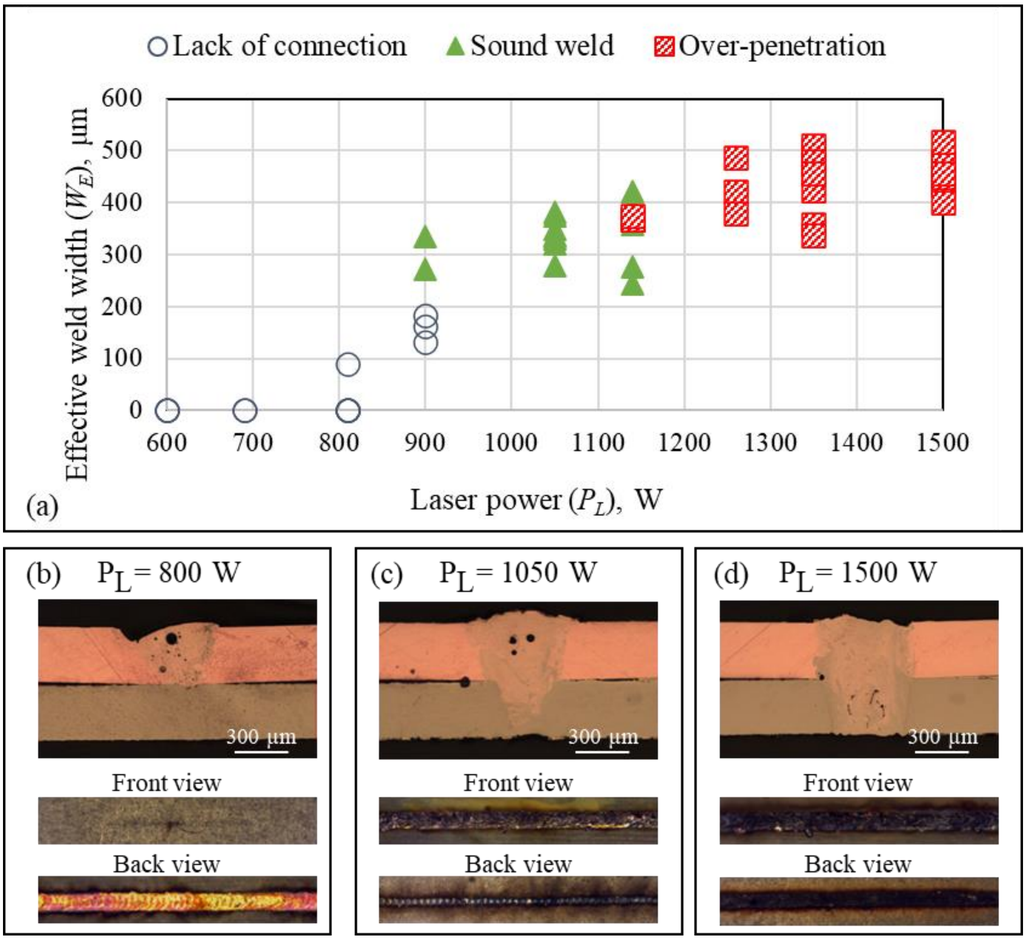

Figure 28 -(a) Results of the metallographic analysis for phase (2) - all welds with gap = 0 mm. (b) Lack of connection; (c) sound weld; (d) over-penetration.

Figure 28 reports result of metallographic analysis. Values of the W_E were plotted against the variation in laser power P_L in Figure 28 (a) showing a good linear correlation (Pearson's correlation coefficient: 89%). No connection at all (*lack of connection*) was established between the two sheets for values of up to 800 W. Adequate extension of W_E with no sign of over-penetration (*sound weld*) was achieved for values of P_L ranging between 900 and 1100 W. For values of P_L greater than 1100 W, the molten pool fully extends throughout the two sheets (*over-penetration*). Piercing of the bottom thin sheet was indicated by transition from conical to cylindrical shape in the profile of the weld seam (as confirmed by the extend of the molten pool in Figure 28 (d)), with the keyhole now fully open.

Plots of the six signal features against the laser power P_L are reported in Figure 29 - the boxplots indicate the spread across the 6 replications for each power level, and their height is a measure of it. Figure 30 shows three representatives signals of the 3 classes - only the $\mathbf{S_P}$ signals have been reported for the sake of the discussion. A trend is clearly visible, with the increase of the laser power, which determines deeper penetration of the weld, the signals show mean value and higher signal scatter. The findings are discussed as follows:

Plasma and temperature signals ($\mathbf{S_P}$ and $\mathbf{S_T}$) - positive strong correlation between the mean values of $\mathbf{S_P}$ and $\mathbf{S_T}$, and the laser power (Figure 29 (a) and (c)) – calculated values of the Pearson's correlation coefficients are equal to 95% and 87%, respectively. Also, these two signals showed strong correlation as value of the Pearson's coefficients for correlation between features of signals $\mathbf{S_P}$ and $\mathbf{S_T}$ was greater than 94%. This evidence indicated that emissions of the plasma plume contributes to both the UV/visible spectrum and the thermal radiation in the IR, which is confirmed by research by Eriksson et al. [56].

Trend of the scatter levels of $\mathbf{S_P}$ and $\mathbf{S_T}$ is very similar to the trend of their mean values, as shown in Figure 29 (b) and (d)) and confirmed by Pearson's correlation coefficients, which are equal to 89% and 85%, respectively. It is worth to observe that when lower laser power was below 800 W, metal melting was limited to the mainly copper with insufficient or even no penetration depth through the steel sheet. This suggests that the welding regime was conduction mode, which is indicated by the mean value of the plasma signal significantly low (below 1 V).

Back-reflection signal ($\mathbf{S_R}$) – correlation between the mean value of the $\mathbf{S_R}$ signal and the laser power is weak, as indicated by the Pearson's coefficient equal to 5%, and shown in Figure 29 (e). The plot of the scatter level indicated a strong positive correlation (Figure 29 (f)), instead, which was confirmed by Pearson's correlation coefficient equal to 90%. This can be explained considering that the local oscillations indicated sudden changes in the dynamics of the keyhole and of the molten pool, with consequences on the multiple reflections occurring in the keyhole.

As the laser power increased, the spread in mean value and the scatter level increased as well. For instance, box plots in Figure 29 (a), showed that the spread of the mean of the **S_P** signal (μ_P) increased from 0.05 V to 0.34 V when transitioning from 1050 W (*sound weld*) to 1500 W (*over-penetration*). This trend is in good agreement with the interpretation that the transition to the *over-penetration* condition resulted in a more instable dynamics of the keyhole with greater oscillations. Conversely, lower spread in the signal features during weld experiments with laser power below 800 W confirmed that the process was more stable because it was in conduction mode, which ultimately resulted in no or limited weld connection.

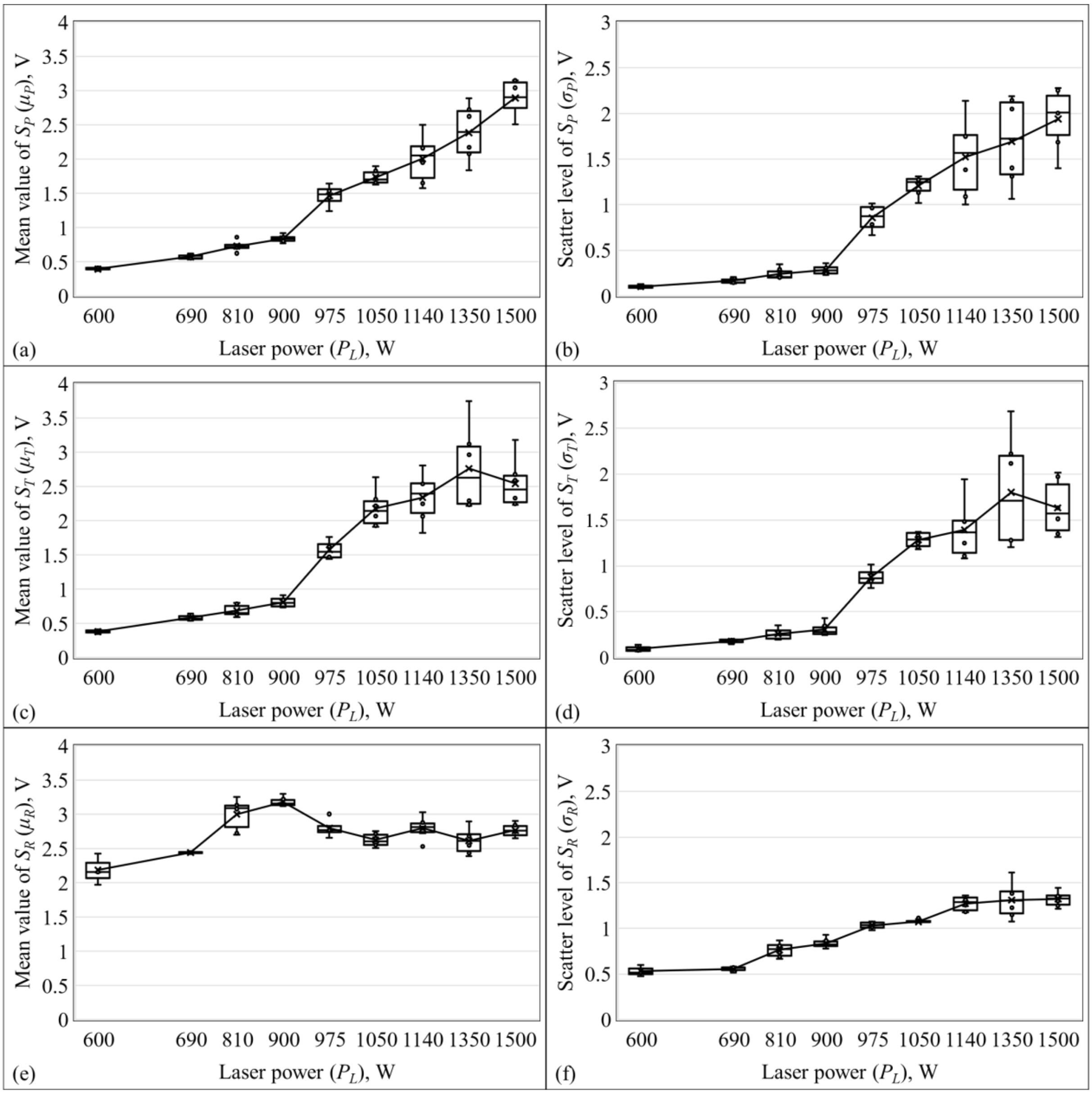

Figure 29 - Summary of the signal features extracted for phase (2) - Characterization of photodiode-based signals to variations of the laser weld (all welds at gap = 0 mm).

Paired analysis via hypothesis tests confirmed that, with the only exception of μ_R, differences between the values of the signal features corresponding to the three classes of welds were statistically different at 5% significance level. Therefore, signal features {μ_P, μ_T, σ_P, σ_T, σ_R} corresponding to different classes were statistically different, and were good indicators for in-process monitoring and diagnosis of weld features.

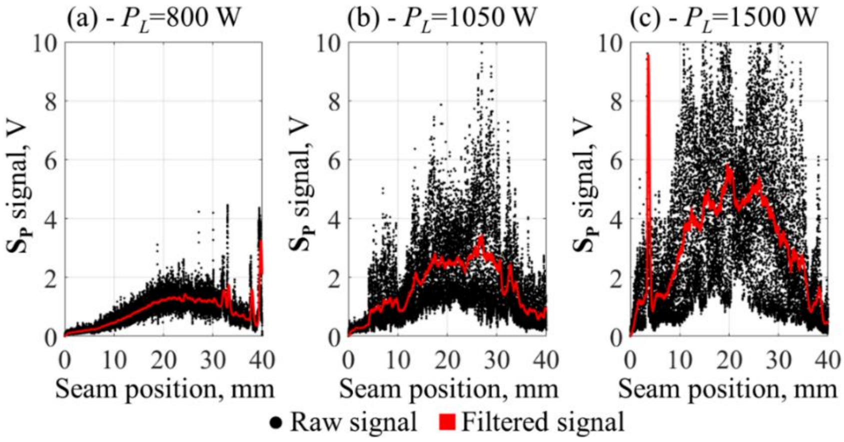

Figure 30 - Representative S_P signals of phase (2) - all welds at gap = 0 mm. (a) lack of connection; (b) sound weld; (c) over-penetration.

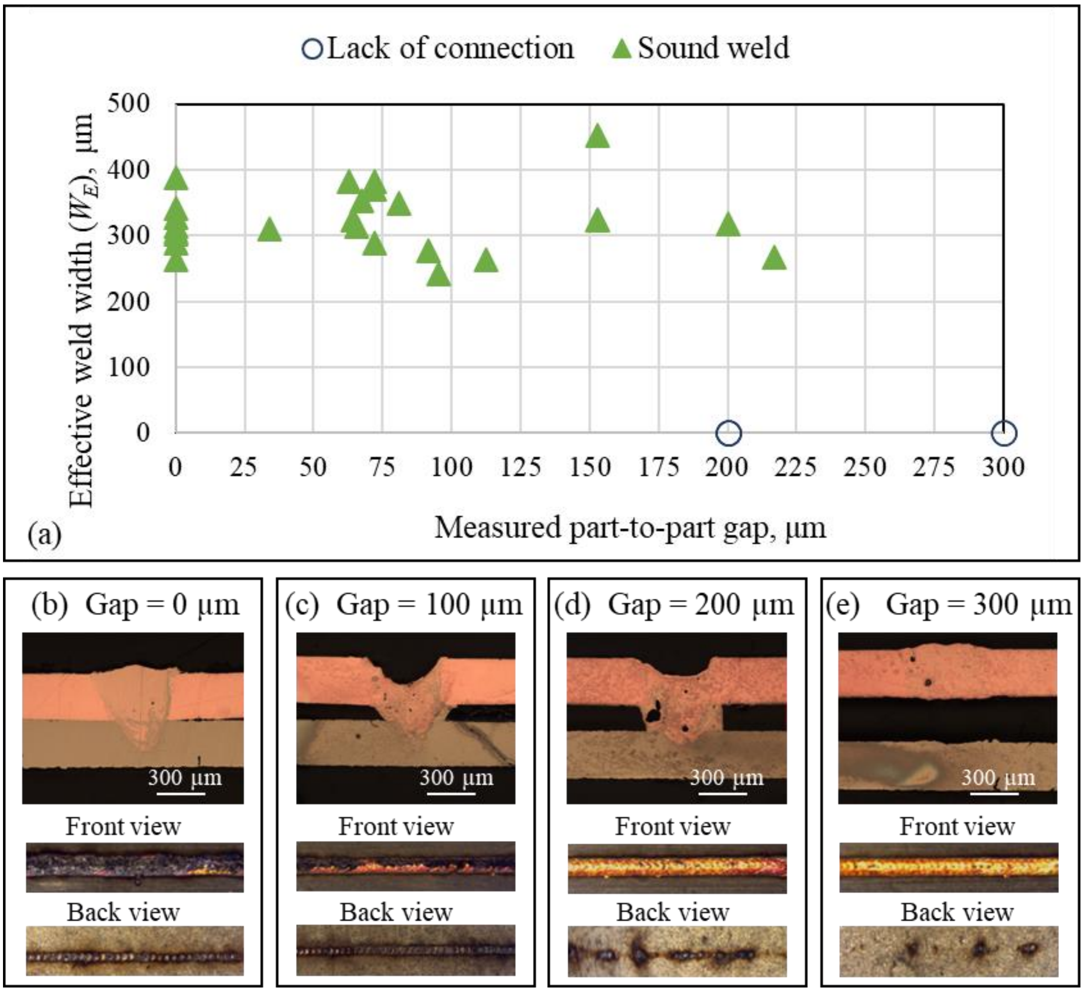

Figure 31 - (a) Results of metallographic analysis for phase (3) - al welds at P_L= 1050 W. (b, c) Sound weld; (d, e) lack of connection,

4.4.2 Variations of part-to-part gap

Characterisation of the sensor to part-to-part gap involved 4 levels of this factor: 0.0, 100, 200, 300 μm. The laser power was set constant at 1050 W. Analysis of the cross sections performed with metallographic analysis led to results reported in Figure 31. In the diagram of Figure 31 (a), measured values of the W_E are plotted against the measured values of the part-to-part gap. The trend exhibits a sudden drop in values of W_E for part-to-part gap greater than 200 μm. This indicates the transition from *sound weld* to *lack of connection*.

Representative plots of the $\mathbf{S_P}$ signals that were recorded during weld experiments with the 4 gap values considered are shown in Figure 32. They show a tendency towards lower mean values and scatter levels of the signals when the part-to-part gap increases, which is also shown by the plots in Figure 33, that report the values signal features against the part-to-part gap.

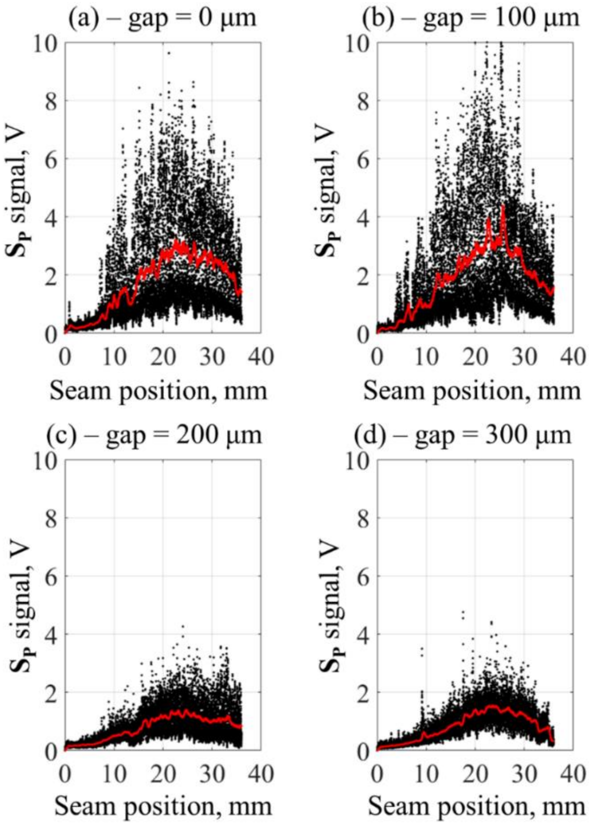

Figure 32 - Summary of the signal features extracted for phase (3) - Characterisation of photodiode-based signals to variations of part-to-part gap (all welds at P_L= 1050 W). (a, b) sound weld; (c, d) lack of connection.

Main findings are discussed as follows:

Back-reflection signal ($\mathbf{S_R}$) – Plots of both the mean value and the scatter level, that are reported in Figure 33 (e) and (f), indicate a weak sensitivity of this signal to variations of gap, which was also confirmed by values of the Pearson's coefficient below 60% for both the features.

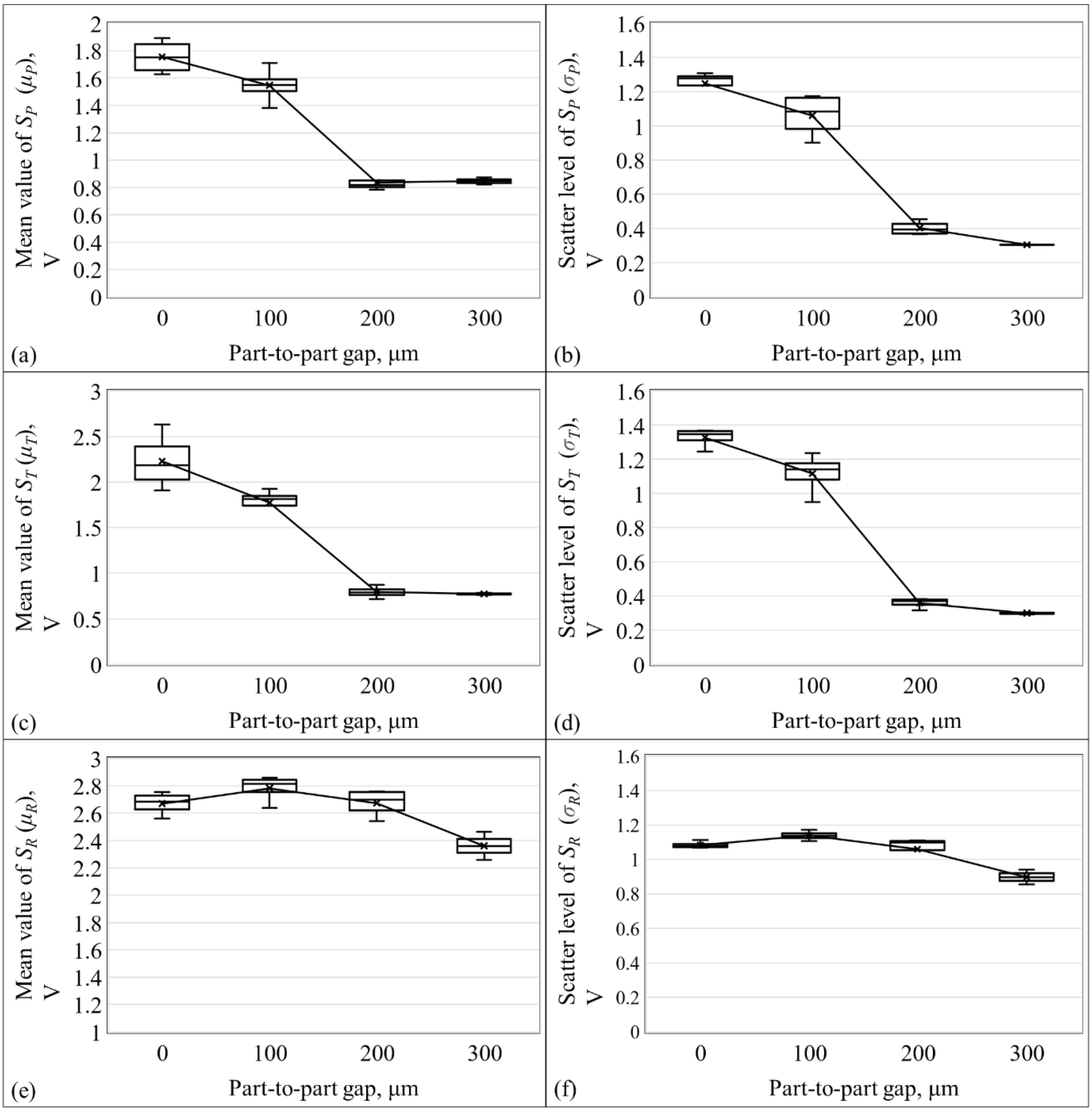

Figure 33- Summary of the signal features extracted for phase (3) - Characterisation of the photodiode-based signals to variations of part-to-part gap (all welds at P_L= 1050 W).

Plasma and temperature signals (**S_P** and **S_T**) – Plots of the mean value of **S_P** and **S_T** against the part-to-part gap (Figure 33 (a) and (c)) follow a descending trend, and calculated correlation coefficients are equal to -91% and -92%, respectively. Diagrams of the scatter level follow a similar trend (Figure 33 (b) and (d)). This descending trend was explained considering that increasing part-to-part gap caused entrapment of higher amount of plasma plume and the metal vapor between the two sheets. Therefore, the amount of radiation emitted by the plume that was collected was by the sensor was lower and this caused a drop in the signals. Strong correlation between {μ_P, μ_T, σ_P, σ_T} and gap was confirmed by Pearson's coefficients all above 98%.

Temperature signal (**S_T**) - a drop in the signal features was observed when part-to-part gap determined transition from the condition of *sound weld* to *lack of connection*, whereas from a thermal point of view, increase of the temperature on the surface of the copper sheet was expected due to different heat exchange mechanisms that were observed in section 3.4.1.3.2. This discrepancy was explained considering that the collected thermal radiation consisted of the combined contribution of both plasma plume and surface.

The step-changes in the plots of signal features {μ_P, μ_T, σ_P, σ_T} are strong indicators to diagnose the transition from *sound weld* to *lack of connection.* Their plots showed that data can be clustered in 2 groups: gap = [0,100] μm and gap = [200,300] μm, thus indicating the transition to *lack of connection* that occured between 100 and 200 μm. This finding was validated via Wilcoxon rank sum tests which confirmed that features {μ_P, μ_T, σ_P, σ_T} of signals recorded during experiments with *sound weld* and *lack of connection* had significantly different medians (at 5% significance level).

4.5 Further developments of this research

Research reported in this chapter investigated whether photodiode-based monitoring is a viable approach to detect variations of both part-to-part gap and weld penetration depth.

The approach for signal processing consisted on calculation and analysis of two features: the mean value and the signal scatter, which was evaluated as the standard deviation of signals in moving windows and depends on accumulated and un-controlled variations. Other statistical features, such as the skewness and the Kurtosis, which are the third and the fourth moments respectively, and were not investigated at this stage of the research. They could be included in future studies, as they might carry exploitable information. However, results indicated that the first two statistical features enable detection of weld defects generated by variations of both part-to-part gap and weld penetration depth.

These outcomes enabled full development of an in-process monitoring system for isolation and diagnosis of weld defects, that were addressed in the next chapter, and ultimately autonomous closed-loop control of weld quality with integrated photodiode-based sensors, powered-up by machine learning. As an example, in Figure 34, features of signal $\mathbf{S_P}$ are plotted in a “feature plane” and are clustered in distinct groups based on their classes. This 2-dimensional representation schematises a methodology that could be extended to the 6 signal features that were investigated in the present research and could be implemented to train a classification model to develop an autonomous system for automatic control of the quality during laser welding of dissimilar metallic thin sheets.

Despite capability of the photodiode-based sensor to detect individual variations of part-to-part gap and weld penetration depth was demonstrated, their simultaneous variations, which are very likely to occur and, therefore, have great practical importance in industrial environment, were not accounted. Therefore, this topic was addressed in the next chapter too. Research focused on definition of boundaries between clusters of experiments in the "feature space" with different labels to enable classification, especially in those regions were different classes overlap triggering false-negative (Type-I error) and false-positive (Type-II error).

Furthermore, the correlation between the signal spread and the welding regime (either conduction or keyhole mode) could be validated via high-speed camera in future works. Indeed, high speed cameras can provide complementary information about surface features of the process, which is spatially integrated, whereas photodiode-based signals carry spatially integrated information on the process zone, with even different dimensionality. For this reason, fusion of photodiodes and cameras for in-process monitoring is a topic of great interest that could disclose valuable opportunities. Acoustic sensors can also be involved in sensor fusion with photodiodes as they provide different information about the process, however, their performances can be affected by acoustic nuisance coming from the production environment, which is an additional challenge that needs to be overcome.

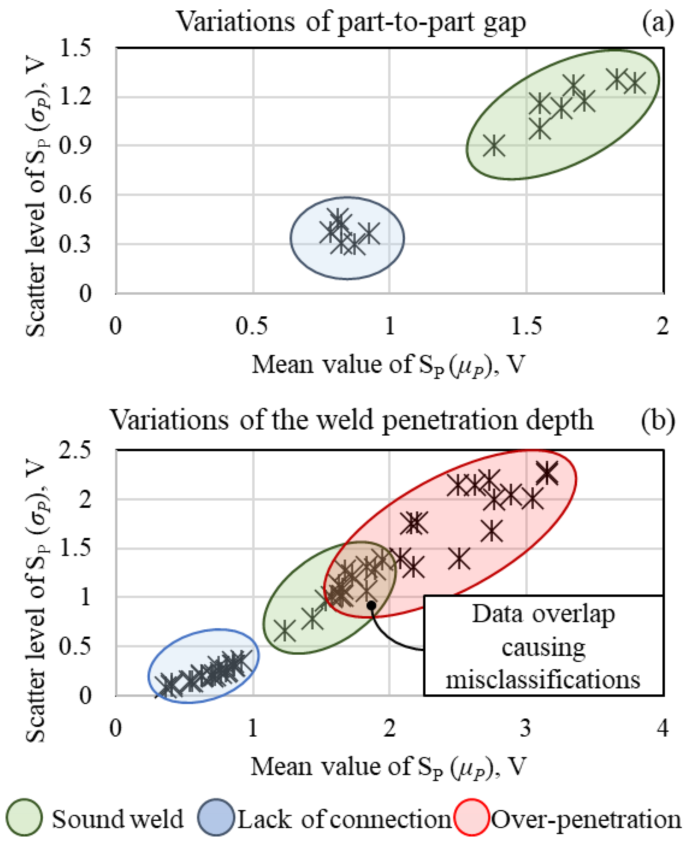

Figure 34- Representation of the "feature space" for automatic diagnosis of weld defects. (a) variations of laser power; (b) variations of the part-to-part gap.

4.6 Conclusions

In this chapter, characterisation of photodiode-based signals was performed to asses whether deviations in the weld quality due to uncontrollable variations of the part-to-part gap and weld penetration depth could be detected during RLW of copper-to-steel thin sheets lap joint. Main results are summarised as follows:

- Pearson's correlation coefficient above 94% between signal features of $\mathbf{S_P}$ and $\mathbf{S_T}$ indicates that optical emissions of the plasma plume were not limited to the UV/visible spectrum only, but also encompasses thermal radiation in the IR;
- Significant increase in the mean value and in the scatter level of signals $\mathbf{S_P}$ and $\mathbf{S_T}$ was an indicator of deeper weld penetration in the lower thin sheet.
- Signal $\mathbf{S_R}$ carried different information than signals $\mathbf{S_P}$ and $\mathbf{S_T}$, however, it offered a weaker contribution to in-process monitoring of weld defects due to part-to-part gap, as validated via Wilcoxon rank sum test and calculation of the correlation coefficient (below 60%).
- Abrupt drops in the mean value and scatter level of signals $\mathbf{S_P}$ and $\mathbf{S_T}$ were good indicators of deviations in the weld quality due to variations of the part-to-part gap. Indeed, plots of these signal features exhibited a drop when part-to-part gap increases above 100 µm which results in a transition from sound weld to lack or incomplete connection.

Chapter 5

5 Diagnosis and isolation of weld defects with supervised ML

5.1 Introduction

Previous chapter addressed the characterization of photodiodes to variations in the part-to-part gap and weld depth penetration during RLW of dissimilar metallic thin sheets. Findings demonstrated that these variations can be detected based on signal features such as the mean value and the scatter level. Definition, calculation and characterisation of signal features is the first step toward fault detection, as graphically represented by plots of experiments in *feature space* of Figure 34. Experiments resulting in similar weld quality are clustered in the same regions of the feature space. This concept is the underlying principle for automatic detection of weld defects via classification of gathered signals. However, automatic in-process quality monitoring requires a model for systematic processing of gathered data and for definition of boundaries in the "feature space" between observations belonging to different classes.

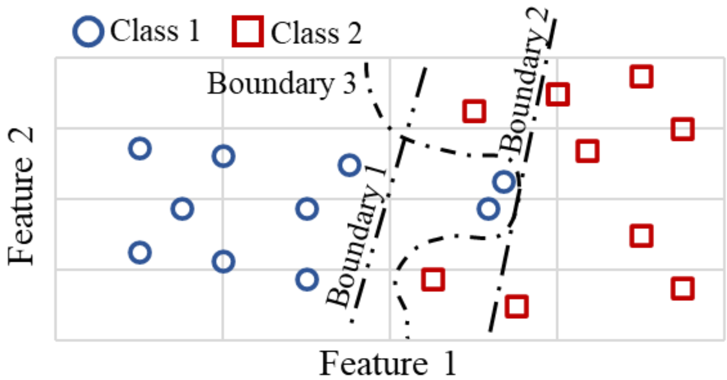

Figure 35 - Concept of feature classification - different decision boundaries as result of different partitions of the feature space.

As current advancements in digital technologies enhanced computational capabilities, ML and AI provide powerful tools that enable implementation of intelligent systems for automatic detection and diagnosis of process faults. The logic behind the automatic detection of defective welds via supervised ML algorithms is to collect a dataset by recording signals during both in-control and faulty welding process. In this way, a training dataset is generated with observations belonging to the different classes considered. Raw data are processed to calculate features that enable their representation (see Figure 35) and, ultimately, are used to train classification algorithms to define "decision boundaries" between the different classes. Then, when a new observation, that was not involved in the training process, is classified, or-in other words- the algorithm automatically assigns a label to it based on the most similar class that was learnt during the training. The way "similarity" is evaluated by different algorithms leads to different results, making the selection of the algorithm an important step in the development of a system based on classification. Scenarios in which similarity between observations with the same label is poor result in misclassifications – i.e., multiple decision boundaries can be drawn in the feature space as consequence of the fact that the same set of features describe multiple classes. The target is to achieve the lower misclassification rate possible as possible to avoid false negative (type-I error) and/or false positive (type-II error) that can affect the scrap rate and the final quality of the production.

This chapter investigates whether implementation of supervised ML algorithms and photodiodes can enable automatic diagnosis and isolation of weld defects, caused by simultaneous variation of part-to-part gap and laser power during RLW of thin sheets, with applications in battery tabs manufacturing. Photodiode-based signals were recorded in real-time during RLW of 200 µm-thick nickel-plated copper to 200 µm-thick nickel-plated steel thin sheets, and were processed to train 7 algorithms (namely, k-nearest neighbours, decision tree, random forest, Naïve-Bayes, support vector machine, discriminant analysis and discrete wavelet transform combined with neural network). Their performances were evaluated in terms of classification accuracy by introducing three classes: *lack of connection*, *sound weld* and *over-penetration weld*, and values of accuracy were compared to evaluate their capability to automatic classify weld defects. Main causes of misclassification were analysed and identified, along with arising opportunities for further development based on sensor fusion, integration with real-time multi-physical simulation and semi-supervised ML.

5.2 State of the Art

Although several innovative technological solutions have been developed in laser welding to improve stabilization of the molten pool and, therefore, widen the process window, still the weld quality does not meet the expected targets. This calls for implementation of systems for in-process monitoring of the quality. In this context, application of supervised ML algorithms is a hot research topic, as it can enable automatic detection of defective welds via classification.

Whan et al. developed a fuzzy multi-feature pattern recognition system to classify the weld quality via processing of UV and IR photodiode-based signals with respect to five classes, namely optimal heat input, slightly low heat input, low heat input, partial joining due to gap mismatch, and nozzle deviation [58]. *Sumesh et al*. trained decision tree and random forest algorithms with statistical features that were extracted by processing signals, which were collected using microphones, to estimate weld penetration depth during metal-arc welding with respect to three classes [60]. *Rodil et al.* implemented and discussed two different methods for in-process monitoring that involved time-frequency analysis of photodiode-based signals (in the IR and UV/VIS ranges) and correlation with plasma electronic temperature, respectively, to detect defective welds during laser welding of galvanized steel (1 mm thick) [26]. *Lee et al.* implemented in-situ monitoring of CO_2 laser welding of 0.83 mm-thick galvanized steel by training k-NN and SVM models with the ranked features based on the spectroscopic and temporal information of the spectra [61]. *Wang et al.* processed features extracted from pictures obtained with high speed photography and used them to train SVM algorithm to evaluate quality of welded steel plates via classification [62]. *Lei et al.* developed a novel method which leverages deep convolutional NN for detection and location of weld bead. They also proposed a deep semantic segmentation network for data augmentation to cope with the lack of open datasets in real industrial applications for effective training [35].

Ozkat et al. discussed integration of information extrapolated with photodiodes and inferred via physics-based modelling to predict geometric features of the weld seam during RLW of zinc-coated steel with a thickness ranging between 1 and 1.2 mm [53]. They also outlined opportunities for development of a CLIP control system.

As reported so far, most of the contributions in literature about implementation of classification algorithms to monitor the weld quality were applied mainly to laser welding of sheets with thickness above 1 mm, which is a process more robust to variations than assembly with thin sheets (below 500 µm) [10]. However, research about application of algorithms to predict the quality during laser welding of thin sheets needs further developments as results are still scattered and not completely exhaustive [10,27]. *Lee et al.* processed data collected with photodiodes to train and compare 3 classification algorithms, namely SVM, fully connected NN and CNN, to predict the weld penetration mode (penetration limited to the upper foils, penetration of the weld in the lower foil and transition mode) [63]. Also *Kang et al.* investigated the use of CNN to predict the weld penetration depth during RLW of 0.4mm- thick aluminium to 1mm- thick copper thin sheets processing data collected with CCD images and spectrometer to perform regression of the weld penetration depth that was ultimately validated with measurements with OCT [29].

Research reported in this chapter aimed to contribute to this field by implementing ML algorithms and photodiodes for in-process monitoring of simultaneous variations of part-to-part gap and weld penetration depth during RLW of dissimilar metallic thin sheets.

5.3 Materials and methods

5.3.1 Materials and equipment

As in Chapter 4, the laser source, the 2D scanner and the photodiode-based sensor that were used during the weld trials are an nLight Compact Fiber Laser 3kW (nLight Inc., USA), a Scout-200 (Laser & Control K-lab, South Korea), and LWM 4.0 (Laser Welding Monitoring, Precitec GmbH, Germany), respectively. Also in this research activity, we considered the 3 photodiode-based signals indicated as S_P (plasma), S_T (temperature), and S_R (back reflection), that were recorded by collecting optical emission the following three ranges: 300-700 nm, 1200-2000 nm, and 1020-1090 nm, respectively with a sampling rate of 50 kHz.

The experimental setup was the same as described in Chapter 4, with the sensor coupled to the scanner just below the collimator, and its position aligned to the centre of the process zone (see Figure 25 (a)). The weld trials were carried out implementing laser beam wobbling with a welding speed of 120 mm/s and circular oscillations with 0.2 mm radius and a frequency of 500 Hz. The laser power (P_L) was delivered in continuous mode and the direction of the laser beam was perpendicular to the specimens (this was enabled via the F-theta optics). The system was regulated so that focal point of the laser beam was positioned 500 µm above the lower surface of the bottom sheets. No filler wire and shielding gas were used. Occurrence of overpenetration with piercing of the thin sheets was indicated based on whether a print was left by the laser on a “check-surface” that was placed underneath the steel sheet, as shown in Figure 25 (b)).

5.3.2 Design of experiments and generation of datasets

The experimental campaign was designed to reproduce scenarios with simultaneous variations of the laser power and of the part-to-part gap, which, therefore, are the factors of the design of experiments. 5 levels of the laser power were considered to reproduce scenarios with variable weld penetration depth and corresponding changes in the thermal-dependent laser absorption, whereas 4 levels of part-to-part gap were considered and controlled in the experimental setup by means of shim packs. Each experimental point was reproduced with three replications that were executed with randomized order to avoid unknown bias effects. Before the welding trials, the surfaces of the specimens, that were 70 mm long and 30 mm wide, were cleaned with acetone to remove any surface contamination. Weld configuration for all the trials was lap joint with and 30 mm long. All the welds were prepared to obtain a cross section in the middle for metallographic analysis – the material preparation process consisted of mounting in resin disks, grinding and polishing steps with no etching before analysis at the optical microscope Nikon Eclipse LV150N.

During analysis at the optical microscope of the cross sections, three measures in the weld profile were taken (see Figure 36). They are: (1) the weld penetration depth, D_{pen}; (2) throat thickness, T_S; (3) and, the actual part-to-part gap. T_s was measured at the shortest distance of the weld profile from the bottom corner of the upper material. Then, experiments were labelled based on these measures with respect to three classes, whose definition derived from the need to ensure safety of the process (no laser piercing through the bottom sheet) and to meet electrical and mechanical requirements (via control of T_S and D_{pen}). These classes are:

Class (1) - *Over penetration* (OP): laser mark left on the check surface.

Class (2) - *Lack of connection* (LoC): $D_{pen} < 0.35 \cdot T_L$ and $T_S < 0.75 \cdot T_U$;

Class (3) - *Sound weld* (SW): $D_{pen} \geq 0.35 \cdot T_L$, $D_{pen} < T_L$, $T_S \geq 0.75 \cdot T_U$.

The purposes that led to definition of these labelling criteria are articulated as follows: (1) due to piercing of the thin sheets, over-penetration involves the risks of damaging adjacent components and thermal-runway; (2) minimum level (35% of T_L) of weld penetration depth to ensure mechanical resistance; (3) minimum level (75% of T_U) of throat thickness to ensure both electrical conductivity and mechanical resistance.

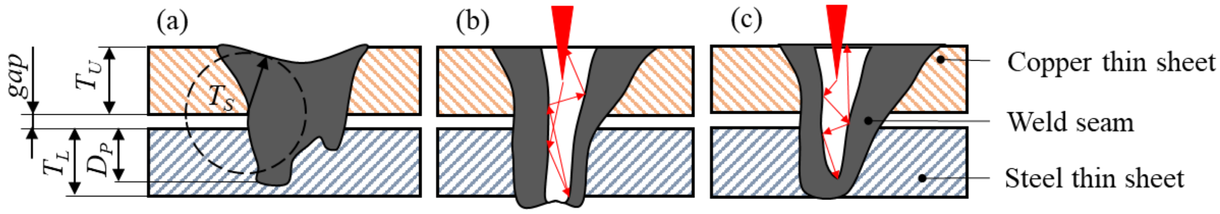

Figure 36 - Geometric features of the cross sections that were measured: the effective gap, the penetration depth (D_{pen}) and the throat thickness (T_S).

Collection of photodiode-based signals during this experimental campaign allowed generation of a dataset with simultaneous variations of laser power and part-to-part gap (dataset C). Datasets generated with experiments described in Chapter 4, that were obtained varying individually the laser power (dataset A), and only the part-to-part gap (dataset B), were included in this investigation to test the capability of the algorithms to generalise. Indeed, the copper thin sheet used in experiments of datasets A and B have different coating and thickness, as reported in Table 8.

Table 8 - Definition of datasets with related process parameters and materials.

Process & materials	Dataset		
	A	B	C
Laser power [W]	600 to 1500	1050	390 to 990
Part-to-part gap [µm]	0	0 to 300	0 to 200
No. of data points	46	14	86
Upper material, T_U	C103 copper R240 (un-coated), 300 µm		C103 copper R240, Ni-plated, 200 µm
Lower material, T_L	Hilumin (steel cold deep, Ni-plated) 300 µm		

5.3.3 Signal processing and definition of signal features

The three signals, S_P, S_T and S_R, that were recorded during weld trials with LWM 4.0 varied between 0 and 10 V, due to settings that were chosen for hardware and software gains.

As labelling of the weld trial was based on analysis of one cross section in the middle of the seam, the signals were cropped to select the corresponding portion. Therefore, a portion at the middle of each signal corresponding to 6 mm (equivalent to a duration of 0.05 seconds and approximate 2,500 readings) was extracted. To ensure correct correspondence between the selected portion of the signals and the results of metallographic analysis, length for the cropping window had to be defined carefully to account that the material preparation process was manual. This led to definition of ±3 mm tolerance, which resulted in 6 mm as total length of the cropped signal.

Then, similarly to Chapter 4, two statistical features were calculated from the selected parts of the signals: the mean value, μ, and the scatter level, σ. In this chapter, the scatter level, σ, was estimated as the standard deviation of the zero-meaned oscillations with frequencies above 100 Hz (oscillating component of the signal was calculated by subtracting a low-pass filtered signal to the raw signal). In this way, each observation of the dataset was represented with a six-tuple of signal features, $\{\mu_P, \sigma_P, \mu_T, \sigma_T, \mu_R, \sigma_R\}$.

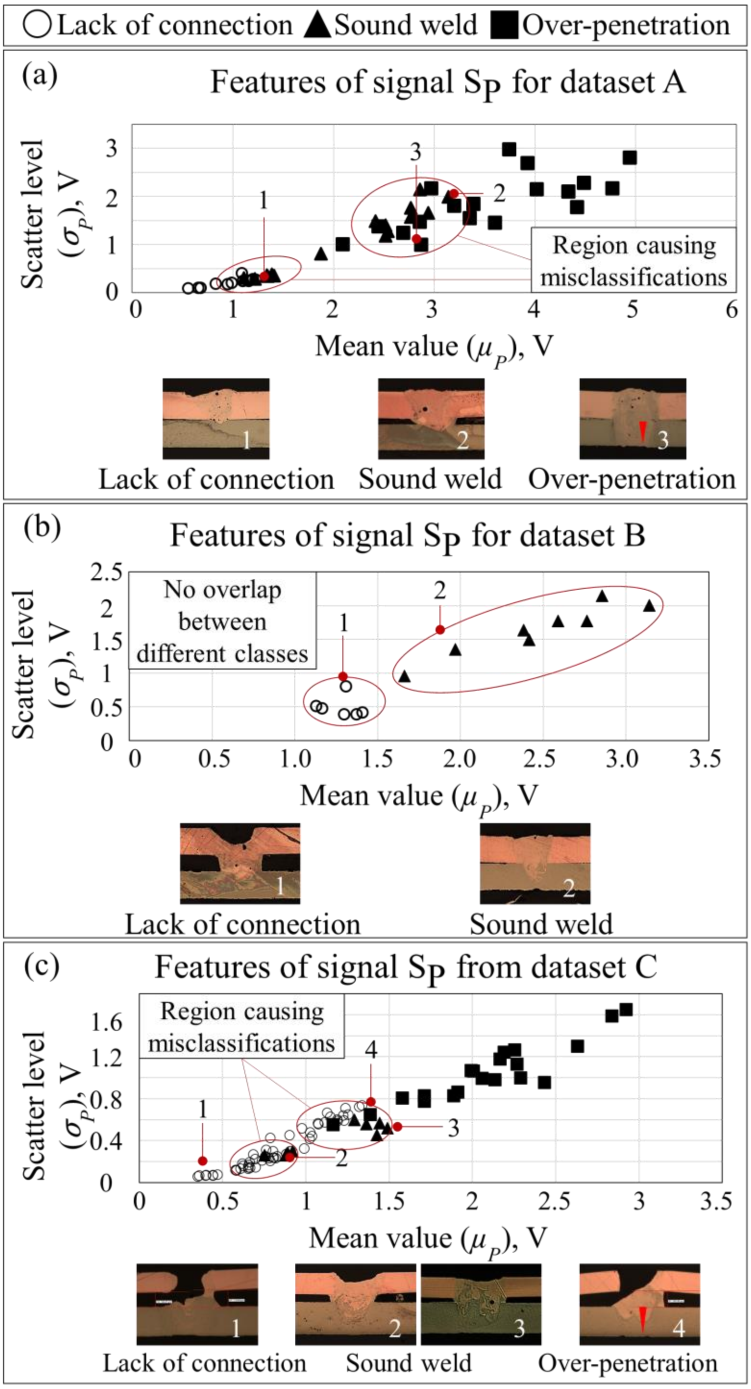

Figure 37 - Representation of the three analysed datasets for the S_P signals. Red triangle indicates laser mark left on the check surface.

Figure 37 shows three plots of the weld trials in a plane based on the values of μ_P σ_P. , one for each of the three analysed datasets. In Figure 37 (a), weld trials of dataset A are plotted, which were obtained by varying the laser power to achieve gradual variations in the weld penetration depths spanning from lack of connection to over-penetration. This gradual transition was reflected by gradual variations in the values of the signal features that resulted in overlap between different classes with a negative effect on the capability of the detection of weld defects by using classification algorithms – this point is covered more in detail in the "Results" section. Conversely, in Figure 37 (b), plot of weld trials of dataset B led to two distinct clusters as lack of connection due to excessive part-to-part gap resulted in abrupt changes of μ_P σ_P. Plot in Figure 37 (c) represented experiments of Dataset C with simultaneous variations of weld penetration depth and part-to-part gap, which also resulted in overlapped regions with gradual transition.

As the size of dataset B was limited to 14 observations and it could not be used alone to train ML algorithms, it was combined with dataset A and C (A∪B∪C) to test the capability of the algorithms to generalise even when thickness and coating of the copper thin sheets change.

5.3.4 ML models for classification of weld defects

Part of the research activity reported in this chapter consisted of benchmarking 7 ML classification models [10,38,60–62] for diagnosis and isolation of weld defects. They are:

k-NN - a data point is classified based on its position and the label of its “k” nearest neighbours, with “k” being an integer indicating the number of nearest neighbours that are considered; the most common class among the considered nearest neighbours is assigned as result of the classification.

decision tree - classification is determined by binary decisions at different nodal levels, with an observation being assigned to one of the two branches based on attribute values. Final decision results in assignation to a class at the last level, which is also called “leaf”.

random forest – they consist of an ensemble of decision trees, and are employed to cope with the tendency to overfit of individual decision trees.

Naïve-Bayes – it is a probabilistic classifier with boundaries between classes that are defined in the space of the observed attributes by leveraging Bayes theorem and assuming that the features are conditionally independent; coupling with kernel density estimation, it enables achievement of higher accuracy.

SVM - it based on definition of an hyperplane, which is a boundary, between two classes in the feature space by maximising the distance margins between observations belonging to the classes; therefore, it is suitable for binary classifications only.

discriminant analysis - boundaries between different classes are set in the space of the observed variables assuming that different classes generate data based on different Gaussian distributions.

DWT&NN - DWT is used for time-frequency analysis and returns a set of coefficients that allows representation of the signal. In this work, calculated DWT's coefficients are used as input to train a single-layer perceptron NN.

Since SVM uses a binary classifier and in this research three classes were introduced, we considered the error-correcting output codes (ECOC) model instead. It is worth noting that these methods are optimized to work with low number of features (below 100). Parameters and kernels for each of the considered ML models were summarised in Table 9.

Additionally, in this research, DWT is implemented too because it can provide features that can be useful to train classification algorithms and are different from the statistical ones which were introduced above. Indeed, DWT of signals is used for time-frequency analysis and outputs a set of coefficients that enables representation in the time-frequency bands domain [10]. Moreover, DWT is efficient in deailng with non-stationary signals, whereas other transform, such as the Fast Fourier transform can provide effective representation in the frequency domain of stationary signals only. For this reason, DWT can effectively represent also local spikes, discontinuities, and fluctuations, accounting their local frequency content.

In the context of this application, main reason to include the DWT was that it provides features that account oscillations of the photodiode-based signals which can reflect changes in the dynamics of the keyhole and molten pool. Indeed, changes in the process status can affect the recoil pressure acting on the keyhole walls and the pressure equilibrium, and therefore result in different dynamics of the keyhole and molten pool. [37].

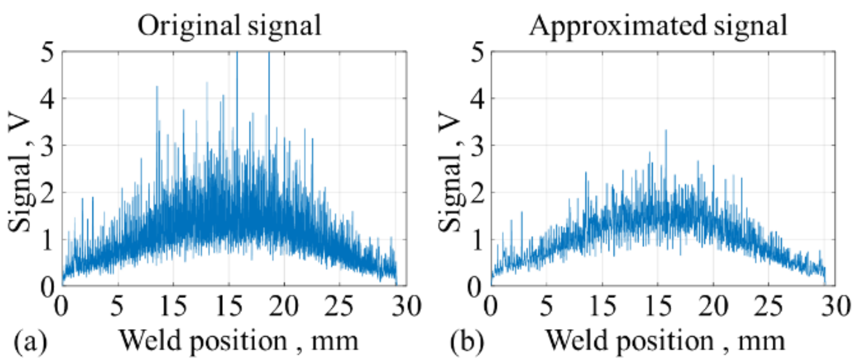

Figure 38 -Application of DWT for signal approximation. (a) Original signal with Ns=12560 and (b) approximated signal reconstructed with Ns=3140.

Table 9 - Kernels and parameters of ML models.

ML model	Parameters and kernels
(1) k-NN	Similarity metrics: Euclidean distance Number of neighbours: tested both 2 and 3. With k>3 accuracy degraded. Standardization of values of the predictors
(2) Decision tree	Algorithm: classification and decision tree (CART) with Gini diversity index split criterion. Minimum leaf size: 1 Minimum sample split: 2 Model depth: 3 for dataset A 5 for dataset C 6 for dataset A ∪ B ∪ C
(3) Random forest	Algorithm: classification and decision tree (CART) with Gini diversity index split criterion. Minimum leaf size: 1 Minimum sample split: 2 Number predictor considered at each node: 3 (randomly selected) Number of trees: 20 Model depth: 4 for dataset A 6 for dataset C 8 for dataset A ∪ B ∪ C

(4) Naïve-Bayes	Kernel smoothing density estimate with normal kernel smoother
(5) ECOC-SVM	3 binary SVM models with: - Coding design: "one-vs-one" - Kernel: linear - Solver: Iterative Single Data Algorithm - Standardization: off - Box-constraint = 1
(6) Discriminant analysis	Quadratic kernel
(7) DWT&NN	Single-layer perceptron without hidden layers

Given a signal with N_S reads, its DWT is an iterative process, and it is performed by passing it through digital low pass filters with impulse response, called *scaling function,* and through high pass filters, the *wavelet function*. The outputs of these two convolutions at a given iteration- or equivalently at a given *level*- are two sets of $N_S/2$ ordered coefficients each, which are indicated as *approximation* and *detail* and store information about the global trend of the signal and the local oscillations, respectively. The *approximation* set at a given level can be the input for the following iteration, which returns another couple of approximation and detail sets of coefficients. Iterations corresponding to different levels store information about the frequency content of the signals at different *frequency bands*. The sets of coefficients (cumulated total number of coefficients equal to N_S) returned by the transform as output of consecutive iterations can be arranged in a sparse matrix and allow non redundant representation of the signal with perfect reconstruction upon inversion.

In many applications, numeric values of the high frequency-bands coefficients are close to zero and, therefore, their contribution to the reconstruction of the original signal can be negligible [10,37]. Therefore, use of $N_s/2$, $N_s/4$ and $N_s/8$ coefficients calculated with the DWT allows representation of the original signal with progressively lower dimensionality, however the resolution is lower as information about local details is carried by lower number of coefficients. This is shown in Figure 38, where the original signal had N_s=12560 and the number of coefficients used for reconstruction was $N_s/4$=3140.

In this study, coefficients calculated with DWT were used as signal features to train NN as they allow different representation of the signal than the statistical descriptors (μ and σ). Indeed, NNs are suitable to process data with high dimensionality [15]. Many papers in literature report studies about applications of NNs that were trained to detect weld defects via classification, especially, deep neural networks (DNN) and CNN, whose potential is gaining increasing interest ([9], [14], [16]). In this study, we trained a NN which consisted of a fully connected input layer (whose nodes are the DWT coefficients) to the output layer (whose nodes are the 3 classes), with a bias vector and without hidden layers. The softmax function was then used for normalization. To avoid any randomness during the training, the weights of the fully connected layer were initialized to zero.

ML models (1) to (6) in Table 9 were trained with the 6 statistical features, $\{\mu_P, \sigma_P, \mu_T, \sigma_T, \mu_R, \sigma_R\}$, whereas the NN was trained with a subset of 1250 coefficients that were calculated by means of DWT with Haar wavelet. Accuracy of the ML models was evaluated using leave-one-out cross-validation; implementation was carried out in Matlab ©. Each algorithm was trained N times, with N being the number of observations in the dataset and also the number of folds. In this way, all the observations were individually used to test the algorithm that was trained with the remaining N-1 observations in N iterations.

Table 10 - Percentage composition (and absolute number specified) of dataset C before and after class balancing.

Class	Before	After
Lack of connection	64.4 % (55)	35.9 % (59)
Sound weld	10.5 % (9)	32.6 % (53)
Over-penetration	24.0 % (22)	31.5 % (51)

Use of a training dataset with imbalanced composition can negatively impact the accuracy of classification models. The terms *balanced* and *imbalanced* are used to describe whether classes are equally represented by the observations or not in dataset. Typically, in classification problems, different approaches are employed to cope with imbalance of the training datasets. They include under-sampling of the majority class, oversampling of the minority class, applying cost functions or synthetic data generation/augmentation [64]. In this study, dataset C was generated during experimental campaign which is described in Table 8. The design of experiments resulted in generation of an imbalanced dataset as higher number of weld trials were carried out with higher part-to-part gaps to account process instability at higher power. Therefore, balancing of dataset C was necessary and it was addressed by augmentation of the minority class via linear combination of original signals. Synthetic signals were generated by averaging original signals elementwise. Percentage class composition of dataset C before and after class balancing is reported in Table 10.

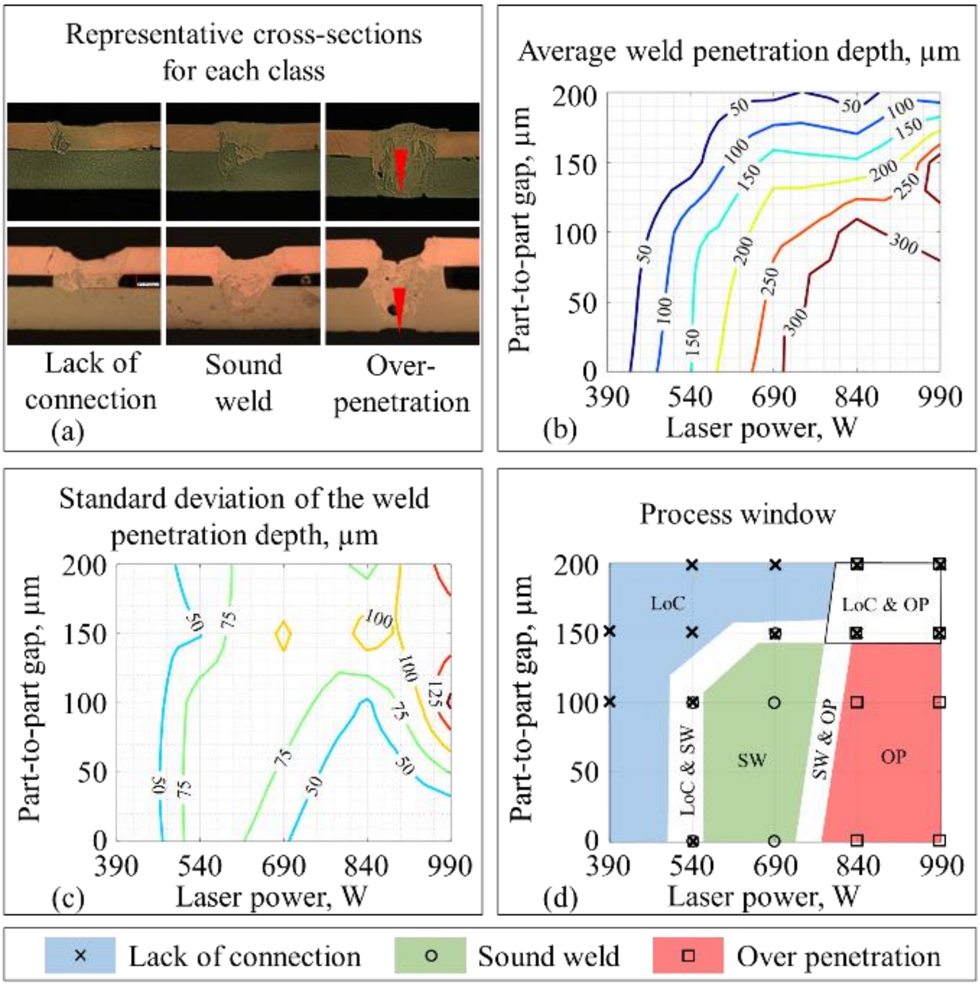

Figure 39 - Results of the metallographic analysis for dataset C, calculated over 3 replications. Red triangle indicates bottom foil piercing (a). Radial Basis Function used for regressions (R2=90%) in (b) and (c).

5.4 Results and discussion

5.4.1 Metallographic analysis

Metallographic analysis of welds and characterization of signals of datasets A and B was already addressed in the previous chapter. Hence, in this section only the results of dataset C were reviewed.

86 weld trials were carried out achieving weld conditions spanning from lack of connection to over-penetration, as shown with cross sections in Figure 39 (a). It is interesting to observe that, when part-to-part gap is zero, the transition from a condition of sound weld to over-penetration was indicated by the change of the geometric shape of the weld seam from conical to cylindrical, reflecting that the laser pierces the steel sheet and marks the check surface.

In Figure 39 (b-c), weld penetration depth and its variability are contour plotted against the part-to-part gap and weld penetration depth. They were evaluated as the mean and the standard deviation of the values that were measured in the cross sections, respectively. Predictably, increasing laser power resulted in greater weld penetration depth, as shown in Figure 39 (b), whereas increasing part-to-part gap caused reduction of the weld penetration depth. Indeed, Figure 39 (d) graphically showed that the conditions of lack of connection and over-penetration were achieved for ranges of the laser power P_L respectively equal to [390, 540] W and [840, 990] W.

Figure 39 (c) shows that when gap $\geq$ 150 μm the process variability significantly increased, especially for P_L=[840 , 990] W. This can be explained considering that these combined values of P_L and gap made the molten pool unstable since the liquid copper flowed in the part-to-part gap as gravity prevailed on viscous stresses and surface tension [49]. As result, significant variability in the weld penetration depth indicated low process repeatability (when gap $\geq$ 150 μm the standard deviation is approx. 125 μm, which is more than half of the copper thickness), and consequently the coexistence of the 2 classes (lack of connection and over-penetration) for the same experimental point of the DoE, as shown by cross sections reported in Figure 40 that were obtained from two replicas of the same experiment.

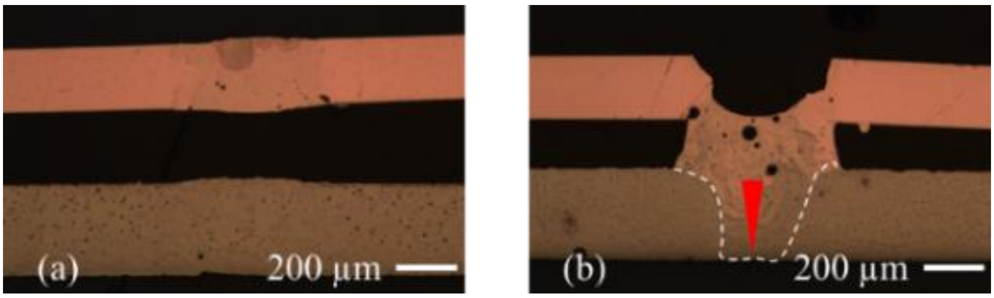

Figure 40 - Two replicas of the same experiment with gap=150 μm; PL=840 W (dataset C). (a) Lack of connection; (b) over-penetration. Red triangle indicates laser mark left on the check surface.

5.4.2 Characterization of signals

Characterization of signals S_P, S_T and S_R to simultaneous variations of laser power and part-to-part gap was addressed in this section by analysing their mean value and scatter level.

To test the statistical significance of the laser power and of part-to-part gap on the process status, a 2-way ANOVA was performed - significance level set at 5%. With the ANOVA, the null hypothesis that the process parameter had no impact on the signal feature was tested, against the alternative hypothesis that its variation had significant impact and was reflected by the variation in the signal itself. Table 11 reports the results of the 2-way ANOVAs in terms of p-values. A p-value lower than 5% implied that the alternative hypothesis is accepted. Additionally, for each of the 6 statistical features, a quadratic polynomial fitting of the data led to a regression model that was contour-plotted against the two considered factors. (Figure 41).

Table 11- Results of the ANOVA test (p-values) for each of the statistical feature (dataset C).

Feature	Variable	p-value	Significance
μ_P	P_L	1.745e-10	
	gap	1.461e-07	
σ_P	P_L	2.689e-09	
	gap	2.638e-05	Strong
μ_T	P_L	1.943e-12	
	gap	5.474e-08	
σ_T	P_L	6.625e-16	
	gap	1.213e-12	
μ_R	P_L	0.078	Weak
	gap	1	Poor
σ_R	P_L	0.078	Weak
	gap	1	Poor

Main findings are discussed as follows:

Plasma and temperature signals (**S_P** and **S_T**) – p-values smaller than 0.05 confirmed the statistical significance of laser power and part-to-part gap on the values of $\{\mu_P, \sigma_P, \mu_T, \sigma_T\}$ and indicated that variations of both these factors were reflected by signal features of S_P and S_T. Additionally, contour plots of the regressions in Figure 41 (a-d) show a positive correlation with the laser power and a negative correlation with the part-to part gap. As observed in Chapter 4, this can be explained considering that the increasing values of P_L resulted in more intense evaporation, and thermal radiation emitted by both the process zone and the plasma plume. Moreover, greater part-to-part gap caused increasing dispersion of the process radiation between the two sheets.

Back-reflection signal (**S_R**) – variations of laser power (p-value=7.8%) and part-to-part gap (p-value=100%) did not statistically describe the variations observed in the back-reflection.

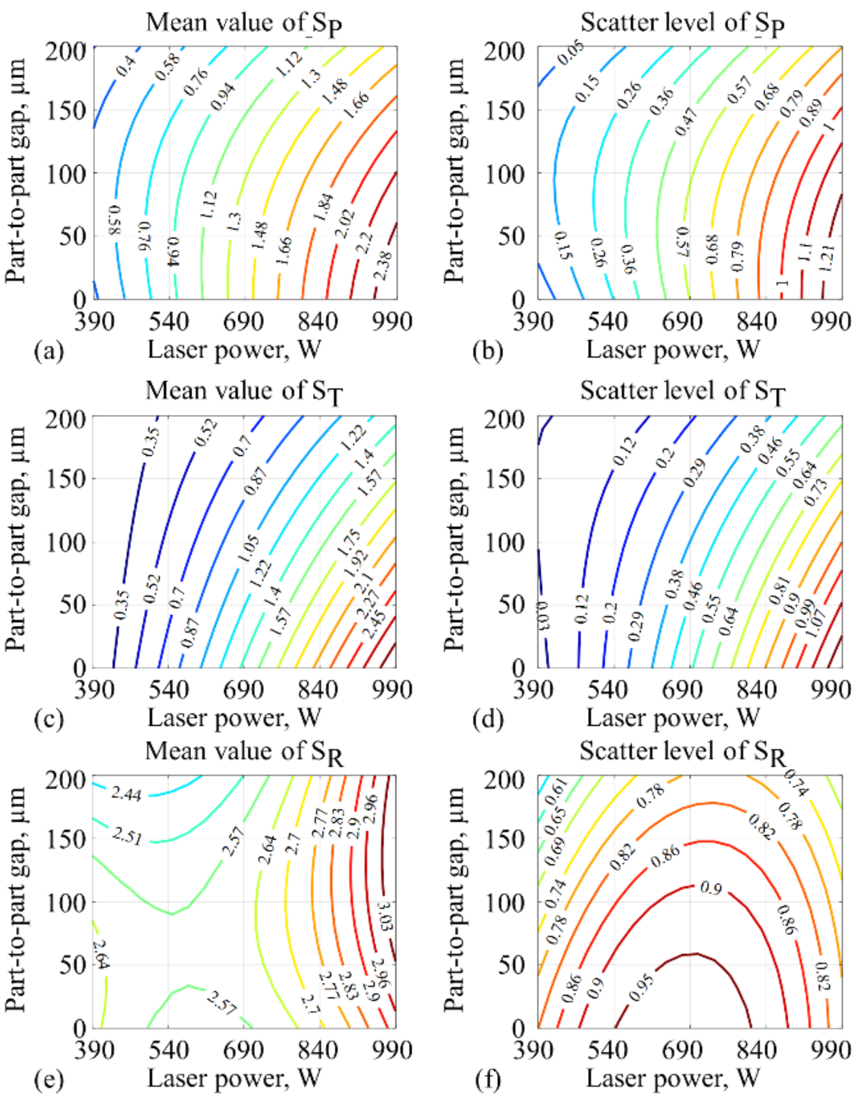

Figure 41- Contour plot of the regression models (quadratic polynomial fitting with R2 = 90%) calculated for each statistical feature (dataset C).

5.4.3 Classification of weld defects

The performances of the ML algorithms that were considered in this study were estimated as accuracy of classification in Table 12. Values of accuracy are reported in percentage and were evaluated as the ratio between the number of correct predictions and the total number of data points in the dataset; the higher the number of misclassification the lower the accuracy. To verify the capability of the models to generalise even when experimental conditions changed (thickness and coating of the copper thin sheet - see Table 8), they were also trained with dataset A ∪ B ∪ C.

Table 12- Accuracy in percentage of all the selected ML models for automatic classification of weld defects.

Algorithm	A	C	A ∪ B ∪ C
2-NN	80.4	95.1	89.5
3-NN	82.6	95.7	88.5
Decision tree	71.7	95.1	81.6
Random forest	**87**	94.5	88
Naïve-Bayes	65.2	96.9	73.8
ECOC-SVM	54.3	96.3	87.4
Discriminant analysis	71.7	96.3	84.4
DWT&NN	84.8	**97.5**	**92.7**

Discussion of main findings is articulated in the following subsections to address different aspect investigated.

5.4.3.1 Discussion about the accuracy

Smaller size and overlap of data corresponding to weld trials with different labels (see Figure 37 (a)) negatively impacted the accuracies of ML algorithms trained with dataset A. Indeed, incremental variation of signal features reflected progressive increase in the weld penetration depth, which determined overlap regions between clusters with different classes.

The random forest and the DWT&NN models scored the two highest classification accuracies respectively equal to 87% and 84.8%.

Detrimental effect of limited size of the dataset was overcome with data augmentation which was carried out to cope with imbalance of Dataset C. However, interaction between opposing effects of simultaneous variations of part-to-part gap and weld penetration depth resulted in overlap of data corresponding to different classes. Among models trained with dataset C, the highest performance was achieved by DWT&NN with 97.5% accuracy, which was explained considering that the DWT coefficients allowed a more detailed representation than the statistical features, as they carried additional information about the frequency content of the signals, thus, enabling better performances.

5.4.3.2 Discussion about the generalization

Results indicated that use of data with different experimental conditions in the training dataset induced confusion in the classification algorithms. Indeed, thickness and coating of the copper sheets changed from dataset A/B and C, resulting in degraded performances of all the algorithms when they were trained with mixed dataset ($A \cup B \cup C$) compared to when they were trained with dataset C only (which includes more observations than A and B). The algorithms were unable to generalise different experimental conditions as they were unable to find reliable patterns for classification in numeric data that reflected both changes in the process status and the experimental conditions. Once again, the algorithm that best generalised was the DWT&NN with 92.7% accuracy.

5.4.3.3 Discussion about the misclassification

Two main sources of confusion were identified with analysis of the misclassifications. They were: (1) high variability of the welding process itself due to physical properties of the metals welded (i.e., high reflective materials such as copper) or resulting from the part-to-part gaps - as articulated in 5.4.1 with Figure 39 (c); these variability was eventually not reflected in the signal features; (2) the interaction between opposing effects of the two process parameters that resulted in comparable welds but different values of the signal feature, or the existence of both over-penetration and lack of connection at the same time- this evidence is included in Figure 39 (d) with overlapped regions and it is illustrated with Figure 42.

Findings articulated so far documented that passive observation of the weld emissions with photodiodes provided useful information for the classification but did not enable complete real-time indication about the weld quality. This is because photodiodes do not directly measure weld features, but only optical radiations emitted during the process. As an example, formation of shrinkages in the upper thin sheet due to the part-to-part gap did not seems to impact the process radiation and, therefore, they were not signalled by the signal features.

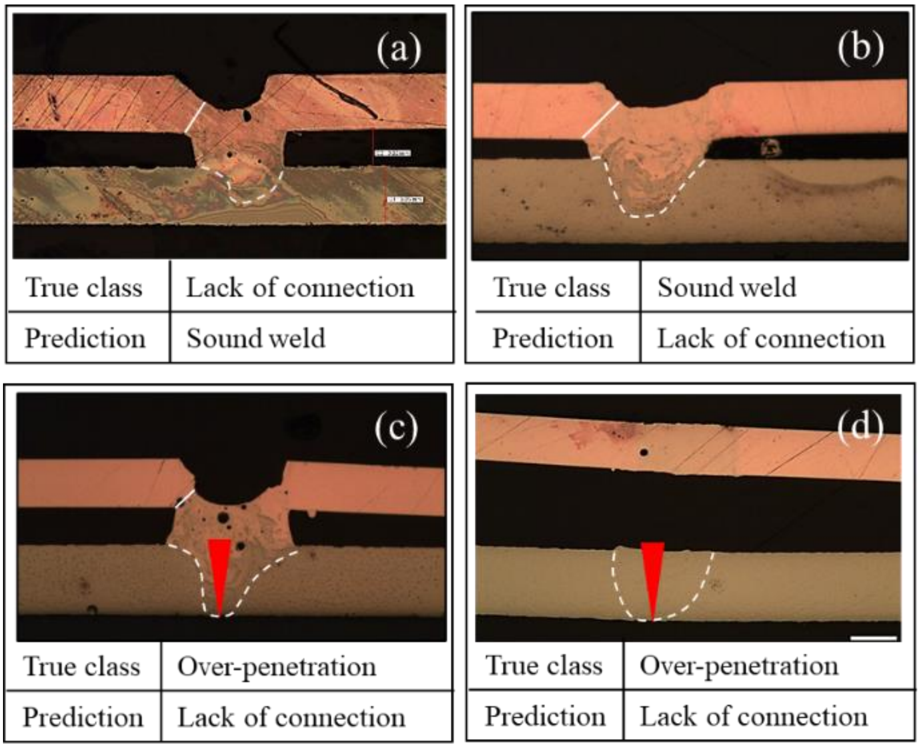

Figure 42 - Representative examples of misclassified observations for dataset C. Red triangle indicates laser mark left on the check surface.

5.5 Opportunities for further development

Discussion in the previous paragraph about generalisation, data-augmentation, and analysis of misclassifications revealed that data-drive approach is sensitive to size of dataset and to exhaustiveness of information gathered by the sensor. As the final target is to achieve the highest classification accuracy as possible, future research is needed to overcome discussed limitations. Opportunities for further developments are discussed as follows.

5.5.1 Sensor fusion

As discussed in Chapter 4, sensor fusion can enable more comprehensive indication on the weld quality and reduce causes of misclassification. Options than could be considered for integration with photodiodes are those sensors that record complementary information from observation of different features of the process, with even different dimensionality of gathered data. They include vision systems/laser scanners (for the direct measurement the seam top surface and throat thickness), microphones, or spectrometers. For this reason, research in this field can disclose opportunities to improve performance of an in-process monitoring system.

5.5.2 Integration with multi-physical simulation

Improved computational resources and the multi-physical modelling [65], are now enabling the development of digital-twin models that combine both data-driven and physics-driven approaches. As an example, sub-surface features of the process (i.e., weld pores) that cannot be directly observed due to technological challenges and limitations, could be predicted via multi-physics modelling.

5.5.3 Further developments in machine learning

As discussed along with analysis of the results, ML algorithms are *data-hungry* which means that their classification accuracies tend to improve with increasing size of the training dataset. Therefore, generation of a large dataset and labelling big number of experiments are at the same time a fundamental step for implementation of supervised ML. However, it is also a expensive and time-consuming processes. Additionally, data labelling is a manual process and prone to errors. To cope with this conflicting needs, semi-supervised ML approaches, which would rely on a mixed-dataset of both “labelled” and “un-labelled” data, could be an interesting solution to investigated, in which un-supervised algorithms, such as k-means or hierarchical clustering, could be implemented.

5.6 Conclusions

The research activity reported in this chapter focused on the combined implementation of photodiodes and ML classification algorithms to automatically diagnose and isolate weld defects due to simultaneous variations of over-penetration and lack of connection in RLW of dissimilar metallic thin sheets. To account safety, electrical and mechanical requirements of this application, three categories were defined (lack of connection, sound weld and over-penetration). Seven classification algorithms were trained and their performances in terms of accuracy were compared. Main results were articulated as follows:

- Characterization of the sensor to variations of part-to-part gap and laser power, revealed that S_P and S_T signals provided were significantly correlated to both the considered factors, whereas, correlation of back-reflection signal S_R resulted to be weak.
- Interaction between opposing effects of variations of part-to-part gap and weld penetration depth, resulted in high variability when gap ≥ 150 µm, due to the process instability caused by the limited thickness of the specimens. These variabilities were eventually not captured by the signals being a source of misclassifications.

- The NN trained with DWT coefficients of the signals enabled detection of defective weld due to simultaneous variations of weld penetration depth with classification accuracy equal to 97.5 %.
- Photodiode-based signals carried significantly correlated information to process variations for training of supervised ML models, however, recorded optical emissions did not provide exhaustive indication on the process's status, as they did not detect shrinkages in the upper sheet, for instance.

Chapter 6

6 Conclusions and future works

This chapter briefly summarises the present research, points out the main contributions, and outlines opportunities for future research.

6.1 Conclusions and key findings

This dissertation aimed to contribute toward the development of a control system for in-process control of RLW of dissimilar metallic thin sheets for manufacturing of connections within battery packs. However, development of such a system involves long term research with intermediate objectives, that include:

i. understanding of complex phenomena involved in the process,
ii. in-process monitoring of targeted nuisance factors, and
iii. classification of the actual status of the RLW process.

Therefore, this PhD focused on these research topics and addressed the following objectives:

1. Development of a multi-physics CFD model for the simulation of RWL of copper-to-steel thin sheets with variable part-to-part gap and weld penetration depth,
2. Characterization of a photodiode-based sensor to variations of part-to-part gap and weld penetration depth during RLW of dissimilar metallic battery tab connectors,
3. Implementation of photodiodes and supervised Machine Learning algorithms for automatic isolation and diagnosis of weld defects during welding of copper-to-steel thin sheets.

A multi-physics CFD model was developed, calibrated and validated with respect to the analysis at the optical microscope of weld cross-sections. This combined experimental-numeric approach enabled investigation of complex features involved in the process such phase changes, keyhole dynamics in the molten metal, and mixing mechanism. Scenarios with variable weld penetration depth and part-to-part gap enabled analysis of the effects of these disturbance factors on thermal and velocity fields. Although the variation of part-to-part gap cannot be zeroed owing to manufacturing and clamping tolerances, its detrimental effect can be reduced by the optimisation, which can be achieved via laser beam shaping, power modulation and/or beam wobbling at higher frequency. For this reason, improvement of the process via laser beam shaping was numerically investigated and discussed. Simulations with ring-shaped secondary laser beam predicted more stable dynamics of the keyhole, wider size of the melt pool, and reduced mixing between parent metals due to the more distributed input power, if compared to the case of welds with only primary beam. Results of simulations with tandem configuration were very similar, in terms of geometry of the weld seam and metal mixing, to the case of welds with primary beam only, instead.

Characterization of a photodiode-based sensor was carried out by collecting optical radiations of three distinguished bandwidths that were recorded in three signals, S_P, S_T and S_R. They were processed to extract signal features, namely the mean value and the scatter level. Statistical signal features were employed to characterize the sensor to variations of the part-to-part gap and weld penetration. Capability to detect these variations was quantitatively demonstrated via hypothesis test and estimation of the correlation with Pearson coefficients. Results showed that lack of connection in the welds due to part-to-part gap was indicated by abrupt changes in the energy intensity and in the scatter level of S_P and S_T. Variations in the weld penetration depth were indicated by gradual changes in the mean value and in the scatter level of signals S_P and S_T. Signal features of S_R carry complementary information to S_P and S_T signals, however, they showed lower correlations to the considered variations. Raw data, script of the signal processing, and results were shared on the open access Zenodo platform.

Six supervised ML algorithms, namely, k-nearest neighbours, decision tree, random forest, Naïve–Bayes, support vector machine, and discriminant analysis were trained with mean value and scatter level of photodiode-based signals S_P, S_T and S_R during weld of copper to steel thin sheets. Additionally, a NN was trained with coefficients calculated with DWT of these signals. Three classes were introduced to diagnose and isolate of defective welds, namely lack of connection, sound weld, and overpenetration. Copper sheets with different coating and thickness were used to test the capability of the models to generalise. The DWT+NN achieved best performances with accuracy of classification equal to 97% in the case of simultaneous variations of the part-to-part gap and weld penetration depth. Analysis of the misclassifications revealed that balancing of data via minority class augmentation had improved accuracy, whereas mixing of data from experiments with different copper sheets remarked that purely data-driven approach did not associate physical meaning to numeric values of signal features.

6.2 Opportunities for further developments

Opportunities for further developments were discussed along with critical analysis of results and are articulated in two sub-paragraphs that deal with research in process modelling and research in in-process monitoring.

6.2.1 Future research streams for multi-physics modelling

Development of a physical model for simulation of RLW of dissimilar metallic thin sheets is the first step toward development of a digital twin of this process. Future research could be devoted to study solutions for the integration of data gathered with sensors and results from simulations, which is a key-concept of digital twins and one the latest trend and focus of intelligent welding field.

Additionally, dedicated research with experimental-numerical approach to study the mechanical behaviour of laser welded joints with thin sheets is planned. The effects of incontrollable variations of part-to-part gap on the static and the fatigue strength is the focus of this research. It could contribute also to the research field of the digital certification of mechanical properties to meet requirements by integrating FEM models and geometry of the weld seam that was predicted with the present CFD approach.

6.2.2 Future research streams for in-process monitoring

Current performances achieved by the proposed methodology for in-process monitoring can be improved with different strategies. One of them is fusion of photodiodes with sensors that record different features of the process zone and, therefore, carry different information. For instance, coupling with imaging systems could provide more comprehensive understanding of the phaenomena as spatially resolved surface features would be complementary with specially integrated sub-surface information provided by photodiodes.

Availability of a large dataset for the training process has beneficial impact on the accuracy performances of data-driven models. However, data generation with experiments and material processing for labelling are time and resource consuming. An approach to cope with these opposed needs, is the development of a hybrid supervised/unsupervised learning with progressive storage of new data recorded during operation of the monitored process in the original training dataset by leveraging unsupervised ML algorithms such as hierarchical and k-means clustering.

References

[1] Burch, I., and Gilchrist, J., 2018, *Survey of Global Activity to Phase out Internal Combustion Engine Vehicles*.

[2] IEA, 2022, *Global EV Outlook 2022 - Securing Supplies for an Electric Future*.

[3] Shafique, M., Rafiq, M., Azam, A., and Luo, X., 2022, “Material Flow Analysis for End-of-Life Lithium-Ion Batteries from Battery Electric Vehicles in the USA and China,” Resources, Conservation and Recycling, **178**(June 2021), p. 106061.

[4] Moller, M., and Rettenmeier, M., 2021, “Laser Technologies for Battery Pack Production - a Comprehensive Overview with a Focus on the Structural Components,” *Laser in Manufacturing Conference*.

[5] Brand, M. J., Schmidt, P. A., Zaeh, M. F., and Jossen, A., 2015, “Welding Techniques for Battery Cells and Resulting Electrical Contact Resistances,” Journal of Energy Storage, **1**, pp. 7–14.

[6] Zwicker, M. F. R., Moghadam, M., Zhang, W., and Nielsen, C. V, 2020, “Journal of Advanced Joining Processes Automotive Battery Pack Manufacturing – a Review of Battery to Tab,” Journal of Advanced Joining Processes, **1**(March), p. 100017.

[7] Windisch-Kern, S., Gerold, E., Nigl, T., Jandric, A., Altendorfer, M., Rutrecht, B., Scherhaufer, S., Raupenstrauch, H., Pomberger, R., Antrekowitsch, H., and Part, F., 2022, “Recycling Chains for Lithium-Ion Batteries: A Critical Examination of Current Challenges, Opportunities and Process Dependencies,” Waste Management, **138**, pp. 125–139.

[8] Sun, T., Franciosa, P., Sokolov, M., and Ceglarek, D., 2020, “Challenges and Opportunities in Laser Welding of 6xxx High Strength Aluminium Extrusions in Automotive Battery Tray Construction,” *Procedia CIRP*, Elsevier B.V., pp. 565–570.

[9] Franciosa, P.; Sokolov, M.; Sun, T.; Chianese, G.; Ceglarek, D. ., 2021, “Laser Welding: High Volume Manufacturing for e-Mobility,” The Laser user, **M**(99), pp. 24–26.

[10] Wu, D., Zhang, P., Yu, Z., Gao, Y., Zhang, H., Chen, H., Chen, S., and Tian, Y. T., 2022, “Progress and Perspectives of In-Situ Optical Monitoring in Laser Beam Welding: Sensing, Characterization and Modeling,” Journal of Manufacturing Processes, **75**(November 2021), pp. 767–791.

[11] Kogel-Hollacher, M., 2020, “The Full Potential of Photonics in E-Mobility: An Overwiev,” The Laser user, (97), pp. 22–23.

[12] Knaak, C., von Eßen, J., Kröger, M., Schulze, F., Abels, P., and Gillner, A., 2021, “A Spatio-Temporal Ensemble Deep Learning Architecture for Real-Time Defect Detection during Laser Welding on Low Power Embedded Computing Boards,” Sensors, **21**(12).

[13] Franciosa, P., Serino, A., Botros, R. Al, and Ceglarek, D., 2019, “Closed-Loop Gap Bridging Control for Remote Laser Welding of Aluminum Components Based on First Principle Energy and Mass,” (May).

[14] Franciosa, P., Sokolov, M., Sinha, S., Sun, T., and Ceglarek, D., 2020, “Deep Learning Enhanced Digital Twin for Closed-Loop In-Process Quality Improvement,” CIRP Annals, **69**(1), pp. 369–372.

[15] Sokolov, M., Franciosa, P., Sun, T., Ceglarek, D., and Dimatteo, V., 2021, “Applying Optical Coherence Tomography for Weld Depth Monitoring in Remote Laser Welding of Automotive Battery Tab Connectors,” Journal of Laser Applications.

[16] Sattar, A., Greenwood, D., Dowson, M., and Unadkat, P., 2020, *Automotive Lithium Ion Battery Recycling in the UK Based on a Feasibility Study*.

[17] Das, A., Li, D., Williams, D., and Greenwood, D., 2018, “Joining Technologies for Automotive Battery Systems Manufacturing,” World Electric Vehicle Journal, **9**(2).

[18] Ramirez, P., 2020, *Sustainable Manufacturing*.

[19] Reinhart, G., Munzert, U., and Vogl, W., 2008, “A Programming System for Robot-Based Remote-Laser-Welding with Conventional Optics,” CIRP Annals - Manufacturing Technology, **57**(1), pp. 37–40.

[20] Rufrano, V., 2013, “Sviluppo e Validazione Di Una Metodologia per La Simulazione Degli Assemblaggi Di Corpi Deformabili Nella Saldatura Laser Remota.”

[21] Moglia, F., and Raspa, A., 2020, “New Trends in Laser Beam Welding,” PhotonicsViews, **17**(5), pp. 26–29.

[22] Ascari, A., and Fortunato, A., 2021, *Laser Dissimilar Welding of Highly Reflective Materials for E-Mobility Applications*, Elsevier Ltd.

[23] Chianese, G., Franciosa, P., Nolte, J., Ceglarek, D., and Patalano, S., 2021, “Photodiode-

Based in-Process Monitoring of Part-to-Part Gap and Weld Penetration Depth in Remote Laser Welding of Copper-to-Steel Battery Tab Connectors," *Proceedings of the ASME 2021 16th International Manufacturing Science and Engineering Conference, MSEC 2021 (2021) 2*, pp. 1–10.

[24] Mayr, A., Bauer, J., and Franke, J., 2022, "A Multi-View Deep Learning Approach for Quality Assessment in Laser Welding of Hairpin Windings Based on 2D Image Captures," Procedia CIRP, **115**, pp. 196–201.

[25] Ceglarek, D., Colledani, M., Váncza, J., Kim, D. Y., Marine, C., Kogel-Hollacher, M., Mistry, A., and Bolognese, L., 2015, "Rapid Deployment of Remote Laser Welding Processes in Automotive Assembly Systems," CIRP Annals - Manufacturing Technology, **64**(1), pp. 389–394.

[26] Saludes Rodil, S., Arnanz Gómez, R., Bernárdez, J. M., Rodríguez, F., Miguel, L. J., and Perán, J. R., 2010, "Laser Welding Defects Detection in Automotive Industry Based on Radiation and Spectroscopical Measurements," International Journal of Advanced Manufacturing Technology, **49**(1–4), pp. 133–145.

[27] Cai, W., Wang, J., Jiang, P., Cao, L., Mi, G., and Zhou, Q., 2020, "Application of Sensing Techniques and Artificial Intelligence-Based Methods to Laser Welding Real-Time Monitoring: A Critical Review of Recent Literature," Journal of Manufacturing Systems, **57**(May), pp. 1–18.

[28] Stavridis, J., Papacharalampopoulos, A., and Stavropoulos, P., 2018, "Quality Assessment in Laser Welding: A Critical Review," International Journal of Advanced Manufacturing Technology, **94**(5–8), pp. 1825–1847.

[29] Kang, S., Kang, M., Jang, Y. H., and Kim, C., 2022, "Deep Learning-Based Penetration Depth Prediction in Al/Cu Laser Welding Using Spectrometer Signal and CCD Image," Journal of Laser Applications, **34**(4), p. 042035.

[30] Chianese, G., Franciosa, P., Nolte, J., Ceglarek, D., and Patalano, S., 2021, "Characterization of Photodiodes for Detection of Variations in Part-To-Part Gap and Weld Penetration Depth During Remote Laser Welding of Copper-To-Steel Battery Tab Connectors," Journal of Manufacturing Science and Engineering, **144**(July), pp. 1–34.

[31] Simonds, B. J., Tran, B., and Williams, P. A., 2020, "In Situ Monitoring of Cu/Al Laser Welding Using Laser Induced Fluorescence," Procedia CIRP, **94**, pp. 605–609.

[32] Bernauer, C. J., Zapata, A., Kick, L., Weiss, T., Sigl, M. E., and Zaeh, M. F., 2022, “Pyrometry-Based Closed-Loop Control of the Melt Pool Temperature in Laser Metal Deposition with Coaxial Wire Feeding,” Procedia CIRP, **111**, pp. 296–301.

[33] Wagner, J., Hagenlocher, C., Hummel, M., Olowinsky, A., Weber, R., and Graf, T., 2021, “Synchrotron X-ray Analysis of the Influence of the Magnesium Content on the Absorptance during Full-penetration Laser Welding of Aluminum,” Metals, **11**(5), pp. 1–13.

[34] You, D., Gao, X., and Katayama, S., 2015, “Detection of Imperfection Formation in Disk Laser Welding Using Multiple On-Line Measurements,” Journal of Materials Processing Technology, **219**, pp. 209–220.

[35] Yang, L., Fan, J., Liu, Y., Li, E., Peng, J., and Liang, Z., 2021, “Automatic Detection and Location of Weld Beads with Deep Convolutional Neural Networks,” IEEE Transactions on Instrumentation and Measurement, **70**.

[36] Chianese, G., Franciosa, P., Sun, T., Ceglarek, D., and Patalano, S., 2022, “Using Photodiodes and Supervised Machine Learning for Automatic Classification of Weld Defects in Laser Welding of Thin Foils Copper-to-Steel Battery Tabs,” Journal of Laser Applications, **34**(4), p. 042040.

[37] Sibillano, T., Ancona, A., Rizzi, D., Lupo, V., Tricarico, L., and Lugarà, P. M., 2010, “Plasma Plume Oscillations Monitoring during Laser Welding of Stainless Steel by Discrete Wavelet Transform Application,” Sensors, **10**(4), pp. 3549–3561.

[38] Cai, W., Wang, J., Zhou, Q., Yang, Y., and Jiang, P., 2019, “Equipment and Machine Learning in Welding Monitoring: A Short Review,” ACM International Conference Proceeding Series, **Part F1476**, pp. 9–15.

[39] Günther, J., Pilarski, P. M., Helfrich, G., Shen, H., and Diepold, K., 2014, “First Steps Towards an Intelligent Laser Welding Architecture Using Deep Neural Networks and Reinforcement Learning,” Procedia Technology, **15**, pp. 474–483.

[40] Huang, W., Wang, H., Rinker, T., and Tan, W., 2020, “Investigation of Metal Mixing in Laser Keyhole Welding of Dissimilar Metals,” Materials and Design, **195**, p. 109056.

[41] Artinov, A., Meng, X., Bachmann, M., and Rethmeier, M., 2022, “Study on the Transition Behavior of the Bulging Effect during Deep Penetration Laser Beam Welding,” International Journal of Heat and Mass Transfer, **184**, p. 122171.

[42] Meng, X., Putra, S. N., Bachmann, M., Artinov, A., and Rethmeier, M., 2022, "Influence of the Free Surface Reconstruction on the Spatial Laser Energy Distribution in High Power Laser Beam Welding Modeling," Journal of Laser Applications, **34**(4), p. 042023.

[43] Daligault, J., Dal, M., Gorny, C., Coste, F., and Fabbro, R., 2022, "Combination of Eulerian and Ray-Tracing Approaches for Copper Laser Welding Simulation," Journal of Laser Applications, **34**(4), p. 042042.

[44] Deng, S., Wang, H. P., Lu, F., Solomon, J., and Carlson, B. E., 2019, "Investigation of Spatter Occurrence in Remote Laser Spiral Welding of Zinc-Coated Steels," International Journal of Heat and Mass Transfer, **140**, pp. 269–280.

[45] Lin, R., Wang, H. ping, Lu, F., Solomon, J., and Carlson, B. E., 2017, "Numerical Study of Keyhole Dynamics and Keyhole-Induced Porosity Formation in Remote Laser Welding of Al Alloys," International Journal of Heat and Mass Transfer, **108**, pp. 244–256.

[46] Ozkat, E. C., Franciosa, P., and Ceglarek, D., 2017, "Development of Decoupled Multi-Physics Simulation for Laser Lap Welding Considering Part-to-Part Gap," Journal of Laser Applications, **29**(2), p. 022423.

[47] Drobniak, P., Otto, A., Vázquez, R. G., Arias, R. M., and Arias, J. L., 2020, "Simulation of Keyhole Laser Welding of Stainless Steel Plates with a Gap," Procedia CIRP, **94**, pp. 731–736.

[48] Buttazzoni, M., Zenz, C., Otto, A., Gómez Vázquez, R., Liedl, G., and Arias, J. L., 2021, "A Numerical Investigation of the Laser Beam Welding of Stainless Steel Sheets with a Gap," Applied Sciences (Switzerland), **11**(6).

[49] Chianese, G., Jabar, S., Franciosa, P., Ceglarek, D., and Patalano, S., 2022, "A Multi-Physics CFD Study on the Part-to-Part Gap during Remote Laser Welding of Copper-to-Steel Battery Tab Connectors with Beam Wobbling," *12th CIRP Conference on Photonic Technologies [LANE 2022]*.

[50] Perez Zapico, E., Ascari, A., Dimatteo, V., and Fortunato, A., 2021, "Laser Dissimilar Welding of Copper and Steel Thin Sheets for Battery Production," Journal of Laser Applications.

[51] Seibold, M., Friedmann, H., Schricker, K., and Bergmann, J. P., 2020, "Process Control by Real-Time Pulse Shaping in Laser Beam Welding of Different Material

Combinations," Procedia CIRP, **94**, pp. 769–774.

[52] De Bono, P., Allen, C., D'Angelo, G., and Cisi, A., 2017, "Investigation of Optical Sensor Approaches for Real-Time Monitoring during Fibre Laser Welding," Journal of Laser Applications, **29**(2), p. 022417.

[53] Ozkat, E. C., Franciosa, P., and Ceglarek, D., 2017, "A Framework for Physics-Driven in-Process Monitoring of Penetration and Interface Width in Laser Overlap Welding," *Procedia CIRP*, pp. 44–49.

[54] Gao, X., Li, Z., Wang, L., Zhou, X., You, D., and Gao, P. P., 2019, "Detection of Weld Imperfection in High-Power Disk Laser Welding Based on Association Analysis of Multi-Sensing Features," Optics and Laser Technology, **115**(September 2018), pp. 306–315.

[55] Tomcic, L., Ederer, A., and Grabmann, S., 2023, "Interpreting Acoustic Emissions to Determine the Weld Depth during Laser Beam Welding Interpreting Acoustic Emissions to Determine the Weld Depth during Laser Beam Welding," **042052**(November 2022).

[56] Eriksson, I., Powell, J., and Kaplan, A. F. H., 2010, "Signal Overlap in the Monitoring of Laser Welding," Measurement Science and Technology, **21**(10).

[57] Sanders, P. G., Leong, K. H., Keske, J. S., and Kornecki, G., 1998, "Real-Time Monitoring of Laser Beam Welding Using Infrared Weld Emissions," Journal of Laser Applications, **10**(5), pp. 205–211.

[58] Whan, Y., Park, H., Rhee, S., and Kang, M., 2002, "Real Time Estimation of CO 2 Laser Weld Quality for Automotive Industry," **34**, pp. 135–142.

[59] You, D., Gao, X., and Katayama, S., 2015, "WPD-PCA-Based Laser Welding Process Monitoring and Defects Diagnosis by Using FNN and SVM," IEEE Transactions on Industrial Electronics, **62**(1), pp. 628–636.

[60] Sumesh, A., Rameshkumar, K., Mohandas, K., and Babu, R. S., 2015, "Use of Machine Learning Algorithms for Weld Quality Monitoring Using Acoustic Signature," Procedia Computer Science, **50**, pp. 316–322.

[61] Lee, S. H., Mazumder, J., Park, J., and Kim, S., 2020, "Ranked Feature-Based Laser Material Processing Monitoring and Defect Diagnosis Using k-NN and SVM," Journal of Manufacturing Processes, **55**(May 2019), pp. 307–316.

[62] Wang, T., Chen, J., Gao, X., and Li, W., 2017, “Quality Monitoring for Laser Welding Based on High-Speed Photography and Support Vector Machine,” Applied Sciences (Switzerland), **7**(3).

[63] Lee, K., Kang, S., Kang, M., Yi, S., Kim, C., and Korea, S., 2021, “Estimation of Al/Cu Laser Weld Penetration in Photodiode Signals Using Deep Neural Network Classification,” Journal of Laser Applications, (33).

[64] He, H., Bai, Y., Garcia, E. A., and Li, S., 2008, “ADASYN: Adaptive Synthetic Sampling Approach for Imbalanced Learning,” Proceedings of the International Joint Conference on Neural Networks, (3), pp. 1322–1328.

[65] Dal, M., and Fabbro, R., 2016, “An Overview of the State of Art in Laser Welding Simulation,” Optics and Laser Technology, **78**, pp. 2–14.

Ringraziamenti

Intraprendere un dottorato si è rivelata un'esperienza straordinaria sia da un punto di vista personale che da un punto di vista tecnico. Per questo sono grato e sento il bisogno di fare alcuni ringraziamenti.

Vorrei prima di tutto ringraziare i docenti cui mi sono riferito durante questo percorso.

Ringrazio il professore Stanislao Patalano per l'opportunità di un Ph.D. così ricco di esperienze e per la guida durante questi anni.

Ringrazio il professore Pasquale Franciosa, sotto la cui supervisione ho lavorato durante la mia lunga permanenza presso il Warwick Manufacturing Group in Regno Unito. Gli sono grato per avermi formato, per le tante opportunità offerte e per avermi trasmesso la passione per l'argomento cui mi sono dedicato in questi anni.

Ringrazio il professore Giovanni Pio Pucillo per la disponibilità di sempre e per gli insegnamenti impartiti fin dagli studi magistrali, al termine dei quali ho maturato il desiderio di intraprendere questo percorso.

Ringrazio il professore Antonio Lanzotti per avermi accolto nel suo gruppo di ricerca dandomi la possibilità di lavorare in un ambiente così stimolante ed amichevole.

Ringrazio tutti i colleghi, quelli italiani e quelli inglesi, con i quali ho lavorato ed ho condiviso bellissimi momenti, in particolare quelli con i quali ho lavorato più strettamente: Agnese, Andrea, Castrese, Vivek, Tianzhu, Sharhid e Qamar.

Ringrazio la mia famiglia, mamma, papà, Clara ed Alessio per avermi sempre incoraggiato, compreso e riempito d'amore. Ognuno di voi mi ha dato ciò di cui avevo bisogno per affrontare le difficoltà, le ansie e la lontananza.

Quest'esperienza mi ha insegnato un nuovo concetto di appartenenza, per questo ringrazio Ginnie, un'amica sincera ed una persona dal cuore buono. Porterò sempre con me i bellissimi momenti passati a casa tua, con Hayden e Faith.

Grazie, Giovanni, per essermi stato sempre vicino anche se molto distante per lungo tempo, per avermi compreso e per aver creduto in me. Ogni obiettivo che conseguo, lo conseguo con te.

Ringraziamenti

La borsa di dottorato è stata cofinanziata con risorse del
Programma Operativo Nazionale Ricerca e Innovazione 2014-2020 (CCI 2014IT16M2OP005),
Fondo Sociale Europeo, Azione I.1 "Dottorati Innovativi con caratterizzazione Industriale"

UNIONE EUROPEA
Fondo Sociale Europeo

Ministero dell'Università
e della Ricerca

PON
RICERCA
E INNOVAZIONE
2014 - 2020